ADVANCES IN PIEZORESISTIVE PROBES FOR ATOMIC FORCE MICROSCOPY

A DISSERTATION

SUBMITTED TO THE DEPARTMENT OF MECHANICAL ENGINEERING

AND THE COMMITTEE ON GRADUATE STUDIES

OF STANFORD UNIVERSITY

IN PARTIAL FULFILLMENT OF THE REQUIREMENTS FOR THE DEGREE OF

DOCTOR OF PHILOSOPHY

Jonah A. Harley

March 2000

© Copyright by Jonah A. Harley 2000

All Rights Reserved

I certify that I have read this dissertation and that in my opinion it is fully adequate, in scope and quality, as dissertation for the degree of Doctor of Philosophy.

Thomas W. Kenny (Principal Advisor)

I certify that I have read this dissertation and that in my opinion it is fully adequate, in scope and quality, as dissertation for the degree of Doctor of Philosophy.

Storrs T. Hoen

I certify that I have read this dissertation and that in my opinion it is fully adequate, in scope and quality, as dissertation for the degree of Doctor of Philosophy.

Calvin F. Quate

Approved for the University Committee on Graduate Studies

Abstract

The atomic force microscope (AFM) is a tool that enables the measurement of precisely localized forces with unprecedented resolution in time, space and force. At the heart of this instrument is a cantilever probe that sets the fundamental limitations of the AFM. Piezoresistive cantilevers provide a simple and convenient alternative to optically detected cantilevers, and have made it easier for commercial applications to exploit the power of the force microscope. Unfortunately, piezoresistive cantilevers do not provide performance levels equal to those of the optically detected AFM. Several advances will be discussed in this work that largely erase that discrepancy, and in some cases take the capabilities of the piezoresistive cantilever beyond those of the standard AFM cantilever.

The primary key to improved cantilevers is to make them thinner and shorter, for increased force resolution and bandwidth. A fabrication technique using epitaxially grown piezoresistors is shown to reduce cantilever thickness a factor of four below the thinnest implanted piezoresistors. Using this approach cantilevers under 100 nm have been constructed, with force sensitivity 4 orders of magnitude greater than commercially available piezoresistors. These cantilevers are capable of single digit femto-Newton-per-root-Hertz force resolution.

These ultra-thin piezoresistive cantilevers suffered from an unexpected increase in *1/f* noise, although the net force resolution was still greatly improved. It is shown in this work that the *1/f* noise observed in piezoresistive cantilevers can be accounted for using a 30-year-old model of *1/f* noise proposed by F. N. Hooge. This model states that the *1/f* noise level of a resistor is proportional to the total number of carriers. For a given dopant concentration, smaller cantilevers therefore have fewer carriers and higher *1/f* noise.

From this relation between the number of carriers and the *1/f* noise, the processing and design of piezoresistive cantilevers was optimized. Previously unknown trade-offs

are demonstrated between piezoresistor size, doping density, dopant thickness and other parameters. In most cases, clearly defined optima exist that determine the fundamental capabilities of piezoresistive cantilevers.

Finally, in an effort to extend the force measurement capabilities of piezoresistors, particularly in the presence of steep force gradients, a novel axial resonant piezoresistive AFM probe was developed. This probe has demonstrated the ability to measure pico-Newton forces with a probe that is extremely rigid (>500 N/m) and is thereby immune for snap-down instabilities.

Acknowledgements

There are many people who contributed to this work. Foremost among them was my advisor, Dr. Tom Kenny, who provided a careful balance of guidance, friendship, support, and the resources and encouragement to pursue my own ideas. The value of an advisor more skilled with the carrot than the stick is not to be underestimated.

The other member of my reading committee, Drs. Storrs Hoen and Cal Quate helped shape the final form of the written document, particularly on some important basic areas I might have otherwise glossed over.

At home I received valuable emotional support and an insightful sounding board from my partner, Gypsy Achong. Without her help I would doubtless still be adding another decimal place to some unnecessary calculation.

The Kenny lab group was a great source of ideas and assistance. I count all of them among the surprisingly exclusive group of people that provide constructive rather than self-aggrandizing criticism. Making particular intellectual contributions to this work were Aaron Barzilai, Tim Stowe, Aaron Partridge, Kurth Reynolds, Kevin Yasumura, Ben Chui, and Eugene Chow, among others.

Finally, I wish to thank my parents, Peter and Carolyn Harley. Their support, love and pride made all my endeavors seem worthwhile and attainable.

Introduction

I began work at Stanford for Dr. Kenny at the end of 1995, with a desire to learn micromachining, but no clear project in mind. Although I had no experience with atomic force microscopes, I came up with the notion to micromachine a device that could unzip strands of DNA as a tool for sequencing them. Related work was being done by Dr. Colton at the Naval Research Laboratory (NRL) in Washington, D.C. and to my surprise it turned out that he and Dr. Kenny were good friends. It further turned out that Dr. Colton's group had already begun working on an experiment very similar to the one I had envisaged, but required custom microfabricated cantilevers. I began my work in the clean room making cantilevers for the DNA work, while paying the lab fees by making piezoresistive cantilevers for another biosensor project at the NRL.

After a couple of summers in Washington, and several cantilever iterations, we still did not have a force detection apparatus with the single pico-Newton force resolution and 10s of kilohertz bandwidth to see the signals we sought. The DNA project wound down as post-docs at the NRL finished up, but the need for improved force probes was clear, and I devoted the rest of my time at Stanford to understanding the fundamental issues and improving the probe designs. The piezoresistive cantilevers for the biosensor had been successful, and I felt piezoresistors held promise as a high bandwidth sensor that could achieve the force resolution we were seeking. The inherent simplicity and convenience of piezoresistance also made it attractive as a versatile sensor for a variety of sensing applications beyond the laboratory. As a result, the rest of my efforts were focused onto understanding and improving piezoresistive force probes.

There are three main results in this thesis:

- a processing improvement to advance conventional piezoresistive cantilevers;
- optimization of such cantilevers based on fundamental noise limitations;

- a novel resonant force probe based on a resonant piezoresistive beam.

Although the ultimate goal for both the piezoresistive cantilevers and the axial resonant probes is maximum force resolution, design guidelines are initially presented based only on a sensitivity analysis without including the noise effects. While it is my feeling that noise is often neglected in MEMS device design and testing, in these two cases appropriate design guidelines can be derived from a sensitivity analysis alone, and the noise is reserved for a more complete treatment in later chapters. This approach also reflects the order in which the actual devices were designed and fabricated, since some of the noise understanding was developed through experimental results after device construction.

Table of Contents

Abstract iv

Acknowledgements vi

Introduction vii

Table of Contents ix

List of Tables xii

List of Figures xiii

List of Figures xiii

Chapter 1. Background and Motivation 1

1.1. AFM background 1
AFM imaging modes
AFM force curve mode
Unzipping DNA

1.2. Piezoresistor background 9
Piezoresistive cantilever applications

Chapter 2. Fundamental parameters of cantilever sensors 19

2.1. Cantilever design parameters 19
Sensitivity
Bandwidth
Noise
Resolution
Spring constant
Other parameters

2.2. Force instabilities 26
Attractive force instabilities and probe stiffness
Force instabilities in molecular manipulation

Chapter 3. Design for Sensitivity and Bandwidth 33

3.1. Mechanical properties of a cantilever beam 33

3.2. Stress distribution in a cantilevered beam 35

3.3. The piezoresistive coefficient 36

3.4. Piezoresistor sensitivity 38

3.5. Non-ideal dopant distributions 41
The advantage of thin piezoresistors

3.6. Summary 45

Chapter 4. Constructing Ultrathin Piezoresisitve Cantilevers 47

4.1. Standard Fabrication Procedure 47

4.2. Epitaxially grown piezoresistors 50

4.3. Detailed epitaxy fabrication procedure 51

4.4. Results: 100 nm-thick piezoresistive cantilevers 53

4.5. Outstanding fabrication issues 57
Back-side etching
Buried oxide removal
Cantilever release

4.6. Summary 60

Chapter 5. Noise in piezoresistors 63

5.1. General noise observations 63

5.2. Johnson noise 64

5.3. 1/f noise 65
Hooge noise theory
Verification of the Hooge formula
Computing the number of effective carriers

5.4. Thermomechanical noise 71

5.5. Summary 73

Chapter 6. Optimization of piezoresistor design and processing 77

6.1. Geometrical design optimization 77
Thickness
Width
Leg length

6.2. Dopant concentration 81
Dopant depth
Concentration

6.3. Surface treatment and anneal 87

6.4. Operation 91

6.5. Predicted resolution 91

6.6. Example of cantilever design 93

6.7. Summary 93
Design
Processing
Operation

Chapter 7. A novel axial resonant probe 99

7.1. An axial resonant AFM probe 101

7.2. Sensor design 103
Beam design
The tether
Probe tip
Driving the oscillator
Secondary detection

7.3. Fabrication 109

7.4. Applying calibrated forces 110

7.5. Results 113
Piezoresistor calibration
Unwanted tip modes
Demodulating the resonant signal
Force resolution

7.6. Summary and future work 120

Epilogue 125
Thin Piezoresistive Cantilevers
Axial Probe

APPENDIX A: Table of Variables 129

List of Tables

Table 1. Modulus of elasticity (E), modulus of rigidity (G) and density ($\boldsymbol{r}$) for silicon and silicon nitride. 34

Table 2. Piezoresistive coefficients for n-type and p-type silicon and germanium. 38

Table 3. Building blocks for computing the number of squares resistance. 71

List of Figures

Figure 1-1. Schematic of atomic force microscope with optical lever detection. 2

Figure 1-2. (a) 5 nm contact mode atomic resolution AFM image of mica. (b) 252 nm tapping mode AFM image of an individual human transcription factor 2: DNA complex. 3

Figure 1-3. Schematic illustration of a force curve. 4

Figure 1-4. Unzipping DNA with an AFM cantilever. 6

Figure 1-5. 50 µm × 0.1 µm tipless silicon nitride cantilevers with 5 µm paddle. 8

Figure 1-6. Schematic of a piezoresistive cantilever. 11

Figure 2-1. Piezoresistive cantilever in a Wheatstone bridge circuit. 20

Figure 2-2. Matlab simulated signals in the presence of white noise. 22

Figure 2-3. Diagram of an attractive force potential versus distance with contours of the cantilever spring constant. 28

Figure 3-1. Finite element model showing the stress distribution in a cantilever beam. 36

Figure 3-2. Diagram of integration variables and cantilever dimensions. 39

Figure 3-3. Displacement sensitivity vs. thickness for a 10 µm wide cantilever with given k or f. 44

Figure 3-4. Angular alignment difficulties with short cantilevers. 45

Figure 4-1. Generic process for the fabrication of a piezoresistive cantilever. 48

Figure 4-2. TSUPREM-4 simulations showing the dopant profile immediately following epitaxy, and after a 3-hour anneal at 700 °C. 51

Figure 4-3. SEM of 87-91 nm-thick cantilevers. 53

Figure 4-4. Response of 0.089 µm × 44 µm × 350 µm cantilever to 1 µm and 0.1 µm displacements. 54

Figure 4-5. Piezoresistor response to thermomechanical noise in a 30 mTorr vacuum. 56

Figure 4-6. Backside release mask for DRIE release. 58

Figure 4-7.	Polyimide residue on FABS cantilevers after O_2 plasma release.	60
Figure 5-1.	Typical measured cantilever noise spectrum from thin (1000 Å) cantilevers showing Johnson and *1/f* noise.	63
Figure 5-2.	Schematic of piezoresistive cantilever with variables.	64
Figure 5-3.	Noise spectra of the 100 nm-thick cantilevers shown in Figure 4-3.	67
Figure 5-4.	Measured 1/f noise power density at 10 Hz vs. number of carriers for piezoresistive cantilevers.	68
Figure 5-5.	Finite element solution of current density in a cantilever.	70
Figure 5-6.	Displacement as a function of frequency for the thermomechanical noise of an oscillator, illustrating two methods to measure Q from such a diagram.	73
Figure 6-1.	Plot of noise vs. leg length ratio *a* for standard cantilever[1] in a bandwidth from 10 Hz to 1 kHz.	80
Figure 6-2.	Force resolution as a function of doping depth.	82
Figure 6-3.	The longitudinal piezoresistive coefficient as a function of boron concentration.	83
Figure 6-4.	Minimum detectable force vs. doping concentration for standard cantilever[1] assuming a maximum power dissipation of 2.5 mW.	85
Figure 6-5.	Optimal doping depending on cantilever size and operation bandwidth.	86
Figure 6-6.	Hooge noise parameter $\boldsymbol{a}$ as a function of anneal diffusion length $\sqrt{Dt}$.	88
Figure 6-7.	Plot of sensitivity factor $\boldsymbol{b}$ vs. anneal for cantilevers of various thickness.	90
Figure 6-8.	Displacement resolution, as limited by *1/f* noise and by Johnson noise for 10 µm wide cantilevers.	92
Figure 7-1.	Schematic illustration of resonant beam AFM probe with stationary tip.	102
Figure 7-2.	Illustration of an oscillator and tether for a planar fabrication process.	104
Figure 7-3.	Calibrating an axial resonant probe.	108
Figure 7-4.	SEM image of force probe.	110

Figure 7-5. Photo of experimental set-up. 112

Figure 7-6. Vibrometer signal showing thermomechanical motion of the paddle and the probe tip. 114

Figure 7-7. Axial resonant probe with a double tether. 115

Figure 7-8. Amplitude detection of resonance shifts. 116

Figure 7-9. Force resolution of axial probe in vacuum and in air. 119

Chapter 1. Background and Motivation

1.1. AFM background

The overriding goal of this work is to improve the capabilities of the atomic force microscope[1] (AFM) and AFM-based sensors by advancing the force detection capabilities of piezoresistive cantilever probes. A brief description of the AFM and of piezoresistors is provided by way of introduction.

AFM imaging modes

The atomic force microscope uses a micromachined cantilever probe to measure forces and displacements with nanometer precision and sub-nano-Newton force resolution. In its typical configuration, a micromachined silicon or silicon nitride cantilever with an atomically sharp tip is mounted on a piezoelectric actuator. The actuator allows positioning and scanning of the tip over 10s to 100s of microns with sub-nanometer resolution, and is used to raster scan the tip across the surface. Forces on the tip that cause deflection of the cantilever can be measured to create an image of the surface.

To measure cantilever deflections, a laser is reflected off the end of the beam into a position sensitive photodetector, as illustrated in Figure 1-1. Flexing of the cantilever results in motion of the reflected laser spot, which is measured by the photodetector. In the most common imaging mode, a feedback loop is closed around the actuator so that a predetermined deflection is constantly maintained by adjusting the cantilever height as it scans across topographical features.

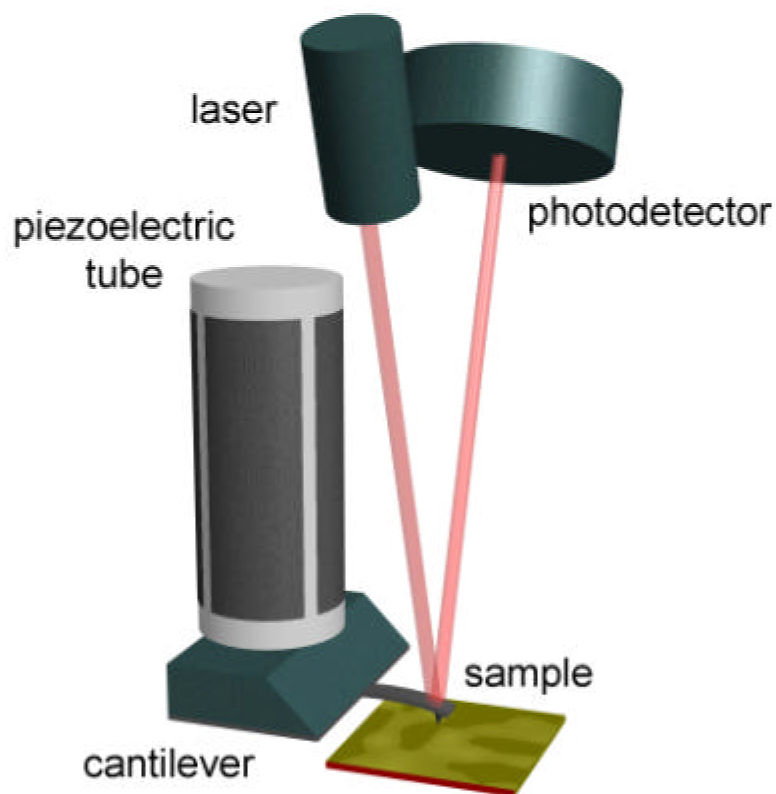

Figure 1-1. Schematic of atomic force microscope with optical lever detection.

The primary advantage of the AFM as an imaging tool is that it does not suffer from the diffraction limitations of optical or scanning electron microscopes. Such wave-based microscopes are generally limited to a resolution of the same order as the imaging wavelength. This impressive capability has been convincingly displayed by atomic resolution images of non-conducting crystals[2], an example of which is shown in Figure 1-2.

For softer samples, such as biological materials in liquid, resolution is not as high, due to deformation of the sample by the nano-Newton forces exerted by the cantilever tip. Substantial improvements have been achieved using tapping mode AFM[3], but atomic resolution is not yet possible.

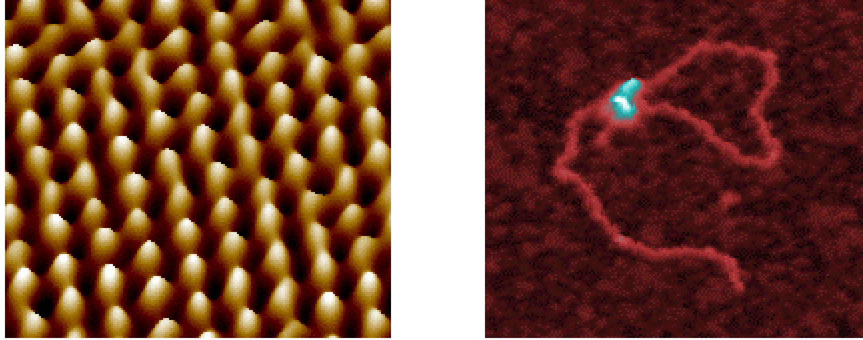

Figure 1-2. (a) 5 nm contact mode atomic resolution AFM image of mica. Image/photo taken with NanoScope® SPM, courtesy Digital Instruments, Veeco Metrology Group, Santa Barbara ,CA. (b) 252 nm tapping mode AFM image of an individual human transcription factor 2: DNA complex. Clearly resolved are the protein: protein interactions of two transcription factor proteins which facilitate the looping of the DNA. Image taken with NanoScope® SPM courtesy of Bustamante Lab, Institute of Molecular Biology, University of Oregon, Eugene.

AFM force curve mode

The AFM can also be used to measure forces as a function of cantilever distance from a single point on the surface[4]. Again, by measuring the position of a reflected laser beam, the deflection of the cantilever can be plotted as a function of distance to the surface. If the cantilever spring constant is known, this deflection can be translated into a force. A conceptualized typical force curve is shown in Figure 1-3.

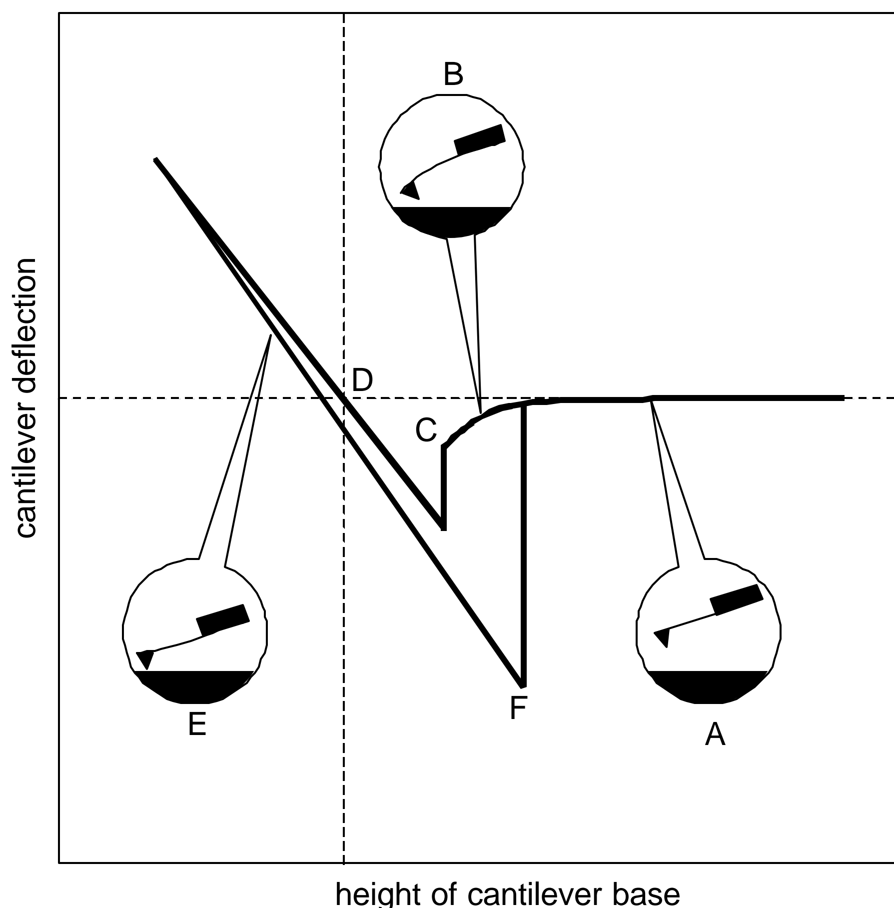

Figure 1-3. Schematic illustration of a force curve. In position (A) the cantilever is far from the surface and experiences negligible attractive force. As it approaches, the cantilever is bent towards the surface, but is not yet in contact (B). At point (C), the cantilever snaps down onto the surface. At point D, the cantilever is in contact with the surface, but has zero deflection. Further motion down and the repulsive forces bend the cantilever back (E). Upon retraction from the surface, the cantilever snaps free at point (F).

Such force curves have recently been used to measure intermolecular forces of single macromolecules such as DNA and proteins as they are unfolded or separated by a cantilever tip[5-7]. The forces to be measured in these experiments typically range in the 100s of pico-Newtons up to a few nano-Newtons. Where better force resolution is required, optical tweezers are often used, but at the expense of temporal resolution.

Optical tweezers trap a micron-sized bead in a soft potential gradient (~10^{-5} N/m) established by photon pressure from a laser[8]. The motion of the bead can be measured with a photodetector, so if the gradient strength is known, the forces that caused the motion can be inferred. Optical tweezers are limited to operation in liquid, and although the force resolution can be under a pico-Newton, the bandwidth is limited to less than one kilohertz and the maximum applied forces are in the 10s of pico-Newtons.

The force resolution of a typical AFM is ~100 pN in a 1 kHz bandwidth[9], although this can be improved to 10s of pico-Newtons in a well-controlled environment. The force to break individual hydrogen bonds has been roughly measured at about 5 pN[10], which is of the same order as the van der Waals forces between two atoms [11]. The capabilities of the AFM are tantalizingly close to allowing measurement of these fundamental force interactions with unprecedented bandwidth. The prospect of measuring the force interactions of biological macromolecules in their actual environment is particularly enticing. As a context to discuss the probe issues in such measurements, consider the following experiment, undertaken in collaboration with Dr. Colton and his group at the Naval Research Laboratory (NRL).

Unzipping DNA

The experimental objective was to measure the forces of the individual bonds that hold the two strands of double stranded DNA together, with a possible commercial application as a sequencing tool.

In one possible configuration, single stranded DNA is bound onto a substrate at the 5′ end, as illustrated in Figure 1-4. The complementary strand is then bound to a cantilever at the 3′ end. Complementary DNA binds such that the 5′ end of one strand is matched to the 3′ end of the other. When the cantilever is brought close to the surface the two strands bind together in the usual double helix. Pulling the cantilever away unzips the

DNA, sequentially breaking the complementary base-pair bonds. If the cantilever has single pico-Newton force resolution and tens to hundreds of kilohertz bandwidth in solution, it should be able to resolve the difference between the two hydrogen bonds which hold together an adenine-thymine (A-T) pair and the three hydrogen bonds which hold together a cytosine-guanine (C-G) pair. There may also be additional force variations due to interactions with neighboring bases along the length of the chain, potentially allowing full determination of the sequence. The bandwidth requirements for this experiment are approximately two orders of magnitude greater than those of most AFM measurements. Pico-Newton force resolution has not been achieved with such bandwidth.

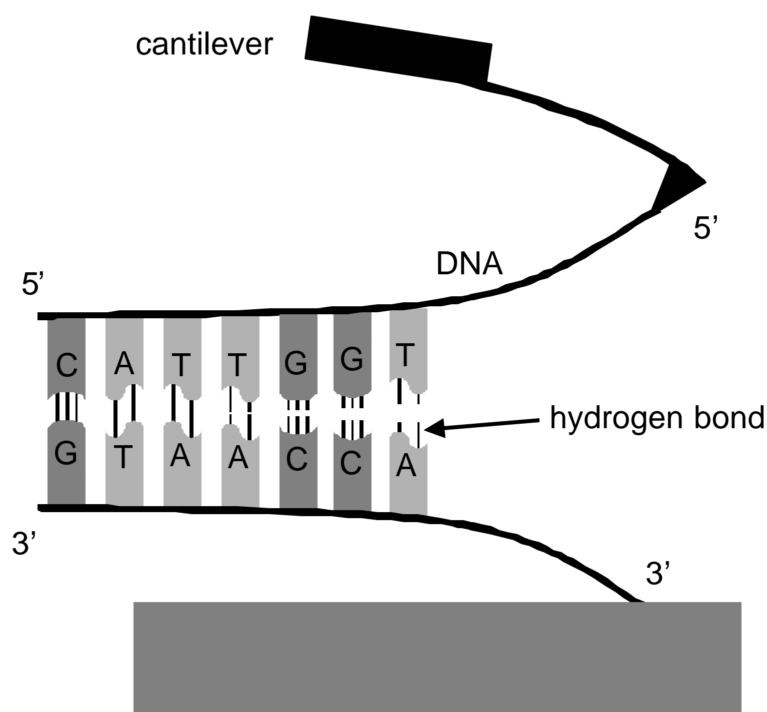

Figure 1-4. Unzipping DNA with an AFM cantilever. As the cantilever is retracted from the surface, the base-pair bonds rupture sequentially. The G-C bonds are held together with 3 hydrogen bonds, which should enable them to be distinguished from the A -T bonds which only have two hydrogen bonds.

A version of this experiment has since been completed by other researchers using a glass pipette as an extremely soft cantilever[10]. Forces were calculated by using a video camera to measure the displacement of a bead at the tip of a thin pipette. This system provided a force detector with high resolution (<1 pN) but low-bandwidth (probably under 10 Hz). Their results showed distinction between A-T-rich regions and C-G-rich regions, with separation forces in the 10-15 pN range, but could not resolve individual bond rupture events, perhaps due to the stored energy in such a soft cantilever (see section 2.2).

The first necessity for this experiment is a cantilever that meets the force resolution and bandwidth requirements. The flexibility of the cantilever determines how much bending occurs for a given force, and its resonance sets the frequency at which the measured forces become mechanically attenuated. Since the resonance is determined by the square root of the spring constant over the mass, the only way to increase both bandwidth and force sensitivity is to make thinner cantilevers (<0.1μm) for a low spring constant and shorter (<50μm), narrow (<10μm) cantilevers for low mass. An example of a custom cantilever I constructed for this application is shown in Figure 1-5. To further reduce mass, the cantilever is tipless, and an array of tips is instead fabricated on the surface to be probed. Constructing the tips on the surface rather than the cantilever gives the added advantage that if a tip becomes damaged, the measurement can be shifted to another tip without replacing the cantilever[12].

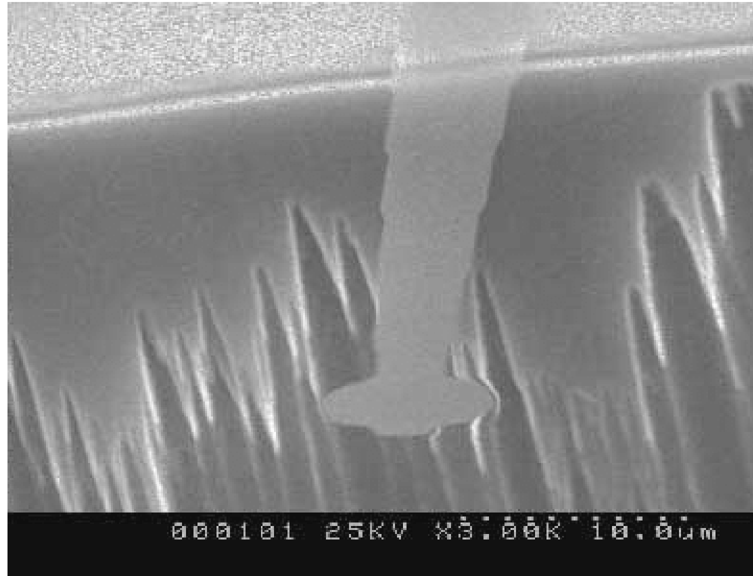

Figure 1-5. 50 µm × 0.1 µm tipless silicon nitride cantilevers with 5 µm paddle.

The main difficulty for a cantilever this size is in getting enough reflected laser light. The laser spot of a commercial AFM is about 30 µm, so not much light is reflected. Even with the addition of a 5 µm diameter paddle at the cantilever end, less than 5% of the total light is reflected from the cantilever. Furthermore, silicon nitride is fairly transparent, with transmittance of red lasers generally in excess of 60%. These two factors, but principally the former, result in a small reflected signal which is overwhelmed by the rest of the laser light reflecting back off the sample surface.

The reflectivity of the cantilever can be improved by coating the end of the paddle with a thin metal layer, as was done on a later generation of devices. The problem of the paddle size, however, can only be addressed by focusing the laser to a smaller spot size. Unfortunately, a smaller spot size means a shorter focal length, and a rapidly diverging reflected beam. This in turn means that the photo-detector must be quite close to the cantilever, so for a given cantilever deflection the laser spot in the detector does not move as far. Although the properties of the cantilevers themselves were promising, minor

modifications of the optics of a commercial AFM at the NRL were insufficient to achieve the necessary performance.

Other researchers are working to take real time images of biological processes such as DNA transcription[13], and facing similar limitations in force resolution and bandwidth. They too have constructed optical cantilevers under 10 μm wide[14], and promising efforts are underway to construct customized AFMs with optics specially designed optics[15]. There may be an easier alternative, however, that lies outside optical detection.

1.2. Piezoresistor background

Piezoresistive sensors have been around for over 40 years[16], and are widely used in commercial pressure sensors and accelerometers[17-19]. A stretched wire grows longer and thinner, which increases its resistance from geometry alone. Any conducting material can act as a strain gauge by this geometrical mechanism, but piezoresistive sensing usually refers specifically to strain gauges in semiconductors. The electrical properties of some doped semiconductors respond to stress with resistance changes over 100 times greater than those attributable to geometric changes alone.

Piezoresistors in silicon are created by introducing dopant atoms to create a conducting path. When the silicon experiences stress, and therefore strain, the lattice spacing between the atoms changes, affecting the band-gap energy. This band-gap change either increases or decreases the number of available carriers in the doped region, which is measured as a change in resistance[20].

To account for more subtle piezoresistive effects, the many-valley model of Herring is used[21]. The "valleys" of this model represent the possible combination of electron wave numbers by which an electron can enter the conduction band. Although the energy valleys themselves are anisotropic, for an unstressed silicon lattice the net effect of all the

valleys is isotropic conductivity. Under anisotropic stress, electrons move between the valleys, increasing conductivity in some directions and decreasing it in others. This model works well in n-type silicon, but is not as successful for p-type silicon[20].

The most commonly exploited piezoresistive coefficient is longitudinal, where the current flow and stress are parallel. There are also transverse and shear piezoresistive effects, however, which can have substantial effects[21]. In the transverse piezoresistive effect the current is normal to a tensile stress. The shear piezoresistive constants apply to piezoresistance arising from shear stresses. In the remainder of this work, only the longitudinal coefficient will be considered.

The first piezoresistive AFM cantilever was created at Stanford University by Marco Tortonese in 1991[22]. By implanting boron, a conducting path was created in the surface of the silicon at the base of a cantilever. Under an applied voltage bias, current flowed out one leg of the probe, and back the other as illustrated in Figure 1-6. For a downward flexing of the cantilever, tensile stress in the top layer results in an increase in resistance, and conversely when the beam is bent upwards.

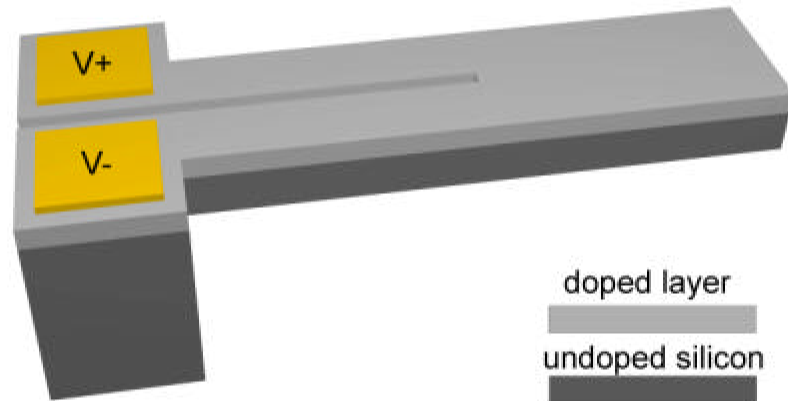

Figure 1-6. Schematic of a piezoresistive cantilever. The top layer is conducting due to a boron-doped layer. Bias on the bond pads causes current to flow out one leg and back on the other, around a physical split between the two.

Integration of a sensing element into the cantilever eliminates the need for the external laser and detector used in most AFMs. This removes the delicate step of aligning the laser to the cantilever and photodetector which usually precedes an AFM measurement, a simplification which expands the potential of the AFM for use in difficult environments such as ultrahigh vacuum chambers[23]. Integrated sensing also facilitates the use of large cantilever arrays[24], or sensors designed for portability and robustness[25]. Example applications are given in the next section.

A further advantage of piezoresistors is that the minimum size constraint associated with optical cantilevers is avoided. Reducing cantilever size allows for a simultaneous increase in bandwidth and decrease in the spring constant, key advances for increased performance.

Despite these advantages, however, most AFMs do not use piezoresistive detection, mainly because piezoresistors do not achieve the force resolution of optically detected cantilevers. With commercially available piezoresistive cantilevers, a user generally

gives up an order of magnitude of force resolution as a price for the convenience. As will be discussed later at some length, however, there are piezoresistor design and processing improvements that can make the performance of the two types of cantilevers comparable.

Piezoresistive cantilever applications

Most current piezoresistive cantilever applications are focused on developing large cantilever arrays, and cantilevers with high bandwidth. A major criticism of AFM-based imaging is that the serial nature of reading with a single tip makes it too slow for fast, large area scans. This concern has been amply answered by Minne *et al.*, who have shown impressive high-speed large-area imaging with arrays of 50 or more cantilevers[26]. Optical measurement of the displacement of many cantilevers would either require many lasers and detectors, or multiplexing of a few lasers and detectors. In either case, the precise laser and detector alignment required for each cantilever makes this approach difficult. Cantilevers with built in diffraction gratings have been developed which ease laser alignment[27], but integrated piezoresistive sensors remain more convenient.

With the ability to build an array of high-speed cantilevers comes several important commercial applications. In addition to high resolution imaging, as for semiconductor diagnostic purposes, AFM cantilevers can be used to write patterned photoresist or oxide mask lines for integrated circuit lithography[28]. The pressure for ever- smaller circuit features makes this a potential successor to current lithography technologies.

A similar pressure for smaller features also exists in the data storage industry. Magnetic bits can only be packed so closely together before they reach the paramagnetic limit and begin to flip spontaneously at room temperature. This limit is expected to occur at data density of about 100 Gbit/in^2. Small physical pits or bumps can be written and detected with AFM cantilevers to store data at densities above 500 gigabits per square

inch, and such AFM-based techniques are currently under investigation at IBM research labs in Almaden[29] and Zurich[30].

Piezoresistive cantilevers are also useful when portable, low cost individual sensors are required. Researchers at the Oak Ridge National Laboratory are developing sensors for humidity, mass, heat and chemical reactions based on cantilevers with integrated sensors[31]. Heat in a bimorph causes bending, and mass changes affect the resonant frequency. For portability and ease of use, laser interrogation is again avoided. These types of measurements can potentially be combined in an array of sensors to create an electronic nose.

All of these applications benefit from improved cantilevers. Increased cantilever resolution results in images of smaller features, faster scanning speeds, reading and writing of smaller data pits, and increased sensitivity chemical sensors. There is a ubiquitous trade-off between the smallest measurable signals and the time of measurement, so even for applications where current cantilevers suffice, improved cantilevers allow faster measurements. If enough advances can be made, piezoresistors may also hold promise for scientific AFM studies beyond the capabilities of the current optically detected devices. How these improvements can be achieved is the subject of the remainder of this work.

References

1. Binnig, G., Gerber, C., and Quate, C. F., "Atomic force microscope," *Phys. Rev. Lett.*, Vol. 56, no. 9, pp. 930-933, 1986.

2. T. R. Albrecht and C. F. Quate, "Atomic resolution imaging of a nonconductor by atomic force microscopy," *J. Appl. Phys.*, vol. 62, no. 7, pp. 2599-6022, 1987.

3. P. K. Hansma, J. P. Cleveland, M. Radmacher, D. A. Walters, P. E. Hillner, M. Bezanilla, M. Fritz, D. Vie, H. G. Hansma, C. B. Prater, J. Massie, L. Fukunaga, J. Gurley, and V. Elings, "Tapping mode atomic force microscopy in liquids," *Appl. Phys. Lett.*, vol. 64, no. 13, pp. 1738-1740, 1994.

4. N. A. Burnham, R. J. Colton, and H. M. Pollock, "Interpretation of force curves in force microscopy," *Nanotechnology* , vol. 4, pp. 64-80, 1993.

5. E. Florin, V. T. Moy, and H. E. Gaub, "Adhesion forces between individual ligand-receptor pairs," *Science*, vol. 264, pp. 415-417, 1994.

6. G. U. Lee, L. A. Chrisey, and R. J. Colton, "Direct measurement of the forces between complementary strands of DNA," *Science*, vol. 266, pp. 771-773, 1994.

7. M. Rief, M. Gautel, F. Oesterhelt, J. M. Fernandez, and H. E. Gaub, "Reversible unfolding of individual titin immunoglobulin domains by AFM," *Science*, vol. 276, no. 5315, pp. 1109-1112, 1997.

8. M. S. Z. Kellermayer, S. B. Smith, H. L. Granzier, and C. Bustamante, "Folding-unfolding transitions in single titin molecules characterized with laser tweezers," *Science*, vol. 276, pp. 1112-1116, 1997.

9. P. K. Hansma, V. B. Elings, O. Marti, and C. E. Bracker, "Scanning tunneling microscopy and atomic force microscopy: application to biology and technology," *Science*, vol. 242, no. 4876, pp. 209-216, 1998.

10. B. Essevas-Roulet, U. Bockelmann, and F. Heslot, "Mechanical separation of the complementary strands of DNA," *Proc. Natl. Acad. Sci.*, vol. 94, pp. 11935-11940, 1997.

11. Israelachvili, J., *Intermolecular and Surface Forces,* 2th ed., Academic Press Inc., London, 1992.

12. J. B. D. Green, A. Novoradovsky, P. Doewonj, and G. U. Lee, "Microfabricated tip arrays for improving force measurements," *Appl. Phys. Lett.*, vol. 74, no. 10, pp. 1498-1491, 1999.

13. N. H. Thomson, B. L. Smith, N. Almqvist, L. Schmitt, M. Kashlev, E. T. Kool, and P. K. Hansma, "Oriented, active Escherichia coli RNA polymerase: an atomic force microscope study," *Biophysical Journal*, vol. 76, no. 2, pp. 1024-1033, 1999.

14. D. A. Walters, J. P. Cleveland, N. H. Thomson, P. K. Hansma, M. A. Wendman, G. Gurley, and V. Elings, "Short cantilevers for atomic force microscopy," *Rev. Sci. Inst.*, vol. 67, no. 10, pp. 3583-3590, 1996.

15. T. E. Schaffer and P. K. Hansma, "Characterization and optimization of the detection sensitivity of an atomic force microscope for small cantilevers," *J. Appl. Phys.*, vol. 84, no. 9, pp. 4661-4666, 1998.

16. C. S. Smith, "Piezoresistance effect in germanium and silicon," *Phys. Rev.*, vol. 94, no. 1, pp. 42-49, 1954.

17. Park Scientific Instruments, *Piezolever Datasheets,* 1998

18. *Novasensor Product Catalog,* 1999

19. *Endevco product catalog,* 1999

20. Kloeck, B., "Piezoresistive sensors," *Mechanical Sensors, chapter 5,* VCH, Weinheim, Germany, 1994.

21. W. G. Pfann and R. N. Thurston, "Semiconducting Stress Transducers Utilizing the Transverse and Shear Piezoresistance Effects," *J. Appl. Phys.*, vol. 32, no. 10, pp. 2008-2019, 1961.

22. M. Tortonese, H. Yamada, R. C. Barrett, and C. F. Quate, "Atomic force microscopy using a piezoresistive cantilever," *Transducers 97. 1997 International Conference on Solid-State Sensors and Actuators*, pp. 448-451, 1991.

23. F. J. Giessibl and B. M. Trafas, "Piezoresistive cantilevers utilized for scanning tunneling and scanning force microscope in ultrahigh vacuum," *Rev. Sci. Inst.*, vol. 65, no. 6, pp. 1923-1929, 1994.

24. S. C. Minne, S. R. Manalis, A. Atalar, and C. F. Quate, "Independent parallel lithography using the atomic force microscope," *J. Vac. Sci. Technol. B*, vol. 14, no. 4, pp. 2456-2461, 1996.

25. D. R. Baselt, G. U. Lee, K. M. Hansen, L. A. Chrisey, and R. L. Colton, "A high-sensitivity micromachined biosensor," *Proc. IEEE*, vol. 85, pp. 672-680, 1997.

26. S. C. Minne, J. D. Adams, G. Yaralioglu, S. R. Manalis, A. Atalar, and C. F. Quate, "Centimeter scale atomic force microscope imaging and lithography," *Appl. Phys. Lett.*, vol. 73, no. 12, pp. 1742-1744, 1998.

27. S. R. Manalis, S. C. Minne, A. Atalar, and C. F. Quate, "Interdigital cantilevers for atomic force microscopy," *Appl. Phys. Lett.*, vol. 69, no. 25, pp. 3944-3946, 1996.

28. K. Wilder, C. F. Quate, D. Adderton, R. Bernstein, and V. Elings, "Noncontact nanolithography using the atomic force microscope," *Appl. Phys. Lett.*, vol. 73, no. 17, pp. 2527-2529, 1998.

29. H. J. Mamin, B. D. Terris, L. S. Fan, S. Hoen, R. C. Barrett, and D. Rugar, "High-density data storage using proximal probe techniques," *IBM Journal of Research and Development*, vol. 39, no. 6, pp. 681-699, 1995.

30. G. Binnig, M. Despont, U. Drechsler, W. Haberle, M. Lutwyche, P. Vettiger, H. J. Mamin, B. W. Chui, and T. W. Kenny, "Ultrahigh-density atomic force microscopy data storage with erase capability," *Appl. Phys. Lett.*, vol. 74, no. 9, pp. 1329-1331, 1999.

31. Thundat, T., Oden, P. I., and Warmack, R. J., "Chemical, physical, and biological detection using microcantilevers," *Proceedings of the Third International Symposium on Microstructures and Microfabricated Systems*, pp. 179-189, Pennington, NJ, 1997.

Chapter 2. Fundamental parameters of cantilever sensors

The goal of any sensor is to measure signals of interest in the presence of noise, and to do so on a time scale commensurate with the signal. Furthermore, the sensor cannot be too obtrusive during the measurement, and thereby affect the signals or change the environment.

A large response to a small signal is clearly beneficial to the performance of a sensor, and is measured as the sensitivity. The output without an input signal is the noise. Resolution is defined as the noise divided by the sensitivity, and is a measure of the smallest resolvable signal. It should therefore be as small a number as possible. The frequency range of the signals that can be measured is the bandwidth, and is related to the speed of the sensor, as well as the sampling rate and the total length of the measurement. Finally, for an AFM cantilever, the spring constant of the beam will determine how it interacts with its environment.

These important terms−sensitivity, noise, resolution, bandwidth and spring constant−will each be explained in more detail below.

2.1. Cantilever design parameters

Sensitivity

For transducers that convert an input signal into an electrical signal, the sensitivity determines how large the output voltage is given a particular input. For a force sensor, it is therefore usually quoted in units of volts per Newton [V/N], and for displacement sensors in volts per meter [V/m]. In a piezoresistor, a change is resistance is usually

converted into a voltage by using a Wheatstone bridge followed by an instrumentation amplifier, as shown in Figure 2-1.

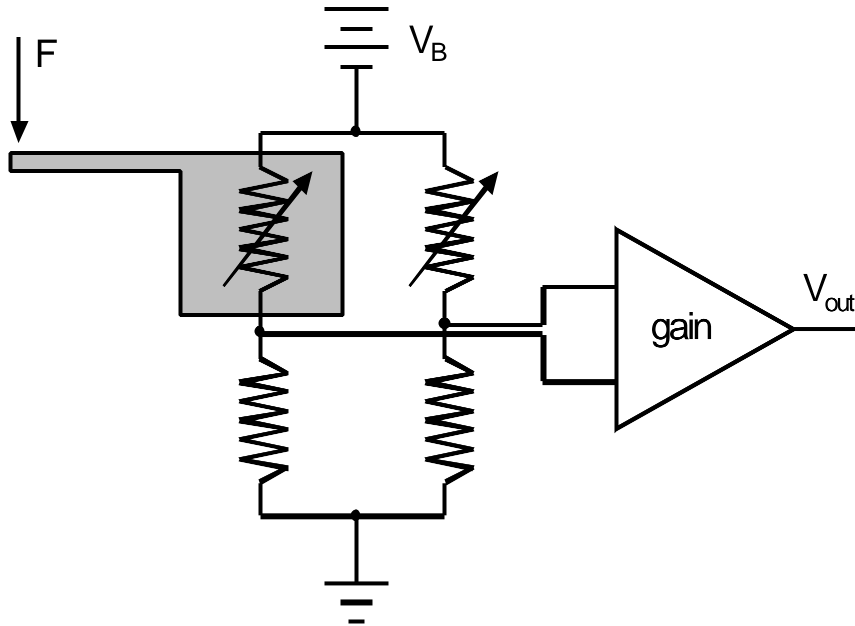

Figure 2-1. Piezoresistive cantilever in a Wheatstone bridge circuit. The piezoresistor is half of a voltage divider, so as the resistance changes, the output voltage varies. The other half of the bridge is another voltage divider, balanced with a variable resistor to null out the signal when there is no input force. An instrumentation amplifier then provides gain.

It is evident from the figure that the sensitivity can be made arbitrarily large by varying the gain of the instrumentation amplifier. For this reason, a sensitivity quotation by itself in volts per signal contains little information. Sensitivity is therefore sometimes given as a fractional change per signal, such as $\Delta R/R$ per Newton [N^{-1}] for the change in resistance of a piezoresistive force sensor. This type of sensitivity is often quoted as parts per million, where 10^{-6} N^{-1} is equivalent to 1 ppm/N. While sensitivity can be a useful metric, the real parameter of interest in most applications is resolution. To determine resolution the noise must be known.

Bandwidth

The range of frequencies that can be measured is known as the bandwidth of the measurement. The upper limit may be set with electronic filtering, or it may be set by the sampling rate of the measurement, the bandwidth of the amplifiers used, the resonant frequency of the of the cantilever, or capacitive losses in the wires, among other possibilities. The low end of the frequency bandwidth is usually set by the length of the measurement, or again by electronic filtering. For a measurement that only lasts one second, a 1 mHz signal will appear to be unchanging.

The mechanical response of a cantilever is attenuated above its resonance, so the maximum measurement bandwidth for a cantilever is usually set by its resonant frequency. The choice of the bandwidth often determines the dominant source of noise, and will therefore have a great impact on the probe design. If low frequency signals are of primary interest, high frequency noise can be neglected in the design.

Noise

For the circuit in Figure 2-1, noise is any voltage V_{out} that is present when there is no force signal applied to the cantilever. A simple measurement of the noise would be to square V_{out}, average it over time, and take the square root. If this root-mean-square (*rms*) value were 1 mV, then 1 mV signals are considered the lower limit on what can be measured.

It is usually beneficial, however, to consider the frequency distribution of the noise, computed by taking a Fourier transform of the noise waveform. If there is noise at frequencies that are not of interest to the measurement, they can be electronically filtered, effectively improving the signal to noise ratio. Simulated example waveforms are shown in Figure 2-2.

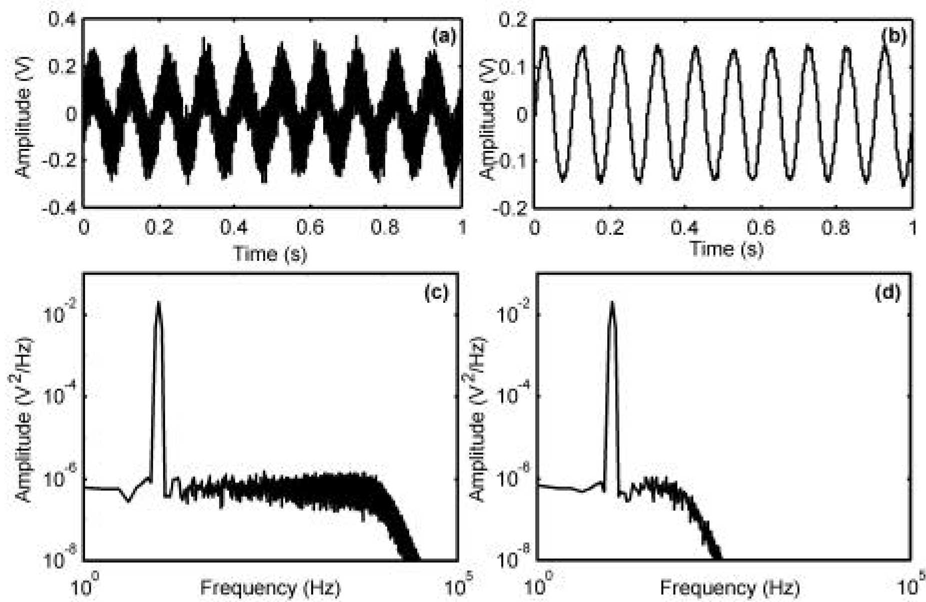

Figure 2-2. Matlab simulated signals in the presence of white noise. (a) shows a 100 mVrms signal at 10 Hz in a 10 kHz measurement bandwidth. (b) shows the same waveform after a filter at 100 Hz. (c) and (d) show the power spectral density of the waveforms.

Because the total noise depends on the measurement bandwidth, the power spectral density (PSD) [V^2/Hz] of the noise is often quoted. The PSD is a measure of the signal power in a given 1 Hz frequency band. Although V^2 are not units of power [W], it is assumed to be the power dissipated in a 1 Ω resistor. To get the total power of two incoherent sine waves, the squared amplitudes must be added. By summing the PSD at each frequency over the bandwidth, the total noise can be computed. As an example, the white noise in Figure 2-2 has power spectral density of $6{\cdot}10^{-7}$ V^2/Hz, so the unfiltered noise in a 10 kHz bandwidth had a total noise power of $(6{\cdot}10^{-7}\ V^2/Hz){\cdot}(10^5\ Hz) = 0.06\ V^2$ or 0.24V. After filtering to a 100 Hz bandwidth, the noise is 0.008 V.

In addition to simply filtering a waveform to remove noise, it is sometimes also possible to remove noise by using a lock-in amplifier. A lock-in amplifier multiplies the incoming waveform by a reference sine wave. Consider a sine component of the signal

with amplitude A_1 at frequency ω_1. If the lock-in reference signal had unit amplitude and frequency f_0, then the output signal is given by

$$A_1 \sin(\omega_1 t)\sin(\omega_0 t) = \frac{A_1}{2}\sin((\omega_0 - \omega_1)t) + \frac{A_1}{2}\sin((\omega_0 + \omega_1)t) \qquad (2.1)$$

Half the power of the frequency components of the signal waveform near f_0 will be shifted to DC, and the other half shifted to $2f_0$. The DC components can then be filtered with a low-pass filter of bandwidth B. This is effectively the same as having a narrow band pass filter of bandwidth $\pm B$ centered at frequency f_0.

In addition to use as a tracking band pass filter, the multiplier function of a lock-in can also be used to move a low frequency signal up to a higher frequency, and back, if desired. This technique is used in "chopped" op-amps to circumvent low frequency noise. Chopping a signal to remove noise is only possible if the signal can be frequency shifted before introduction of the noise. As an example, low frequency resistance drift of a piezoresistor cannot be removed by chopping, because the drift noise is introduced at the same point and time as the signal, and the two cannot be separated.

Resolution

The resolution of the probe determines the minimum force or displacement that can be measured. Resolution is defined as the noise divided by the sensitivity. The total amount of noise is dependent on the bandwidth of the measurement, since filters can remove noise outside the bandwidth of interest. As a result, resolution should be quoted as the minimum detectable force or displacement in a given bandwidth. This is often given as $N/\sqrt{Hz}$ or $m/\sqrt{Hz}$ for measurements in a 1 Hz bandwidth. If the noise is constant as a function of frequency, such a measure is sufficient to compute the resolution in any bandwidth. If the noise level varies irregularly with frequency, however, the total

resolution should be given for the relevant bandwidth, as in 5 nN in a bandwidth from 10 Hz to 1 kHz.

Spring constant

The spring constant, k [N/m], of a cantilever beam is also critical to the usefulness of the sensor. In the discussion of section 3.3, it will be shown that increasing the stiffness of a cantilever improves its displacement sensitivity, while decreasing the stiffness improves the force sensitivity. This observation by itself would suggest a short, thick, stiff cantilever for displacement measurements such as surface imaging, and a long, thin, soft cantilever for force measurements. There are other restrictions on the cantilever stiffness, however.

The disadvantages of an extremely stiff cantilever are readily apparent. For contact AFM imaging, a stiff cantilever will exert large forces that may damage the sample or result in tip wear. For imaging solids, acceptable forces are in the 1-10 nano-Newton range. For imaging biological samples, the forces must be below ~0.1 nN. The disadvantages of a soft cantilever as a force sensor are somewhat subtler, and will be discussed in the section 2.2.

Other parameters

There are many other parameters used to specify sensor performance, such as linearity, dynamic range, accuracy and drift. Linearity and dynamic range are not usually discussed for AFM sensors because the probes are typically used in a feedback mode where the goal is to keep a constant force on the cantilever. For force measurements, they should be important figures of merit, but the signals usually involve such small displacements that linearity is assumed. The signals are also typically so close to the noise limits of the sensor that both concerns are secondary to the need for resolution. As

AFM force curve measurements become a more widespread and rigorous scientific tool, dynamic range and linearity should gain importance as figures of merit.

Drift is simply a measure of the noise in a particular, low frequency, bandwidth, and should therefore be superfluous if resolution is quoted correctly.

Accuracy is rarely mentioned for AFM force measurements. AFMs measure displacement accurately, and the spring constant of the cantilever is used to infer the forces. The accuracy to which the spring constant is known is usually the limiting factor in the accuracy of a force measurement. Although several approaches have been devised, there is still no convenient way to calibrate the stiffness of an AFM probe and get results with much better than 20 percent accuracy. The displacement resolution of an AFM probe can be accurately determined by applying known displacements to the probe. These calibration displacements can be applied with a piezo-electric actuator that has been previously calibrated using another known sensor, such as a laser interferometer. To calibrate a force sensor, however, the spring constant must be known. This allows the conversion of known displacements into known forces.

There are numerous methods that have been used to compute or measure cantilever spring constants. The most common is simply to make a good measurement of the cantilever dimensions and compute the theoretical spring constant. The spring constant varies as the cube of the thickness and length, so measurement inaccuracies result in large spring constant errors. The largest error is typically associated with the thickness measurement. A measurement of the resonant frequency can be used to get another estimate of the thickness, which helps with the accuracy of this technique[1].

Alternatively, known masses can be applied to the end of the beam, and the resulting resonance shifts measured[2]. This method can be accurate if the masses are accurately known and their location on the beam is well determined, but it primarily suffers from the

inconvenience of the method. Micro-manipulating 10 μm-diameter beads is a time consuming task, and likely as not to result in a broken cantilever.

If the spring constant of a single cantilever is accurately established, it can theoretically be then used to apply known forces to other cantilevers and thereby calibrate them. It is surprisingly difficult to repeatably calibrate a second cantilever in this manner, however. Slight tilt in the relative orientation of the beams and lateral motion during the loading apply buckling loads that introduce substantial errors.

A final technique is to make use of the intrinsic thermal noise of the cantilever. There is Brownian motion in any mass-spring system that has an expectation value proportional to the temperature and one over the spring constant. The spring constant can then be deduced from a measure of the thermomechanical displacement and the temperature. The major difficulty with this approach is getting an accurate measure of the minute thermomechanical motion over a broad frequency range.

2.2. Force instabilities

Attractive force instabilities and probe stiffness

The snap-in and snap-out of the cantilever force curve shown in Figure 1-3 results in a region in which the forces cannot be measured, fundamentally limiting the usefulness of the technique. These instabilities arise when the attractive force gradient from the interaction with the surface exceeds the cantilever spring constant.

The instability can be understood by looking at a static balance of forces. The cantilever tip will be stationary when the restoring force from the flexing of the cantilever, $F=kx$, equals the attractive force from the surface. As the cantilever base moves closer to the surface, the attractive force increases, causing further bending of the cantilever until equilibrium is again reached. This bending of the cantilever moves the tip

still closer to the surface in turn increasing the attractive forces. If the situation arises where these surface forces are increasing faster than the restoring force of the flexing beam, the tip snaps down. The rate at which the restoring force increases ($dF/dx = k$) is the spring constant. Therefore, when the attractive force gradient exceeds the spring constant, snap-down occurs. A similar phenomena causes snap-in for electrostatic actuators commonly used in MEMS devices.

Figure 2-3 illustrates the attractive forces from a Leonard-Jones potential of the form $-Ad^{-6}+Bd^{-12}$, where A and B are constants and d is the distance from the surface. Typical values for A and B of single atoms are 10^{-77} J·m^6 and 10^{-134} J·m^{12}.[3] A 0.01 N/m cantilever probing this interaction would snap in 0.67 nm from the surface at a force of 1 pN. Upon retracting the cantilever it would snap free 0.39 nm from the surface at a force of 22 pN, and end up at a new equilibrium 2.3 nm from the surface. In addition to this force vs. distance curve, for each position of the cantilever base a line of slope k can be plotted of the force versus distance due to the cantilever bending. Two such contours are indicated, one at snap-in and one at snap out, where they are tangent to the surface potential force curve.

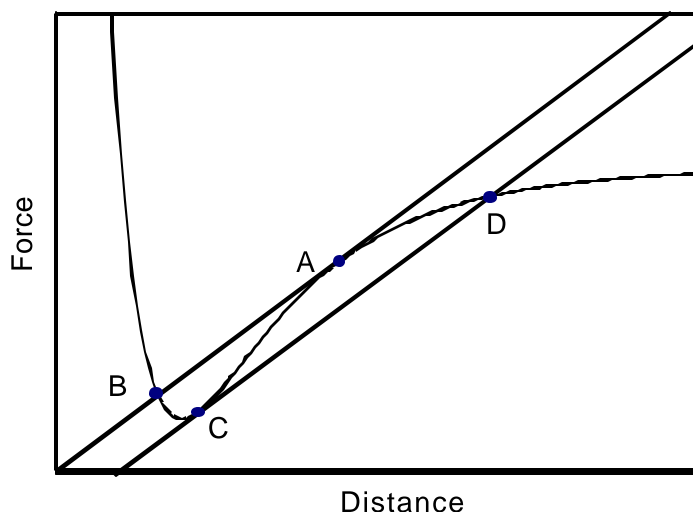

Figure 2-3. Diagram of an attractive force potential versus distance with contours of the cantilever spring constant. For an approach, point A indicates snap-in. The forces then balance and achieve equilibrium at point B. When retracting the cantilever snaps free at point C and comes to equilibrium at point D.

The region between points A and C of this force potential cannot be mapped using this cantilever. To fully map out this force potential requires a cantilever of stiffness greater than the maximum slope of the force potential.

Although snap-out due to van der Waals forces can be observed, the most commonly observed snap-outs are the result of meniscus forces from condensation and other contaminants[4]. The attractive force of the meniscus is usually 10-100 nN[5].

Force instabilities in molecular manipulation

The instabilities described in the preceding section are well known to AFM users, but a less familiar variation of this problem exists for force measurements on macromolecules. Consider again the DNA unzipping experiment described in section 1.1, and diagrammed in Figure 1-4. For the case of a strong bond followed by a weaker bond, force-gradient instabilities may prevent measurement of the weaker bond.

When measuring the first, strong bond, the cantilever will flex until the beam restoring force is great enough to break the bond. The free end of the cantilever will then spring back until it either reaches zero deflection, or catches on the next bond in the sequence, a distance $\boldsymbol{d}$ away. If it catches a second bond before completely relaxing, the cantilever at this point exerts a force equal to the force of the first bond minus $k\boldsymbol{d}$. If this remaining force is enough to break the second bond, the cantilever will simply rip through that bond as well, without recording it as a discrete event.

For the DNA unzipping experiment discussed in Chapter 1, 10-15 pN forces were required to rupture the individual complementary strand bonds[6]. According to these results, the A-T pair, composed of two hydrogen bonds, should rupture at ~10 pN, and the C-G pair, composed of three hydrogen bonds, at ~15 pN. The spacing between the bond pairs in double-stranded DNA is 0.34 nm, which means that for unzipping the cantilever tip can move 0.68 nm before catching the next bond. To measure a C-G followed by an A-T, then, the cantilever must have a spring constant of greater than 5 pN/0.68 nm=0.007 N/m in order to stop on the weaker bond. In other words, the spring constant of the beam must be greater than the force gradient between the two bonds.

In fact, matters will be even worse than this, since the cantilever will have some inertia when it reaches the next bond. Even if the cantilever has room to reach zero deflection before the next bond, for any quality factor greater than one it will have some overshoot that could rupture the subsequent bond. To be certain that instabilities and dynamic effects are not affecting the measurement, the cantilever should ideally never deflect more than half the distance between bonds. This criterion allows for maximum overshoot, so that as long as the oscillations are allowed to settle before the next event, each can be measured independently. In the example of the previous paragraph, the cantilever could have a minimum spring constant of 15 pN/0.34 nm=0.04 N/m. This type of instability will prevent researchers using soft devices such as thin pipettes or optical

tweezers from resolving all the individual bond ruptures when mechanically denaturing DNA.

A major drawback to this type of approach for sequencing is that as the double helix becomes unzipped it acts as another spring attached to the end of the cantilever. Now the net effective spring constant between the base of the cantilever, which is controlled, and the point where bonds are breaking is $k_{eff} = (k_{cantilever}^{-1} + k_{DNA\ strand}^{-1})^{-1}$. It is this spring constant which will now set the unzipping instability point. As the unzipped strand becomes longer, its spring constant decreases, thereby lowering the overall effective spring constant of the system. The elasticity of the DNA will likely limit this type of sequencing to strands below one kilo-base-pair in length.

References

1. J. E. Sader, I. Larson, P. Mulvaney, and L. R. White, "Method for the calibration of atomic force microscope cantilevers," *Rev. Sci. Inst.*, vol. 66, no. 7, pp. 3789-3798, 1995.

2. J. P. Cleveland, S. Manne, D. Bocek, and P. K. Hansma, "A nondestructive method for determining the spring constant of cantilevers for scanning force microscopy," *Rev. Sci. Inst.*, vol. 64, no. 2, pp. 403-405, 1993.

3. Israelachvili, J., *Intermolecular and Surface Forces,* 2th ed., Academic Press Inc., London, 1992.

4. A. L. Weisenhorn, P. K. Hansma, T. R. Albrecht, and C. F. Quate, "Forces in atomic force microscopy in air and water," *Appl. Phys. Lett.*, vol. 54, no. 26, pp. 2651-2653, 1989.

5. Baselt, D. R., *The tip-sample interaction in atomic force microscopy and its implications for biological applications*, Ph.D. Thesis, California Institute of Technology, 1993.

6. B. Essevas-Roulet, U. Bockelmann, and F. Heslot, "Mechanical separation of the complementary strands of DNA," *Proc. Natl. Acad. Sci.*, vol. 94, pp. 11935-11940, 1997.

Chapter 3. Design for Sensitivity and Bandwidth

In this chapter fundamental equations are derived which determine the sensitivity and the mechanical characteristics of the cantilever. This derivation primarily indicates the relation between the stress in the beam and the distribution of the dopant, which in turn determines the current flow in the cantilever. A similar set of equations was presented by Tortonese in his 1993 thesis[1], and has been the basis for most cantilever designs since.

Such designs, based purely on the goal of maximizing sensitivity within some mechanical constraints of spring constant and bandwidth, have the implicit assumption that the noise of the device will be largely unaffected by these design decisions. As will be shown in Chapter 4, this assumption is invalid for some cases, but in many instances, design for maximum sensitivity does lead to substantial performance gains.

3.1. Mechanical properties of a cantilever beam

The spring constant, k, of a rectangular diving-board cantilever is given by

$$k = \frac{Ewt^3}{4l^3}, \tag{3.1}$$

where w, l, and t, are the width, length and thickness of the beam, and E is the modulus of elasticity of the material. For cubic crystals such as silicon, the modulus of elasticity depends on the crystal orientation according to[2]

$$E^{-1} = s_{11} - 2\left(s_{11} - s_{12} - \tfrac{1}{2}s_{44}\right)\Gamma, \tag{3.2}$$

where

$$\Gamma = \boldsymbol{g}_1{}^2\boldsymbol{g}_2{}^2 + \boldsymbol{g}_2{}^2\boldsymbol{g}_3{}^2 + \boldsymbol{g}_3{}^2\boldsymbol{g}_1{}^2, \qquad (3.3)$$

and $\boldsymbol{g}_1$, $\boldsymbol{g}_2$, and $\boldsymbol{g}_3$ are the direction cosines between the axis of interest and the three standard crystal axes. For example, the angle between the [110] direction and the x-axis is 45 degrees, so γ_1 is $\sqrt{2}/2$. For silicon, s_{11} is $0.77 \cdot 10^{11}$ m^2/N, s_{12} is $-0.21 \cdot 10^{11}$ m^2/N and s_{44} is $1.25 \cdot 10^{11}$ m^2/N[3]. The modulus of rigidity, G, can be calculated from the same coefficients according to

$$G^{-1} = s_{44} + 4\left(s_{11} - s_{12} - \tfrac{1}{2}s_{44}\right)\Gamma, \qquad (3.4)$$

The resulting Young's moduli for silicon in the predominant crystallographic directions are given in Table 3-1. Piezoresistive cantilevers are usually constructed on <100> wafers, so along the dominant strain axis the <110> value of 1.7×10^{11} N/m is used.

	E (GPa)	**G (GPa)**	**$\boldsymbol{r}$ (kg/m^3)**
Si <100>	166	80	
Si <110>	170	62	2333
Si <111>	190	58	

Table 3-1. Modulus of elasticity (E), modulus of rigidity (G) and density ($\boldsymbol{r}$) for silicon and silicon nitride. The values for the <100> and <111> are the extremes.

The resonant frequency for a cantilever is[4]

$$f_0 = \boldsymbol{a}_n \frac{t}{l^2}\sqrt{\frac{E}{\boldsymbol{r}}} \qquad (3.5)$$

where $\boldsymbol{r}$ is the material density (2300 kg/m^3 for silicon) and $\boldsymbol{a}_n$ are coefficients for the various resonant modes. For the fundamental mode, $\boldsymbol{a}_1 = 1.01$, so the fundamental resonance is often approximated without the $\boldsymbol{a}$ parameter. The next resonant modes occur at $\boldsymbol{a}_2 = 6.36$, $\boldsymbol{a}_3 = 17.81$, and $\boldsymbol{a}_4 = 34.90$.

3.2. Stress distribution in a cantilevered beam

When a transverse load F is applied to the end of a cantilever, as in Figure 3-2, the stress, $\boldsymbol{s}$, in the beam is proportional to the resulting moment M according to

$$\boldsymbol{s} = \frac{Mc}{I}, \tag{3.6}$$

where the bending moment $M=F(l-y)$ and for a rectangular beam $I=wt^3/12$. The stress is then given as

$$\boldsymbol{s} = \frac{12(l-y)c}{wt^3} F\ . \tag{3.7}$$

For a beam loaded as shown, the top half of the is in tensile stress along the [110] direction, and the bottom half is in compression. At the center of the beam is a layer called the neutral axis, which experiences zero stress. To first order approximation, the stress distribution increases linearly from the tip of the cantilever to the base, and varies linearly across the beam thickness. Halfway through the thickness of the beam, there is a point of zero stress, where there is a transition from a tensile stress to a compressive one. The plane of these points along the length of the cantilever is called the neutral axis. The variable c denotes the distance from the neutral axis.

As can be seen in Figure 3-1, equation (3.12) breaks down near stress concentrators such as sharp corners, or notches in the beam. The stress also extends beyond the base of the cantilever into the substrate. For many analyses, including this one, the approximation of linearly varying stress is sufficient. According to equation (3.7), the stress increases linearly from the end of the cantilever to the base, and linearly from the neutral axis out to the surface.

Figure 3-1. Finite element model showing the stress distribution in a cantilever beam. The stress increases linearly along the length from the tip to the base, and also linearly across the thickness. The bottom half is in compression and the top half in tension.

A triangular beam could be used instead of the rectangular beam shown, and would have the advantage that the width, and hence the area moment of inertia, *I*, also increases linearly from the tip to the base. Such a beam would be no more likely to fail under a load, would have a constant stress along its length, and would have a higher resonant frequency. Because most piezoresistive cantilevers have been rectangular, a rectangular beam will be used in the remainder of this treatment.

3.3. The piezoresistive coefficient

To compute the sensitivity of a piezoresistor, expressed as $\Delta R/R$ per Newton, for a cantilever with arbitrary dopant profile, the effects of the stress and dopant distribution must be analyzed. The stress varies across both the thickness and length of the beam, and the dopant profile varies across the thickness, so a complete derivation of the net effect must involve integration along both these axis.

A piezoresistor with cubic symmetry responds to stress as

$$\frac{\Delta \boldsymbol{r}}{\boldsymbol{r}} = \boldsymbol{p}_l \boldsymbol{s} \,, \qquad (3.8)$$

where $\boldsymbol{s}$ is the resistivity and $\boldsymbol{p}_l$ is the longitudinal piezoresistive coefficient, along the direction of the tensile stress. There also exists a transverse piezoresistive coefficient, usually denoted as $\boldsymbol{p}_t$. Analogously to the derivation of the modulus of elasticity, the piezoresistive coefficients are determined by π_{11}, π_{12}, and π_{44}. The direction cosines are again used to determine π_l and π_t in any other direction, according to

$$\boldsymbol{p}_l = \boldsymbol{p}_{11} - 2(\boldsymbol{p}_{11} - \boldsymbol{p}_{12} - \boldsymbol{p}_{44})\Gamma \,, \qquad (3.9)$$

and

$$\boldsymbol{p}_t = \boldsymbol{p}_{12} - 2(\boldsymbol{p}_{11} - \boldsymbol{p}_{12} - \boldsymbol{p}_{44})\Gamma \,. \qquad (3.10)$$

Coefficients for p-type and n-type silicon are given in Table 3-2. These numbers are given for low doping levels, and therefore represent the maximum coefficients. For a [100] wafer, the maximum piezoresistive coefficient occurs in the [110] direction, where Γ is ¼. This results in a $\boldsymbol{p}_l$ for p-type silicon along the [110] direction of $71.8 \cdot 10^{11}$ m^2/N. Although higher values of $\boldsymbol{p}_l$ can be obtained with n-type silicon, the high piezoresistive coefficient occurs in directions that are inconvenient from a fabrication point of view. A graphical representation of the piezoresistive coefficients is available in the work of Kanda[5].

	p_{11} [10^{11} m^2/N]	p_{12} [10^{11} m^2/N]	p_{44} [10^{11} m^2/N]
n-type silicon (11.7 W-cm)	-102.2	53.4	-13.6
p-type silicon (7.8 W-cm)	6.6	-1.1	138.1
n-type germanium (9.9 W-cm)	-4.7	-5.0	-137.9
p-type germanium (15 W-cm)	-10.6	5.0	46.5

Table 3-2. Piezoresistive coefficients for n-type and p-type silicon and germanium[6].

3.4. Piezoresistor sensitivity

Subsequent calculations will assume a cantilever with the design shown in Figure 3-2. The total thickness of the cantilever is t. The path of the piezoresistor is defined by splitting the cantilever base into two legs of length l_{leg} that extend some fraction of the total length l. The gap between the legs is assumed to be of negligible width, so that the total cantilever width is w and the legs are of width $w/2$. A summary of all the variables used in this paper can be found in appendix A.

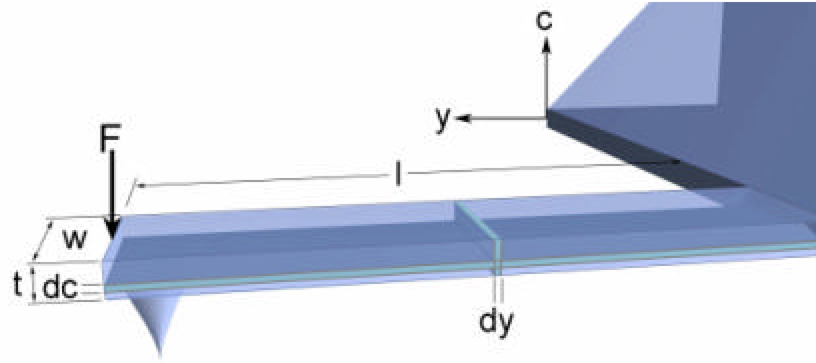

Figure 3-2. Diagram of integration variables and cantilever dimensions.

First consider a thin horizontal slice *dc* of the cantilever, where *c* is the distance from the neutral axis of the beam, as shown in Figure 3-2. For an infinitesimally thin slice, the stress and dopant are constant as a function of thickness. A differential length *dy* of thin vertical slice has resistance of

$$dR_{slice} = \frac{\mathbf{r}\, dy}{w\, dc}, \tag{3.11}$$

where $\mathbf{r}$ is the is the resistivity. The resistance from each vertical slice is added in series, giving the resistance for a full horizontal slice is

$$R_{slice} = 2\int_{0}^{l_{leg}} \frac{\mathbf{r}\, dy}{w\, dc} = \frac{2\,\mathbf{r}\, l_{leg}}{w\, dc}, \tag{3.12}$$

with the factor of two entering because there are two legs. The resistance contribution where the current changes direction to the return leg is neglected.

The analogous calculation for $\mathbf{D}R_{slice}$ is where the piezoresistive effect enters. When stressed, the resistance in this element varies according to equation (3.8) as

$$\Delta\left(dR_{slice}\right) = \frac{\Delta \boldsymbol{r}\, dy}{w\, dc}\,. \tag{3.13}$$

The change in resistance of the full slice is therefore

$$\Delta R_{slice} = 24\int_0^{l_{leg}} \frac{\boldsymbol{r}\boldsymbol{p}_l (l-y)c}{w^2 t^3 dc} F dy\,, \tag{3.14}$$

which when integrated gives

$$\Delta R_{slice} = 24\frac{\boldsymbol{r}\boldsymbol{p}_l (l-\frac{l_{leg}}{2})c l_{leg}}{w^2 t^3 dc} F\,. \tag{3.15}$$

For a single slice, then, the sensitivity ΔR/R is

$$\frac{\Delta R_{slice}}{R_{slice}} = 12\frac{\boldsymbol{p}_l (l-\frac{l_{leg}}{2})c}{wt^3} F\,. \tag{3.16}$$

The maximum possible signal occurs at the surface, when $c=t/2$. If the doped region exists only at the surface, there are no other resistance contributions and the sensitivity is

$$\frac{\Delta R}{R} = \frac{6\boldsymbol{p}_l (l-l_{leg}/2)}{wt^2} F\,. \tag{3.17}$$

By including the spring constant of the cantilever, and the relation $F=kx$, a similar equation can written for the maximum sensitivity to a displacement,

$$\frac{\Delta R}{R} = \frac{3\boldsymbol{p}_l Et\left(l-l_{leg}/2\right)}{2l^3} x\,. \tag{3.18}$$

The change is resistance is usually measured by making the piezoresistor one quarter of a Wheatstone bridge, so the measured output is $V_{out}= (\boldsymbol{D}R/R)(V_{bias}/4)$.

3.5. Non-ideal dopant distributions

Equations (3.17) and (3.18) are simplified by the assumption of only measuring the stress at the surface. For a better model of the total fractional resistance change, Tortonese formulated an efficiency factor ***b*** to be inserted in the numerator of the sensitivity equations[1]. ***b*** is computed as the ratio of the complete ΔR/R, which includes the distribution of the stress and dopant, to a simplified version in which the stress is assumed to be at the surface value. As such the efficiency factor which ranges between 0 and 1.

To compute the full sensitivity equations (3.12) and (3.14) can be integrated to sum the contributions of each horizontal slice across the beam thickness. Since these are resistors adding in parallel, it is convenient to convert to conductance to carry out the integration. The conductance G is defined as $1/R$, and it is easily shown that

$$\frac{\Delta R}{R} = -\frac{\Delta G}{G}. \tag{3.19}$$

The total conductance is

$$G = \int_{-\frac{t}{2}}^{\frac{t}{2}} \frac{w}{2\boldsymbol{r}(c) l_{leg}} dc , \tag{3.20}$$

where the resistivity now varies in across the thickness depending on the dopant profile, so the integral cannot be solved in a closed form.

The change in conductance can be rewritten from equation (3.19) as

$$\Delta G = -\frac{\Delta R}{R^2}, \tag{3.21}$$

so the contribution of a single slice is

$$\Delta G = -\int_{-\frac{t}{2}}^{\frac{t}{2}} \frac{6\boldsymbol{p}_l F(l - \frac{l_{leg}}{2})c}{t^3} \frac{dc}{\boldsymbol{r} l_{leg}} . \tag{3.22}$$

Finally the full sensitivity is

$$\frac{\Delta R}{R} = -\frac{\Delta G}{G} = \frac{3\boldsymbol{p}_l (l - \frac{l_{leg}}{2})}{wt^3} \frac{\int_{-\frac{t}{2}}^{\frac{t}{2}} \frac{c}{\boldsymbol{r}(c)} dc}{\int_{-\frac{t}{2}}^{\frac{t}{2}} \frac{1}{\boldsymbol{r}(c)} dc} F . \tag{3.23}$$

This form is generally too complex to be of use for design calculations, hence the factor $\boldsymbol{b}$. Comparing this with the simplified equation assuming maximum surface stress, and accounting for the difference with $\boldsymbol{b}$ yields

$$\boldsymbol{b} = \frac{2}{t} \frac{\int_{-t/2}^{t/2} \boldsymbol{p}_l(p) \boldsymbol{m}(p)\, p\, c\, dc}{\int_{-t/2}^{t/2} \boldsymbol{p}_l(p) \boldsymbol{m}(p)\, p\, dc} , \tag{3.24}$$

where the resistivity has been expanded according to $\boldsymbol{r}=(\boldsymbol{p}_l \boldsymbol{m} q)^{-1}$. Both the piezoresistive coefficient, $\boldsymbol{p}_l$, and the hole mobility, $\boldsymbol{m}$, are functions of the dopant concentration p.

The advantage of thin piezoresistors

Of the key performance parameters, sensitivity, resonant frequency and spring constant all improve with reduced cantilever thickness. From the simplified force sensitivity equation (3.17), it is evident that reducing the thickness will improve the sensitivity, but decreasing the thickness without adjusting the length will decrease the spring constant, so this by itself is not a complete metric.

Consider the effect of a thickness reduction while maintaining a fixed spring constant. From equation (3.1) the spring constant is proportional to t^3/l^3, so t and l can be reduced together without affecting the stiffness. The force sensitivity from equation (3.17) varies as l/t^2, so it is evident that a thinner, shorter cantilever results in a net force sensitivity improvement. The spring constant is usually specified by the demands of the application, so optimizing for force resolution given k also optimizes for displacement resolution.

The bandwidth also scales favorably with reductions in thickness. The resonant frequency is proportional to t/l^2 from equation (3.5), so again, if the thickness and length are reduced together, the spring constant remains unchanged while the resonant frequency increases.

As an example, a cantilever for high-speed AFM imaging may require a bandwidth over 100 kHz and a spring constant below 0.01 N/m to minimize sample damage. From equation (3.5) for the resonant frequency, a minimum value for t/l^2 is specified. For a practical minimum width of 10 µm, equation (3.1) for the spring constants then applies a second constraint to the ration of t/l. To satisfy these requirements the cantilever thickness must be below 0.2 µm.

Figure 3-3 illustrates the displacement sensitivity versus thickness for lines of constant spring constant, as well as lines of constant resonant frequency. For this case, the legs are assumed to extend half of the total cantilever length, with the bias voltage of 5 V. To read force sensitivity from this plot, simply multiply the displacement sensitivity by the spring constant. The width of the cantilever in the plot is fixed at 10 µm, and the length is adjusted to achieve the desired spring constant or resonance. The design space of the cantilever in the previous example is indicated as the shaded region of the figure.

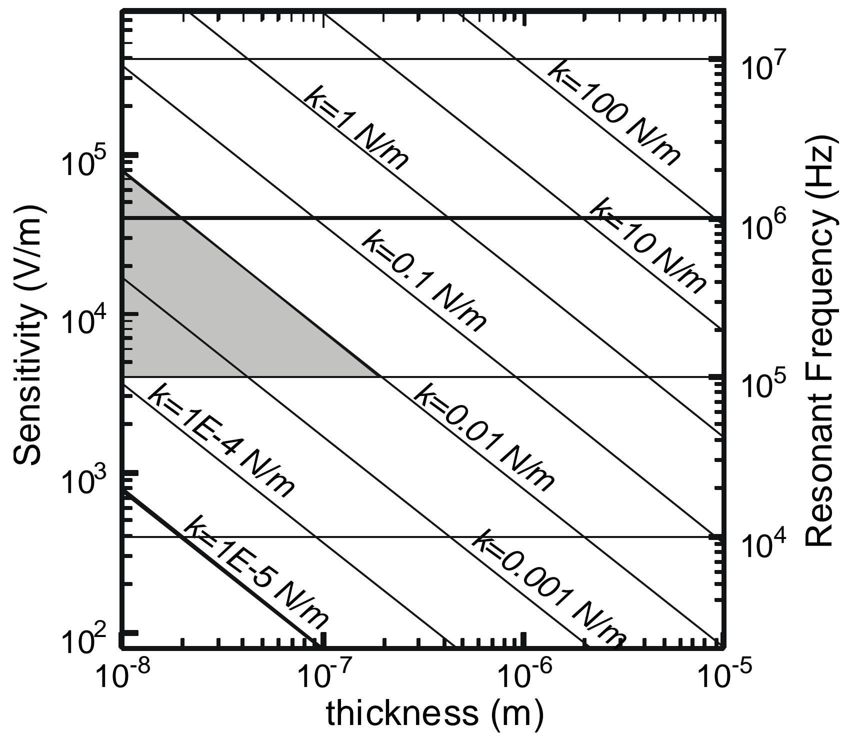

Figure 3-3. Displacement sensitivity vs. thickness for a 10 μm wide cantilever with given *k* or *f*. The horizontal lines are contours of constant resonant frequency. The sloped lines are contours of constant stiffness. The shaded region illustrates the design space for cantilevers with over 100 kHz bandwidth and under 0.01 N/m stiffness.

One drawback to the use of small cantilevers is the difficulty in approaching a surface without crashing the corners of the cantilever chip, as illustrated in Figure 3-4. Such a problem can be alleviated by piggybacking the cantilever on a stiff extension. If a 50 μm-long 0.2 μm-thick cantilever extends from the end of a 50 μm-long 2 μm-thick support cantilever, 99.8% of the deflection will occur in the thin cantilever. The effective length of the cantilever is therefore doubled, while the sensitivity is essentially unchanged.

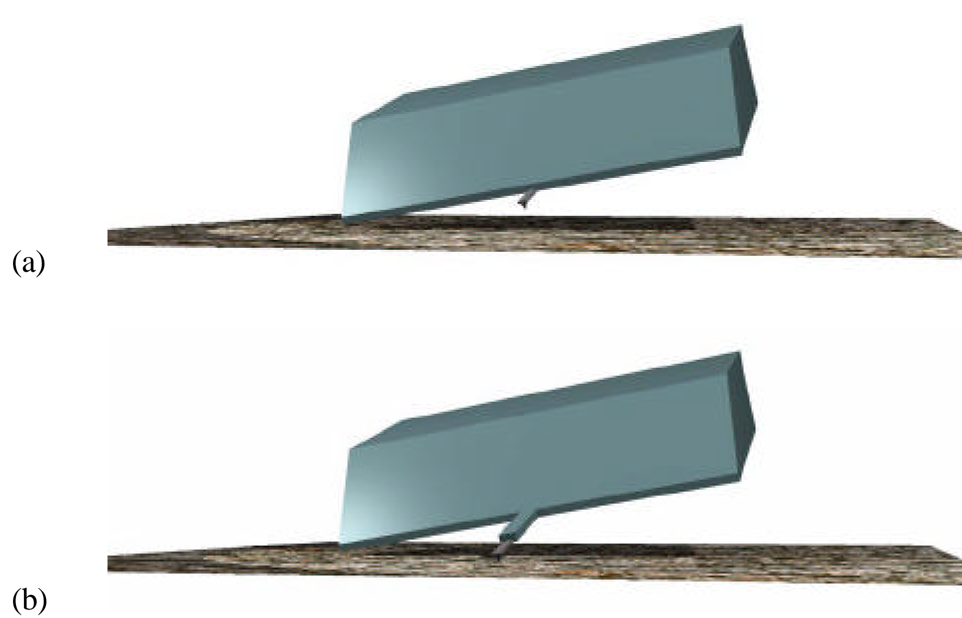

Figure 3-4. Angular alignment difficulties with short cantilevers. (a) A short cantilever can have difficulty accessing a surface because slight angular tilt of the chip may cause the chip corner to crash. This problem is alleviated in (b) by piggy-backing the short cantilever on a longer, thicker substrate.

3.6. Summary

This chapter described the fundamental equations that describe the mechanical characteristics of the beam and the sensitivity of the piezoresistor to applied forces. From these equations, it is evident that thinner, smaller piezoresistors are the route to improved characteristics.

References

1. Tortonese, M., *Force Sensors for Scanning Probe Microscopy*, Ph.D. Thesis, Stanford University, 1993.

2. Nowick, A. S. and Berry, B. S., *Anelastic Relaxation in Crystalline Solids,* Academic Press, New York, 1972.

3. J. de Launay, "The theory of specific heats and lattice vibrations," *Solid State Physics*, vol. 2, pp. 219-303, 1956.

4. Timoshenko, S., Young, D. H., and Weaver, J., *Vibration Problems in Engineering,* 5th ed., Wiley, New York, 1974.

5. Y. Kanda, "A graphical representation of the piezoresistance coefficients in silicon," *IEEE Trans Electron Devices*, vol. 29, no. 1, pp. 64-70, 1982.

6. Harris, C. M. and Crede, C. E., *Shock and Vibration Handbook,* McGraw-Hill, 1961.

Chapter 4. Constructing Ultrathin Piezoresisitve Cantilevers

It was established in Chapter 3 that thin cantilevers provide increased sensitivity and bandwidth for a given spring constant. The ability to construct thin piezoresistive cantilevers will expand the design space in ways that are physically impossible with thicker devices. In this chapter, the standard fabrication techniques for piezoresistive cantilevers will be introduced, and then modified to allow thinner devices. Data will be presented on actual devices under 1000 Å thick.

4.1. Standard Fabrication Procedure

The fabrication of piezoresistive cantilevers generally still follows the technique developed by Tortonese *et al.* A cantilever-shape is defined on the top layer of a silicon-on-insulator (SOI) wafer. It is then doped with boron to create a p-type conducting layer, a metal is deposited for contact to the doped layer, and the cantilever is released by the removal of the bulk silicon underneath it. This process is outlined in Figure 4-1.

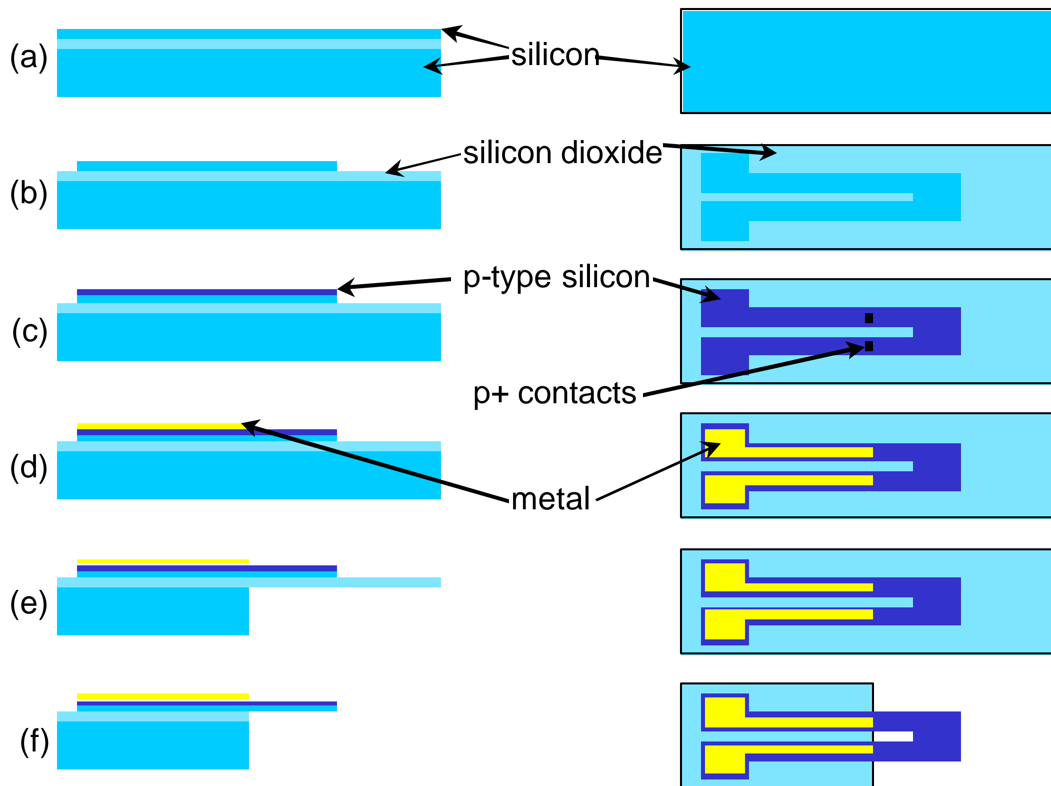

Figure 4-1. Generic process for the fabrication of a piezoresistive cantilever. (a) starting substrate of silicon-on-insulator (SOI) wafer (b) cantilever and leads are etched in top silicon (c) top silicon is boron doped through part of its thickness, and p+ contacts are implanted at the base of the cantilever (d) metal leads are deposited (e) the wafer is etched from the back side, stopping on the buried oxide (f) the oxide is removed, releasing the cantilever.

Variations on this process flow are used for most piezoresistive cantilevers. Process changes tend to involve the dopant introduction and possible coatings to improve the noise characteristics. A thin (~1000 Å) oxide is often grown after the dopant introduction in step (c), nominally to passivate dangling bonds and thereby reduce the noise. The effectiveness of this approach will be discussed in the section on piezoresistor noise in Chapter 4.

The fabrication of thinner piezoresistive cantilevers is difficult for two reasons. First, thin cantilevers are more fragile, and physically harder to release without damaging them.

Release techniques such as critical point drying[1] can be used, however, and 400 Å non-piezoresistive cantilevers have been fabricated[2]. The second fabrication difficulty is related to the electrical properties of the piezoresistor. Thin piezoresistors are difficult to fabricate because the dopant must not be allowed to spread through the cantilever thickness. As was shown in Figure 3-1 half the thickness of a loaded cantilever is in compressive stress, and the other half is in tensile stress. If the dopant is evenly distributed through the cantilever, the signal from the compressive bending stress on one side will cancel the tensile stress signal from the other.

Following their invention, the major performance advances of piezoresistive cantilevers have come through reduced thickness. At each step, different techniques have been employed to circumvent the stress-dopant distribution problem. The first substantial improvement over the original 2 to 4 µm-thick piezoresistive cantilevers by Tortonese *et al.* was by Chui *et al.*, who made 1 µm-thick cantilevers by implanting a boron-doped piezoresistor through a protective oxide and activating it with a rapid thermal anneal[3]. Pre-oxidizing the cantilevers and implanting through the oxide eliminates the diffusion from a passivating oxide growth anneal that Tortonese had used. Ried *et al.* made 0.3 µm-thick cantilevers by using a lower energy implant, again a rapid thermal anneal, and a low temperature oxide for passivation[4].

For sub-micron thick cantilevers, it is difficult to confine the dopant to only the top half of the beam, and the 0.34 µm-thick cantilevers are approaching the minimum thickness achievable with conventional ion-implantation. The damage from the implant results in transient enhanced diffusion, which causes a 1000-fold enhancement of the boron mobility, even for rapid thermal anneals[5]. Until the boron atoms find their lattice sites in the crystal, even slight anneals cause substantial diffusion of the doped layer. Annealing is required to achieve this implant activation, so some transient enhanced dopant diffusion is an inevitable consequence.

An alternative approach to improving the cantilevers is to include other resistors on the chip[6]. If a cantilever has two identical piezoresistors, it can be used as two of the resistors in the Wheatstone bridge, thereby gaining a factor of two in sensitivity. The increase in cantilever size required to accommodate two resistors requires a larger cantilever, however, so the net effect may be mitigated somewhat. A second resistor can alternatively be added elsewhere on the chip, perhaps on a dummy cantilever, in order to decrease temperature sensitivity. For most AFM measurements, the time scale is such that temperature fluctuations are not critical, but where low frequency drift is an issue, a dummy resistor can be an effective remedy.

4.2. Epitaxially grown piezoresistors

The thickness limitations of ion implantation can be overcome by using vapor phase epitaxy. In vapor phase epitaxy, a clean surface of silicon is exposed to silane and borane gasses at temperatures ranging from 800°C to 1200°C, resulting in growth of boron doped silicon layers at about 10 Å/sec at 800 °C. A 300 Å-thick boron-doped layer can therefore be grown at 800 °C in 30 seconds, during which time there is negligible diffusion. The dopant concentration is set by the concentration of the borane gas, and the epitaxy results in a step-like doping profile. This is in contrast to implanted atoms, which follow a Gaussian profile. Furthermore, the dopant is active in the lattice as grown, so an activating anneal is unnecessary and there is no transient enhanced diffusion. Some additional annealing is therefore tolerable.

A TSUPREME-IV simulation of an epitaxially grown profile is shown in Figure 4-2, both as grown and after a 3-hour wet anneal at 700°C which grows 200 Å of thermal oxide. Before the implant, the doping concentration drops almost five orders of magnitude in under 10 nm. After the anneal, there is still an order of magnitude drop in

that distance. From these profiles, cantilevers well under 100 nm thick should be possible. The validity of this simulation is shown in the experimental results of section 4.3.

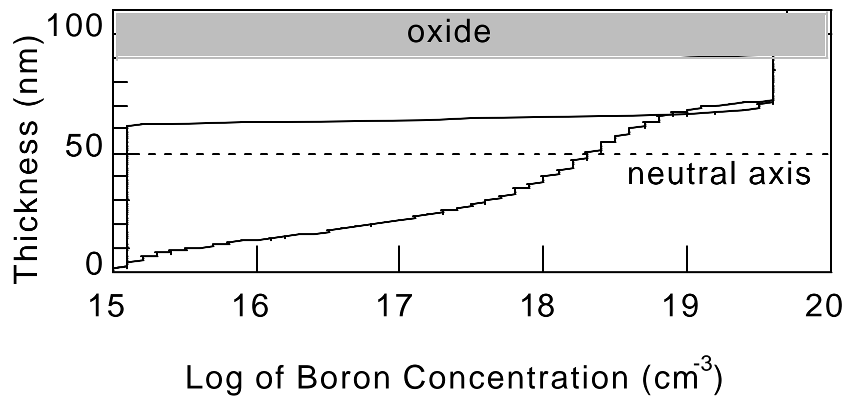

Figure 4-2. TSUPREM-4 simulations showing the dopant profile immediately following epitaxy, and after a 3-hour anneal at 700 °C.

One advantage of implantation is the ability for easy patterning with a photoresist mask. The same result can be achieved epitaxially by patterning parts of the surface with oxide, and then alternating growth steps with etching *in situ* using gaseous HCl. Silicon that is deposited on the oxide layer is amorphous and is quickly removed during the etching cycle, whereas the single crystal silicon is not. This capability is a standard feature of vapor-phase epitaxy reactors.

4.3. Detailed epitaxy fabrication procedure

The starting material for these devices was a SIMOX SOI wafer with a 2000 Å top layer of <100>, 10-20 Ω-cm p-type silicon on a 4000 Å thick oxide. The silicon layer was thinned to 800 Å by growing a thermal oxide and stripping it with buffered oxide etch (BOE). After cleaning, the wafer was loaded into the epi reactor, and cleaned in the chamber for 30 seconds in gaseous HCl. This typically removes another 100 Å of silicon.

Approximately 300 Å of epitaxial silicon was then grown at 800°C, doped to its solid solubility limit of 4×10^{19} cm^{-3}. The cantilevers were then photolithographically patterned and plasma etched, and 10^{15} cm^{-2} of boron was implanted at 30 keV for ohmic contacts.

To activate the contact implant and passivate the piezoresistor surface, 200 Å of thermal oxide was grown in a 3 hour wet anneal at 700°C. According to TSUPREM-IV simulations, previously shown in Figure 4-2, the dopant diffusion from this step is minimal. The front side processing was completed with the evaporation and patterning of aluminum leads and a 1-hour forming gas anneal at 400°C. The forming gas anneal is critical for the *1/f* noise characteristics, which are at least an order of magnitude worse without it. The effect of the 3 hour anneal, which was also included to improve *1/f* noise, is discussed further in Chapter 3.

The release for these cantilevers was done using a Bosch deep reactive ion etch (DRIE) from the back of the wafer. After the DRIE, they are still embedded in a protective photoresist on the front side and the buried SOI oxide on the back. A dip in 6:1 BOE was used to remove the oxide, and after unsuccessful attempts to cleanly remove the photoresist layer with an O_2 plasma etch, an acetone dip followed by critical point drying was ultimately used*. Upon release from the photoresist it was discovered that due to surface tension, the BOE had not cleared out the oxide at the bottom of the etch holes. A few cantilevers were set aside for reference, and the rest of the wafer was dipped in pad etch, which could access the now-exposed oxide from the front of the wafer. This etch removed both the SOI buried oxide and the 200 Å passivating oxide around the cantilevers. This accidental loss of the passivating oxide did not adversely affect the noise of the devices.

---

* Critical point drying was performed at Hewlett-Packard Labs.

4.4. Results: 100 nm-thick piezoresistive cantilevers

A variety of cantilevers between 870 Å and 900 Å thick were fabricated using the epitaxy approach. These devices represent a factor of 4 thickness reduction compared to the thinnest implanted piezoresistive cantilevers[4], and a factor of 20 reduction compared to current commercial piezoresistive cantilevers[7]. The thickness values were measured using an ultra-violet reflectometer.

The cantilevers range in length from 10 μm to 350 μm and in width from 2 μm to 44 μm, four of which are shown in Figure 4-3.

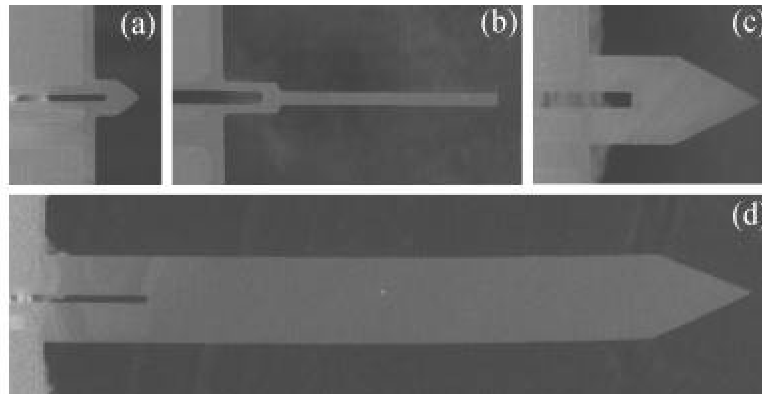

Figure 4-3. SEM of 87-91 nm-thick cantilevers. (a) 10 μm × 8 μm (b) 50 μm × 2 μm (c) 40 μm × 20 μm (d) 350 μm × 44 μm. Cantilever (d) is at a 40% scale compared to the others.

Note that there is little evidence of curling even in cantilever (d) despite the extreme length to thickness ratio of the cantilever. Although the 4×10^{19} cm^{-3} boron dopant concentration introduces some compressive stress, the stress is not large enough to pose a concern for cantilever bending.

The cantilevers range from 0.1 N/m stiffness and 2 MHz resonant frequency to 0.00003 N/m stiffness and 1kHz resonance. A general-purpose 50 μm × 2 μm wide cantilever has spring constant of 0.001 N/m and a 50 kHz bandwidth.

The sensitivity of the cantilevers was measured by using a piezoelectric actuator to press them with known deflection against a solid surface. The results for the longest cantilever, with the best force resolution, are shown in Figure 4-4. Comparing this sensitivity to that predicted by equation (3.17), gives a measured sensitivity of 70 % of the theoretical maximum, or $\boldsymbol{b}=0.7$. The value of $\boldsymbol{b}$ predicted from the simulation can be computed by integrating the profile of Figure 4-2, and results in a value of 0.65. This suggests that the simulated doping profile is a good approximation, and that the epitaxy approach is valid for thin cantilevers.

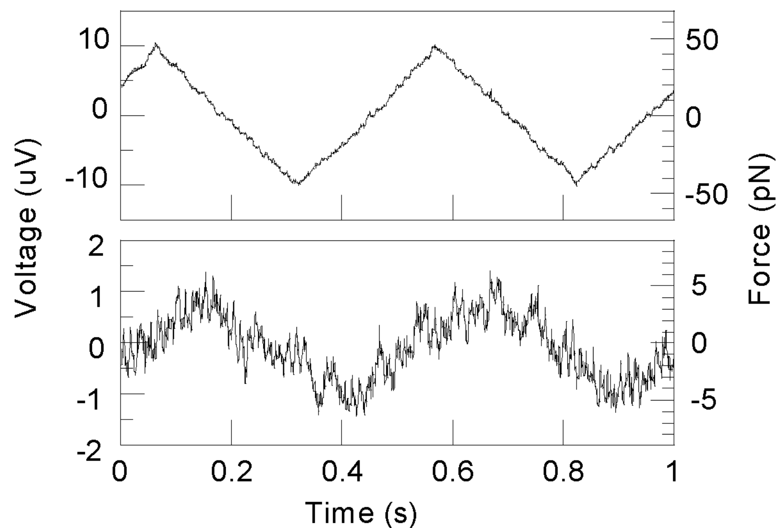

Figure 4-4. Response of 0.089 µm × 44 µm × 350 µm cantilever to 1 µm and 0.1 µm displacements. The spring constant is 0.00003 N/m, so these are forces of 33 pN and 3 pN respectively. The bandwidth is from 1 Hz to 1200 Hz.

This method of measuring sensitivity was not found to be repeatable for the longest cantilever, with results varying almost an order of magnitude, some better and some worse than this one. The problems here are analogous to those discussed in section 2.1 regarding cantilever spring constant calibration. Any slight tilt in the cantilever mounting angle introduces substantial buckling forces. The piezoelectric actuator that provided the

z-motion in the scans was also visibly introducing some unwanted motion in the x and y directions that applies a torque on the beam.

The calibration of the shorter cantilevers using direct bending with a piezoelectric tube was more repeatable, but suffered from a different problem. Misalignment of the backside etch during fabrication resulted the top silicon layer overhanging the backside cavity 20-50 µm at the base of the cantilever. The applied displacements are then absorbed by the deflection of the thin silicon layer at the base of the cantilever, reducing the measured sensitivities by up to 50%. This problem could be avoided with a thicker top substrate such as the piggy-back cantilever shown in Figure 3-4.

In order to more accurately calibrate the sensitivity of the largest cantilever, a second sensitivity measurement was made using the thermomechanical noise of the oscillator. In a vacuum, the resonance quality of this oscillator is enhanced from about 5 up to 85, and the thermomechanical motion at the resonant frequency is then visible above the other noise sources of the cantilever. This motion was measured with the piezoresistor and also with a calibrated laser vibrometer to compute the displacement sensitivity. The piezoresistor response to thermomechanical noise is shown in Figure 4-5, along with the theoretical thermomechanical noise and vibrometer data from another cantilever of the same geometry but slightly different resonant frequency. The sensitivity value of the piezoresistor in this figure is consistent with the AFM sensitivity measurement of Figure 4-4.

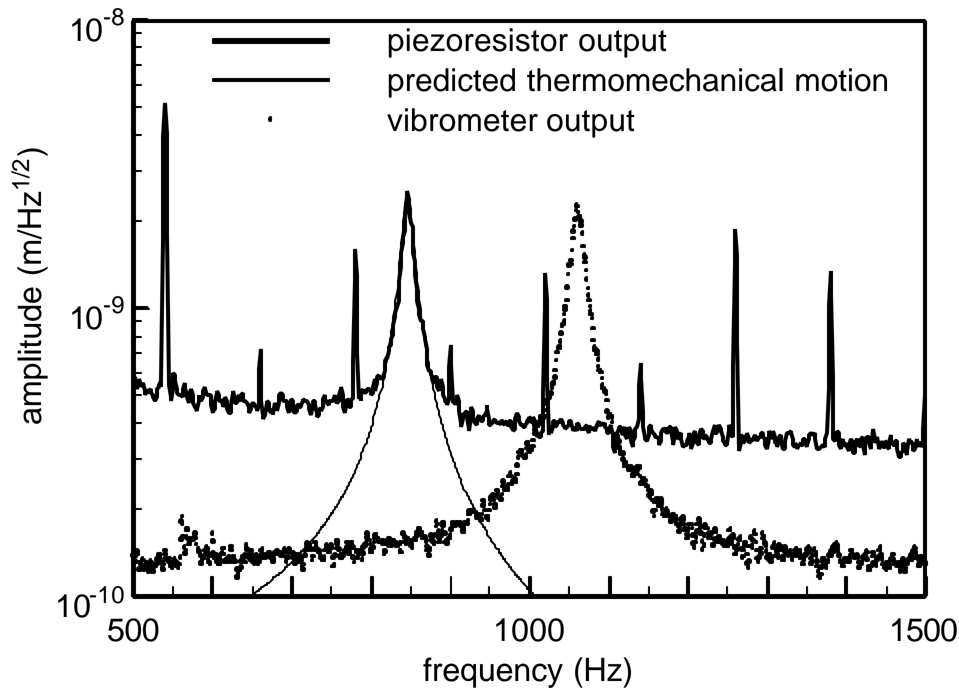

Figure 4-5. Piezoresistor response to thermomechanical noise in a 30 mTorr vacuum. The theoretical thermomechanical noise is also indicated for this oscillator with a Q of 60. The dotted points are vibrometer data from another cantilever of the same geometry but slightly different resonance. The vibrometer noise floor is a factor of 5 below that of the piezoresistor. The piezoresistor sensitivity shown here is consistent with the sensitivity of Figure 4-4.

For piezoresistive cantilevers, the most frequently quoted bandwidth is from 10 Hz to 1 kHz. In that bandwidth, the resolution of this cantilever is 500 fN. At its best frequency (near 1 kHz), it achieves a resolution level of 8 fN/√Hz. A typical commercial cantilever has force resolution of only 0.5 nN in the 10 Hz to 1 kHz bandwidth, so for pure force resolution, this cantilever represents a three order of magnitude improvement. These performance specifications are similar to those achievable using optical tweezers[8,9].

4.5. Outstanding fabrication issues

The back side etch to expose the cantilever and the final release step are the two processing steps that are most troublesome.

Back-side etching

Tortonese and Chui both used wet etches to make windows under the cantilevers and define the chip. This has the two disadvantages. The first is that the 55 degree angle of the exposed <111> planes uses a lot of real estate on the wafer. It also makes definition of the final chip problematic due to the rapid etching of convex corners. Without the ability to etch convex corners, the chip will be attached to the wafer at all four corners, and quite resistant to breaking from the wafer.

The second disadvantage of wet etching is that the front side of the wafer must be protected. Protection from tetra-methyl-ammonium hydroxide (TMAH) or potassium hydroxide (KOH) can be achieved using polyimide plus wax and a glass plate, using a layer of nitride, or single-side etcher. The polyimide-wax method was found to require close monitoring for the 8 hours of the etch, since leaks in the wax occur quite frequently. Ethylene diamine pyrochatechol (EDP), an alternative to TMAH that can be masked using only polyimide, is now unavailable in most clean rooms due to safety concerns.

Another alternative to protecting the front of the wafer is to deposit silicon nitride. On a metallized wafer, this requires a PECVD nitride chamber, and the resulting film tends to be full of pinholes through which the TMAH can penetrate. As another alternative, oxide layers proved to be an unsatisfactory TMAH mask, as oxide protected features eroded far sooner than predicted from published etch rates[10].

Because of these difficulties, most of these cantilevers were etched using the DRIE process. Such an etch stops readily on the buried oxide layer of the SOI wafer, requires little in the way of front side protection, and is not limited in the shape of the etch.

Because larger areas etch faster than slower ones, easy-to-release chips can be fabricated by taking advantage of this in the mask design shown in Figure 4-6. The central chip will be supported by the two tabs at the bottom. If the space between the chip and tab is around 10 microns, with the rest of the spaces at least 50 microns wide, the thin spaces will only be etched about halfway through the wafer, enough to allow the chip to be broken off cleanly and easily.

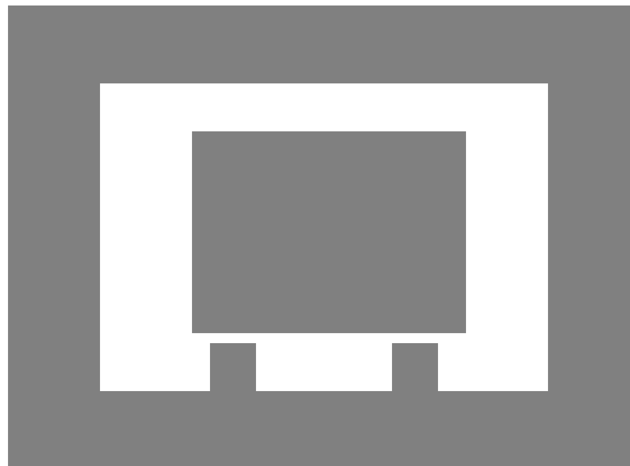

Figure 4-6. Backside release mask for DRIE release. The space between the central chip and the bottom tabs etches more slowly than the rest, so the completed chip is supported by two tabs which are pre-scored to break off cleanly.

For a more compact packing of devices, a combination of DRIE and dicing can be used. If the front of the wafer is protected with a polyimide layer, then it can be diced after the DRIE etch. In this case the backside etch holes can be just large enough to expose the cantilevers, rather than a moat surrounding the chip, as shown in Figure 4-6.

Buried oxide removal

Both a wet etch and a deep reactive ion etch stop on the buried oxide of the SOI. This oxide must then be removed. A plasma etch can be used, but if DRIE was used for the silicon removal, the sidewalls may have negative slope and will then shadow-mask the

oxide. A wet etch such as buffered hydrofluoric acid is more convenient for the oxide removal and more selective to silicon, but the surface tension tends to prevent the acid from entering the release holes. This is particularly problematic for DRIE etched wafers, which are coated with a polymer residue. Adding a surfactant (X-14) to the oxide etch does not improve matters noticeably. Simply avoiding small holes is another option, or, since the passivating oxide did not prove to be important, etching the oxide with pad etch from the front surface of the wafer is also a possibility.

Cantilever release

Another difficulty which plagues both the DRIE and the wet etch approach is in the final release of the cantilevers. Most of the cantilevers discussed in this research are too delicate to be removed directly from a liquid. As the liquid dries the cantilevers are bent backwards by the surface tension of the receding liquid-air interface until they are broken or pinned to the chip. Critical point drying is an effective technique to avert this problem, but requires specialized apparatus not found in most clean rooms.

The other option is to embed the cantilevers in membranes that protect them during drying and can then be selectively removed in a dry plasma. Organics such as polyimide or photoresist can serve this purpose, but the membrane removal proved surprisingly challenging. Frequently, even after prolonged O_2 etches tendrils of blackened polyimide or photoresist remain on the cantilevers and around the release holes, as shown in Figure 4-7. Identical wafers without release holes come perfectly clean, suggesting that it is some feature of the membrane that impedes clean removal. I postulate that because the membranes do not have silicon nearby to conduct away the heat they char into a semi-permanent form. Piranha etch ($H_2SO_4 + H_2O_2$) will also not remove these remains. This problem did not occur on all the wafers, but when did occur, it was regrettably necessary to discard the cantilevers.

Figure 4-7. Polyimide residue on FABS cantilevers after O_2 plasma release.

4.6. Summary

To address the problem of dopant spread, epitaxial growth was used to create a doped piezoresistive layer. The technique was demonstrated by the construction of high-sensitivity cantilevers under 1000 Å thick. The basic fabrication procedure, along with the major processing difficulties of the backside etch and release, was also described.

References

1. Hoen, S., Zuger, O., Yannoni, C. S., Mamin, H. J., Wago, K., and Rugar, D., "Fabrication of ultrasensitive force detectors," pp. 209-212, 1994.

2. T. D. Stowe, K. Yasumura, T. W. Kenny, D. Botkin, K. Wago, and D. Rugar, "Attonewton force detection using ultrathin silicon cantilevers," *Appl. Phys. Lett.*, vol. 71, no. 21, pp. 288-290, 1997.

3. B. W. Chui, T. D. Stowe, T. W. Kenny, H. J. Mamin, B. D. Terris, and D. Rugar, "Low-stiffness silicon cantilevers for thermal writing and piezoresistive readback with the atomic force microscope," *Appl. Phys. Lett.*, vol. 69, no. 18, pp. 2767-2769, 1996.

4. Ried, R. P., Mamin, H. J., Terris, B. D., Fan, L. S., and Rugar, D., "5 MHz, 2 N/m piezoresistive cantilevers with INCISIVE tips," pp. 447-450, 1997.

5. M. Miyake and S. Aoyama, "Transient enhanced diffusion of ion-implanted boron in Si during rapid thermal annealing," *J. Appl. Phys.*, vol. 63, no. 5, pp. 1754-1757, 1988.

6. Thaysen, J., Boisen, A., Hansen, O., and Bouwstra, S., "AFM probe with piezoresistive read-out and highly symmetrical wheatstone bridge arrangement," *The 10th international conference on solid-state sensors and actuators*, vol. 2, pp. 1852-1855, Sendai, Japan, 1999.

7. Park Scientific Instruments, *Piezolever Datasheets,* 1998

8. A. Ashkin, J. M. Dziedzic, J. E. Bjorkholm, and S. Chu, "Observation of a single-beam gradient force optical trap for dielectric particles," *Optics Letters*, vol. 11, no. 5, pp. 288-290, 1986.

9. L. P. Ghislain and W. W. Webb, "Scanning-force microscope based on an optical trap," *Optics Letters*, vol. 18, no. 19, pp. 1678-1680, 1993.

10. J. T. L. Thong, W. K. Choi, and C. W. Chong, "TMAH etching of silicon and the interaction of etching parameters," *Sensors and Actuators A (Physical)*, vol. 63, no. 3, pp. 243-249, 1997.

Chapter 5. Noise in piezoresistors

5.1. General noise observations

Piezoresistive sensors have two main noise sources, both easily distinguishable on a typical noise spectrum vs. frequency, as shown in Figure 5-1. At low frequencies, all resistors suffer from conductance fluctuations, usually called *1/f* noise because the noise power density [V^2/Hz] decreases as one over the frequency. In addition to this is Johnson noise, which is independent of frequency, and shows up on a frequency spectrum plot as horizontal line. Johnson noise is fundamental, due to thermal energy in a resistor, and is well-understood[1].

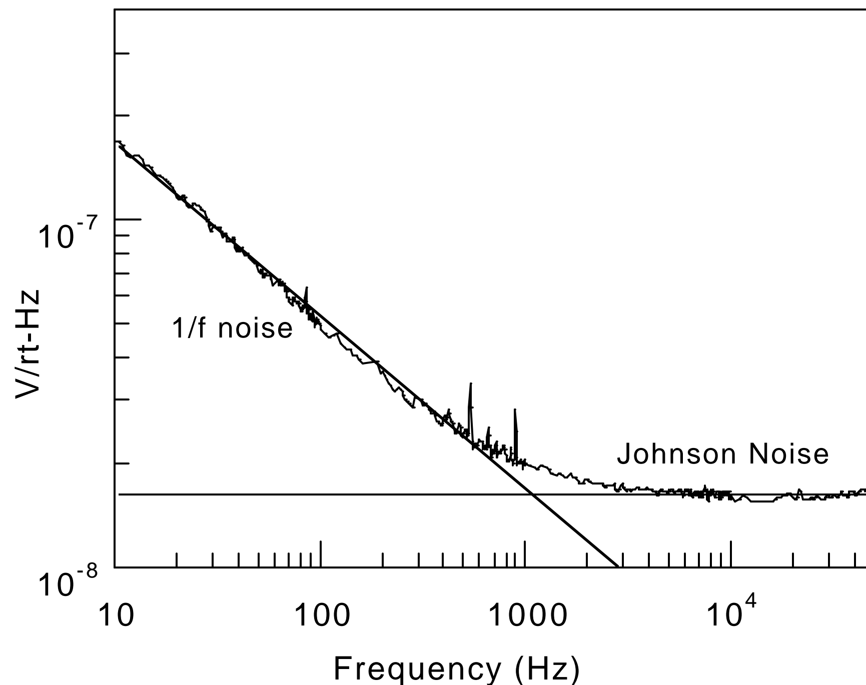

Figure 5-1. Typical measured cantilever noise spectrum from thin (1000 Å) cantilevers showing Johnson and *1/f* noise. Typical cantilevers transition from *1/f* to Johnson noise in the low hundreds of Hertz.

The cause of *1/f* noise, on the other hand, is still an active area of research, and despite the fact that it is the dominant noise source for most piezoresistors, it has not been properly included in a piezoresistor analysis. It will be shown that a 30 year-old empirical model of *1/f* noise in a resistor[2] is applicable for piezoresistors. This model has clear dependencies on the sensor geometry and processing, and provides the missing link for a complete optimization.

5.2. Johnson noise

The Johnson noise of a piezoresistor is a fundamental limit, set by the thermal energy of the carriers in a resistor, and dependent only on the resistance, R, and the temperature, T. It is white noise, independent of frequency. The voltage noise power density S_J (units [V^2/Hz]) in a measurement bandwidth from f_{min} to f_{max} is

$$S_J = 4k_B TR(f_{\max} - f_{\min}), \tag{5.1}$$

where the subscript J indicates that it is the Johnson noise.

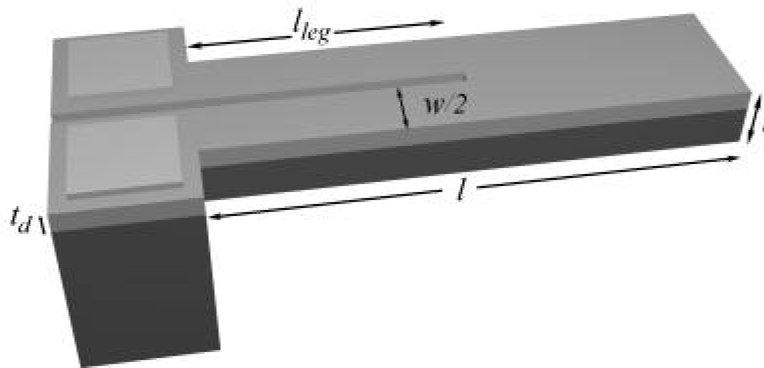

Figure 5-2. Schematic of piezoresistive cantilever with variables.

For a step doping profile of thickness t_d, the total Johnson noise depends only on the geometry and the doping. For the geometry given in Figure 5-2 the resistance is

approximated by $R=(4l_{leg}\rho)/(wt_d)$. The resistivity of the doped region is defined as $\rho=(\mu_p qp)^{-1}$, where μ is a known function of the dopant density. The factor of 4 enters because the cantilever has two legs, each of width $w/2$ and length l_{leg}. The total Johnson noise power for a given geometry and doping is therefore

$$\overline{V_J^{\ 2}} = \frac{16k_B T l_{leg}}{wt_d \mu qp}\left(f_{\max} - f_{\min}\right). \quad (5.2)$$

Although the overall resistance sets the Johnson noise level, minimizing R is not usually a priority for the following reason: the sensitivity is proportional to the bias voltage, which is in turn limited by the power dissipation of the device ($V_B^{\ 2}/R=constant$), so $V_B=\sqrt{R\cdot constant}$. Since both the sensitivity and noise vary as $\sqrt{R}$, the Johnson noise due to high resistance can be compensated for by an increased bias voltage. The minimum value of R is in fact more of a concern, and should be high enough to exceed the voltage noise of the first stage of amplification. For the AD624 instrumentation amplifier, the voltage noise is 4 nV/√Hz, which is equivalent to the Johnson noise of a 1 kΩ resistor. The current noise of the AD624 is 200 fA/√Hz above 10 Hz, so in that frequency range the Johnson noise of the resistor will exceed the current noise up to a resistance of 400 kΩ.

5.3. 1/f noise

Hooge noise theory

In 1969, F. N. Hooge put forth the empirical observation that the *1/f* noise spectral density (units [V^2/Hz]) of a homogeneous resistor is dependent on the total number of carriers in the resistor, according to the equation:

$$S_H = \frac{\alpha V_B^{\ 2}}{Nf} \qquad (5.3)$$

where V_B is the bias voltage across a resistor with a total number of carriers N, and f is again frequency[2]. α is a dimensionless parameter which, for an implanted resistor, has since been found to vary depending on the anneal[3].

If equation (5.3) is integrated from f_{min} to f_{max}, then the voltage noise power is

$$\overline{V_H^{\ 2}} = \frac{\alpha V_B^2}{N} \ln\left(\frac{f_{\max}}{f_{\min}}\right). \qquad (5.4)$$

Note that for any decade of frequency, the integrated *1/f* noise is constant. The total noise between 1 Hz and 10 Hz is the same as that between 1 kHz and 10 kHz. Although the bandwidth is much greater in the latter case, the noise level is correspondingly less.

For a constant doping concentration, the number of carriers is proportional to the volume, so the *1/f* noise power density varies inversely with the cantilever volume. This is an unfortunate result for the prospects of further cantilever miniaturization. The Hooge noise is not dependent on the resistance since a long thin resistor with high resistance can have the same number of carriers as a short, wide, low resistance one.

Verification of the Hooge formula

We initially happened onto Hooge noise as the source of our *1/f* problems after a set of thin epitaxial cantilevers showed unusually high *1/f* noise characteristics. Four of these 0.1 µm-thick cantilevers were pictured in Figure 4-3. Plots of noise vs. frequency for these cantilevers are shown in Figure 5-3. This data set suggests that there is something systematic in the *1/f* noise of these piezoresistors, since the noise levels are ordered according to the size of the cantilevers. These noise levels are also higher than those reported for other thicker cantilevers from the literature, whose *1/f* noise corner is

typically in the low hundreds of hertz[4,5]. Some 1 μm-thick cantilevers from the same fabrication run as the cantilevers of Figure 5-3 had much lower *1/f* noise, so the epitaxial process itself could not account for the excess noise.

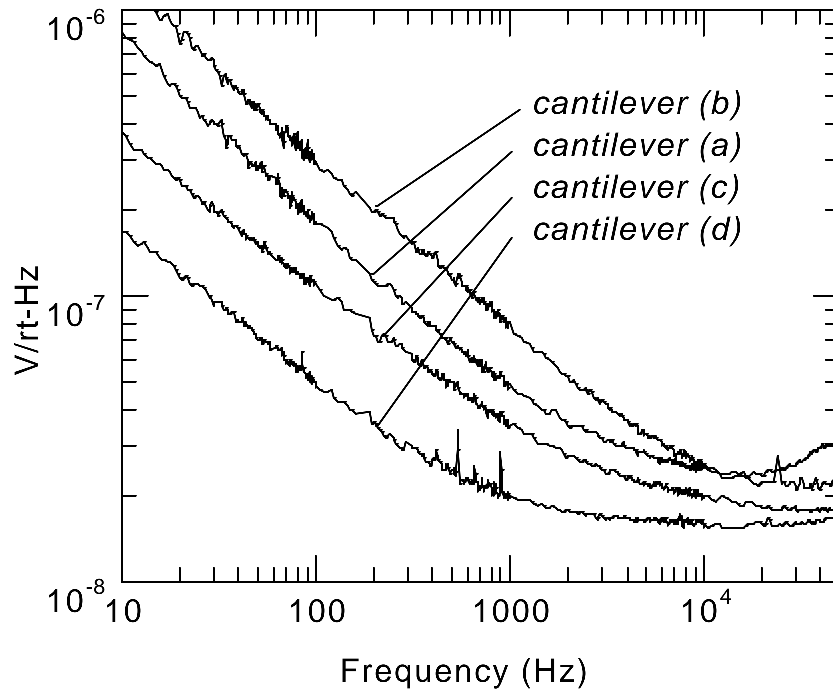

Figure 5-3. Noise spectra of the 100 nm-thick cantilevers shown in Figure 4-3. (a) 10 μm × 8 μm (b) 50 μm × 2 μm (c) 40 μm × 20 μm (d) 350 μm × 44 μm. The piezoresistive region is not the same percentage of the total cantilever volume in all cases.

Our initial explanation was that because the passivating oxide on the cantilevers had been removed (see section 4.3), surface noise effects were dominating. A set of cantilevers that had not been released or stripped of their oxide showed the same noise spectra, however, discounting that hypothesis. The ability to remove or omit the passivating oxide, in fact, has positive implications for thin piezoresistive cantilevers, since for such thin cantilevers even a thin oxide passivation contributes a substantial percentage thickness and results in undesirable bending from the compressive stress of the oxide.

To test the Hooge noise relation, the total number of carriers in each cantilever was calculated using a finite element analysis. The *1/f* noise for a variety of cantilevers is plotted as a function of the effective number of carriers, *N*, in Figure 5-4. The plot shows cantilevers of different lengths, widths and thicknesses, ranging from 970 Å to 2.2 μm thick. The square points are from this work, for 300 Å-thick $4{\cdot}10^{19}$ cm^{-3} boron doped epitaxially grown layers with lengths ranging from 10 μm to 350 μm and widths ranging from 4 μm to 40 μm. Figure 5-3 also includes points from thicker cantilevers previously published by other authors.

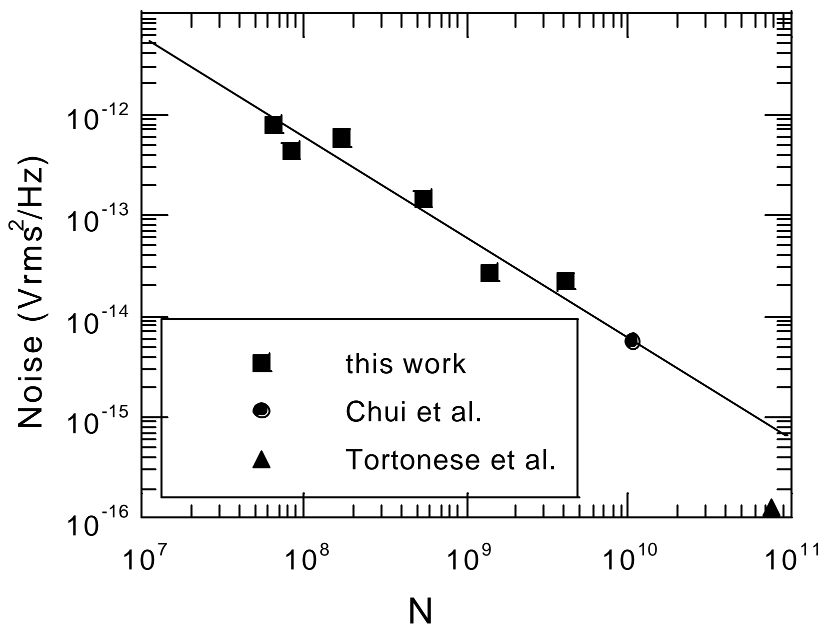

Figure 5-4. Measured 1/f noise power density at 10 Hz vs. number of carriers for piezoresistive cantilevers. A line of slope -1 indicates the Hooge model. The point from Tortonese et al. has a greater anneal than the others (see section 6.3).

This plot further contradicts the notion that surface quality is paramount in the *1/f* noise level of a resistor, since the data shows increasing noise as the surface area decreases. If the hypothesis were put forth that the surface to volume *ratio* were the important parameter, then cantilevers with constant thickness and doping should all have the same noise, because their surface to volume ratio, *(wl)/(wlt),* is constant. The square

points plotted in Figure 5-4 are from cantilevers of the same thickness and doping, indicating this is also not the case.

Computing the number of effective carriers

For a rectangular resistor with constant doping concentration, $N=pwlt$. For non-rectangular resistors, where the current density is not constant, the equivalent number of carriers is more difficult to compute and the simple formula of equation (5.3) cannot be directly applied.

Intuitively, carriers near the tip of the cantilever should not be included in the computation of N, since they are not involved in the conduction. This is indeed the case, and a more complicated formula must be used, which weights carriers by their contribution to the current density. This can be written as[6]:

$$S_H = \frac{\mathbf{a}}{I^2 f} \iiint (J \cdot J)^2 \frac{\mathbf{r}^2}{p} dxdydz \qquad (5.5)$$

where I is the total current and J is the current density. The integral is taken over the full volume of the cantilever.

To use this formula on a non-trivial geometry requires knowledge of the current density, which usually entails a finite element solution, such as that shown in Figure 5-5. Note that highest current density is at the corner where the current changes direction. Since the current density contributes noise power to the fourth power it is therefore advisable to minimize sharp corners in the current path wherever possible.

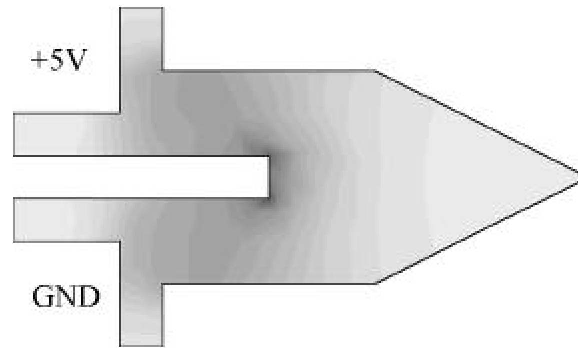

Figure 5-5. Finite element solution of current density in a cantilever. The current travels out the top leg, and returns on the bottom leg, with the highest current density near the corner where it changes direction.

For back-of-the-envelope calculations, one can define a square of resistance as the leg width squared, and compute the number of carriers in one square. Knowing the total number of squares from a measured value of resistance then gives a close approximation of N.

Sharp corners pose a difficulty for counting squares without real devices to measure. Table 5-1 shows four simulated geometries, and the number of squares of resistance associated with each. This should be a sufficient tool to adequately approximate most structures for design purposes. Some of the shapes in the table can be constructed from sub-shapes, which gives an idea of the errors involved in building from simple cases. Although the equivalent number of squares resistance can be obtained from Schwarz-Christoffel conformal mapping[7], these values were obtained with a finite element model.

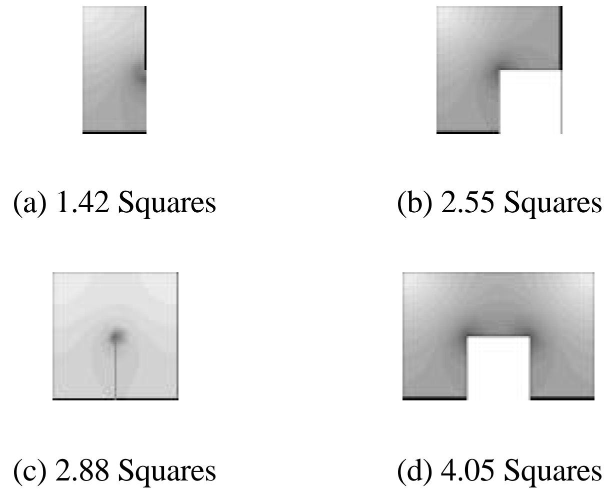

Table 5-1. Building blocks for computing the number of squares resistance. The bold lines at the ends of the structures indicate lines of constant potential where the bias voltages are applied.

In many cases, however, approximating the number of carriers as the density times the doped volume of the legs ($N=l_{leg}t_d w$) is adequate. Then, as for Johnson noise, the Hooge noise can be predicted based on only the doping and geometry as

$$\overline{V_H{}^2} = \frac{\alpha V_B^2}{l_{leg} t_d w p} \ln\left(\frac{f_{\max}}{f_{\min}}\right). \tag{5.6}$$

5.4. Thermomechanical noise

Another possible noise source for consideration in piezoresistive cantilevers is the thermomechanical noise[8]. This is the mechanical analog of Johnson noise, and consists of physical oscillations due to thermal energy in the beam. Thermomechanical noise has yet to be a limiting factor for the low frequency noise of any piezoresistive cantilever, but has been observed for high-Q cantilevers on resonance[9] and could particularly be a factor in resonant sensors where the noise spectrum near the resonance is of consequence. The cantilevers reported in this work are the closest to DC thermomechanical noise of any

thus far reported. The Johnson noise of the softest cantilever comes within a factor of 5 of the low frequency thermomechanical noise.

Thermomechanical noise is effectively a white noise drive [N^2/Hz] of force power density

$$S_{F,th} = \frac{4kk_B T}{\omega_0 Q}. \tag{5.7}$$

This drive signal passes through the transfer function of the cantilever. If the damping is independent of frequency, the fundamental mode can be well represented as a second order oscillator as

$$H(\omega) = \frac{1/m^2}{\left(\omega_0{}^2 - \omega^2\right)^2 + \left(\omega_0 \omega / Q\right)^2}, \tag{5.8}$$

so the resulting displacement noise spectral density [m^2/Hz] is

$$S_{th}(\omega) = \frac{4\omega_0 k_B T}{mQ} \frac{1}{\left(\omega_0{}^2 - \omega^2\right)^2 + \left(\omega_0 \omega / Q\right)^2}. \tag{5.9}$$

At low frequencies the displacement noise is independent of frequency, which, rewritten to include the spring constant, k, is

$$S_{th} = \frac{4k_B T}{k\omega_0 Q}. \tag{5.10}$$

At resonance the amplitude is increased by a factor Q, with a width of f_0/Q at the –3dB points. Above the resonance the noise rolls off at –40 dB/decade, although there will be higher order modes present which are not included in this model. The amplitude [m] of the noise oscillations as a function of frequency is shown in Figure 5-6.

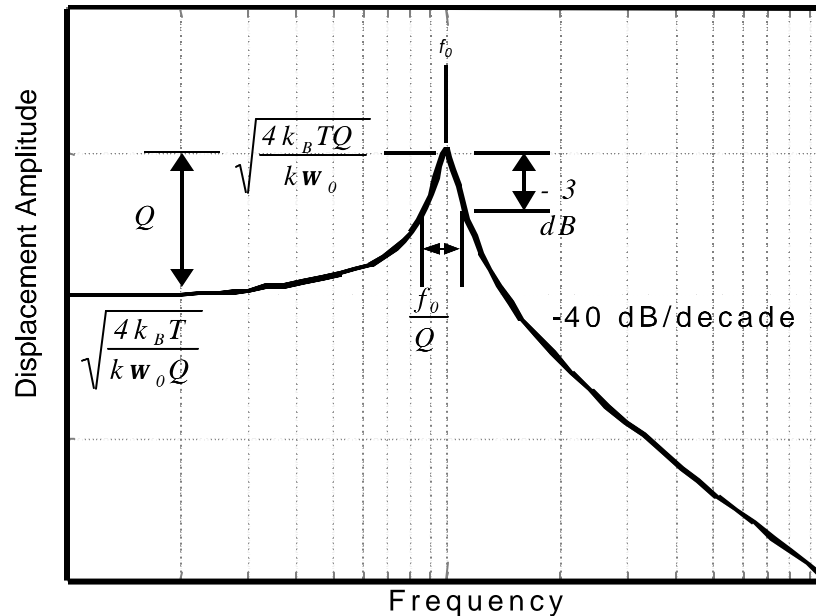

Figure 5-6. Displacement as a function of frequency for the thermomechanical noise of an oscillator, illustrating two methods to measure Q from such a diagram.

Note that in Figure 5-6 the definition of f_0/Q as the width at the –3 dB point is not the full width half maximum of the curve. The definition of f_0/Q as the width at half maximum is true only on a power plot [m^2], and not on a plot of amplitude [m]. In either case, Q is defined with reference to the –3 dB point, but on a power plot there are only 10 dB per decade, so the half maximum is –3 dB. In an amplitude plot there are 20 dB per decade, so the –3 dB point is where the amplitude has dropped by $1/\sqrt{2}$. This definition of Q can be verified by showing that the amplitude of $H(\omega)$ at $f=f_0+f_0/2Q$ (from equation (5.8)) is very close to half of $H(\omega)$ at $f=f_0$.

5.5. Summary

The three major noise sources for piezoresistive cantilevers were identified: Johnson noise, *1/f* noise and thermomechanical noise, and equations for each in terms of beam

dimensions and electrical characteristics are provided. *1/f* noise was shown experimentally to follow the Hooge relation for piezoresistors. These noise sources will provide a basis for a complete piezoresistor optimization in the following chapter.

References

1. H. Nyquist, "Thermal Agitation of Electric Charge in Conductors," *Phys. Rev.*, vol. 32, pp. 110-113, 1928.
2. F. N. Hooge, "1/f noise is no surface effect," *Phys. Lett. A*, vol. 29, pp. 139-140, 1969.
3. L. K. J. Vandamme and S. Oosterhoff, "Annealing of ion-implanted resistors reduces the 1/f noise," *J. Appl. Phys.*, vol. 59, no. 9, pp. 3169-3174, 1986.
4. M. Tortonese, H. Yamada, R. C. Barrett, and C. F. Quate, "Atomic force microscopy using a piezoresistive cantilever," *Transducers 97. 1997 International Conference on Solid-State Sensors and Actuators*, pp. 448-451, 1991.
5. B. W. Chui, T. D. Stowe, T. W. Kenny, H. J. Mamin, B. D. Terris, and D. Rugar, "Low-stiffness silicon cantilevers for thermal writing and piezoresistive readback with the atomic force microscope," *Appl. Phys. Lett.*, vol. 69, no. 18, pp. 2767-2769, 1996.
6. L. K. J. Vandamme and W. M. G. van Bokhoven, "Conductance noise investigations with four arbitrarily shaped and placed electrodes," *Appl. Phys.*, vol. 14, no. 2, pp. 205-215, 1977.
7. Warner, R. M. Jr. and Fordemwalt, J. N., *Integrated Circuits,* McGraw-Hill, New York, 1965.
8. T. B. Gabrielson, "Mechanical-thermal noise in micromachined acoustic and vibration sensors," *IEEE Trans Electron Devices*, vol. 40, no. 5, pp. 903-909, 1993.
9. Ried, R. P., Mamin, H. J., Terris, B. D., Fan, L. S., and Rugar, D., "5 MHz, 2 N/m piezoresistive cantilevers with INCISIVE tips," pp. 447-450, 1997.

Chapter 6. Optimization of piezoresistor design and processing

With the addition of the Hooge noise relation of equation (5.3) to the sensitivity and Johnson noise equations, the impact of geometry and doping on the major noise sources and the sensitivity is now known. The analysis of Chapter 2 can now be extended to a full optimization of cantilever resolution.

The pattern of the optimization trade-off is repeated several times. Improvements designed to help the noise by increasing the number of carriers or lowering the Hooge constant, $\boldsymbol{a}$, hurt the sensitivity, either by lowering the $\boldsymbol{b}$ of equation (3.24) or reducing the piezoresistive coefficient $\boldsymbol{p}_l$.

The electrical processing of the cantilever has no effect on the thermomechanical noise, which is specified entirely by the spring constant, resonance frequency and resonance quality. The particular choices of length width and thickness once k and $\boldsymbol{w}_0$ are specified have no bearing on the thermomechanical noise, except perhaps in the Q of the oscillator. For these reasons, and considering that no piezoresistive cantilever has ever been limited by low-frequency thermomechanical noise, the optimization which follows concerns only Johnson and $1/f$ noise.

6.1. Geometrical design optimization

Thickness

As established in Chapter 2, for high sensitivity and bandwidth cantilevers should be made as thin as possible. Thinner cantilevers have increased bending stress from applied forces, and the lower mass permits higher bandwidth for a given spring constant. As was

shown in the previous chapter, however, *1/f* noise is worse for smaller cantilevers. It will be demonstrated in this chapter that the low frequency resolution is worse for a thin cantilever, despite the increased sensitivity. The cantilever should therefore be made as thin as necessary to satisfy the spring constant and bandwidth requirements, but no thinner, if it is to be used as a low frequency transducer. For cantilevers that will measure resonant shifts, or are otherwise primarily concerned with higher frequency signals, the device should be made as thin as possible.

Width

From equation (3.17), it is evident that reducing width can improve force sensitivity as w^{-1}. In this case it reduces the spring constant, but not the resonant frequency. According to equations (5.2) and (5.6), the voltage noise from both Johnson and Hooge sources varies as $w^{-1/2}$ so the resolution varies as $w^{1/2}$. From this perspective, cantilevers for force resolution should be as narrow as the lithography limitations allow.

However, if the width is to be reduced without changing the spring constant (i.e. reduce the length at the same time), the force sensitivity only improves as $w^{-1/3}$, and both the *1/f* and Johnson noise gets worse according $w^{-2/3}$. In this case, the force resolution for a fixed spring constant actually improves for wider cantilevers, but varying only as $w^{-1/6}$. With the spring constant fixed, the displacement resolution in this case also varies as $w^{-1/6}$, again slightly favoring wider cantilevers. This variation is so slight, however, that any convenient width value will do, and much concern need not be given to the matter.

Leg length

Once the thickness, spring constant and width are chosen, the length of the cantilever is fully determined. The ratio of the leg length, l_{leg}, to the total length l still remains to be chosen, however. If the legs extend the full length of the cantilever, the number of carriers is maximized, to the benefit of the Hooge noise, but there is a loss in sensitivity

due to the extra resistance near the tip of the beam where the stresses are low. Conversely, if the legs had nearly zero length, the piezoresistive region would always see the maximum possible stress, but the resistor would have increased Hooge noise due to a lack of carriers. By writing a full expression for the displacement resolution, the optimum leg length can be computed.

If the piezoresistor makes up one corner of a Wheatstone bridge, the output signal is

$$V_{out} = \frac{V_B}{4}\frac{\Delta R}{R}, \tag{6.1}$$

and an expression for the displacement resolution which includes both noise sources and the force sensitivity can be written:

$$x_{\min} = \frac{\sqrt{\frac{\mathbf{a} V_B^2}{l_{leg} t_d w p}\ln\left(\frac{f_{\max}}{f_{\min}}\right) + \frac{16 k_B T l_{leg}}{w t_d \mathbf{m} q p}\left(f_{\max} - f_{\min}\right)}}{\frac{3 V_B \mathbf{p}_L E t}{8 l^3}\left(\frac{l - l_{leg}}{2}\right)}. \tag{6.2}$$

In this case the first term in the numerator is the contribution of Hooge noise, and the second is the contribution of Johnson noise. The denominator is an expression of the sensitivity.

If l_{leg} in equation (6.2) is replaced by $a{\times}l$, where a is the fraction of the total length that the legs extend, then the resolution can be written as a function of a. Differentiating $x_{\min}$ with respect to a then gives an optimal ratio of the leg extension.

The calculated displacement resolution for a typical cantilever[1] is shown in Figure 6-1, along with the resolution limited by Johnson and Hooge noise independently. The *1/f* limited resolution always has a minimum at a=2/3, and the Johnson limited resolution increases monotonically, so there is no reason to extend the legs beyond two thirds of the cantilever length. For leg length less than one third the total length, the *1/f* noise

increases dramatically, unless the cantilever is dominated by Johnson noise. For the rest of this work *a=0.5* will be used as an optimal value for the general case.

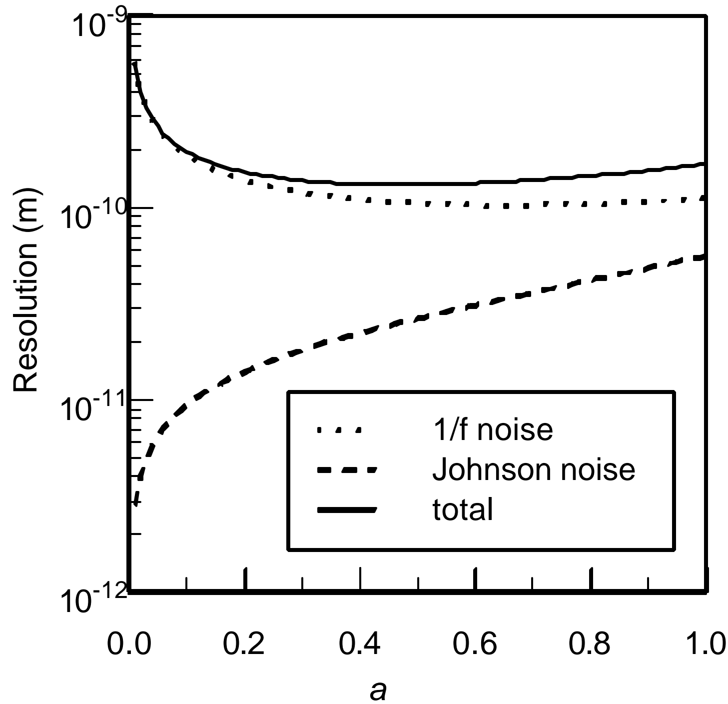

Figure 6-1. Plot of noise vs. leg length ratio *a* for standard cantilever[1] in a bandwidth from 10 Hz to 1 kHz. The dotted curve indicates the *1/f* noise, and the dashed curve is the Johnson noise. Thermomechanical noise with a Q of 50 would add a horizontal line to this graph at 4×10^{-13} m, and is therefore a negligible source of noise.

At this point, the cantilever geometry has been optimized, but there remain several important processing decisions that will affect the performance. The appropriate doping level must be chosen, as well as the thickness of the doped layer. Following that, surface treatments and an appropriate anneal must be chosen to minimize the noise without unduly reducing sensitivity.

6.2. Dopant concentration

There are two major decisions to be made regarding the dopant: 1) how deep should it extend into the cantilever, and 2) what is the appropriate concentration. Both decisions involve a trade-off between sensitivity and noise. The depth and concentration are independent for the optimization, so they can be treated separately.

Dopant depth

The optimum depth of the doped layer involves a trade-off of reducing the noise at the expense of reduced sensitivity. If the doped layer is very shallow, the number of carriers is small and the *1/f* noise is high, but if the doped layer is very deep, $\boldsymbol{b}$ (see section 3.5) tends to zero, and sensitivity is lost.

Epitaxially grown layers can achieve near step profiles, and implanted layers can be approximated with an equivalent step profile. The assumption of a step profile simplifies the integral formula of equation (3.24) to $\boldsymbol{b} = 1\text{-}t_d/t$, where t_d is the thickness of the dopant. After substituting this simplified equation for $\boldsymbol{b}$ into the total resolution equation (6.2), the derivative can be computed with respect to t_d to solve for the minimum resolution. The resulting minimum occurs at $t_d = t/3$, and is independent of the doping level and the geometry, including thickness. For doping depth between 15% and 60% of the thickness the resolution is within 20% of the optimum, beyond which point it rolls off sharply, as shown in Figure 6-2. For all piezoresistive cantilevers, then, the target thickness for the doped layer should be approximately one third of the total thickness, but there is some room for error.

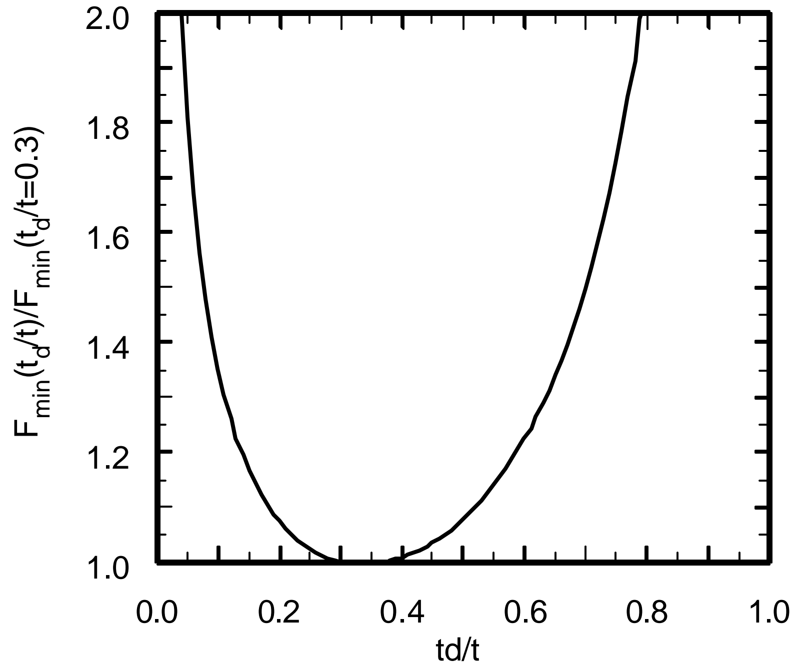

Figure 6-2. Force resolution as a function of doping depth. The optimum resolution is obtained for a doping thickness of *t/3*. Dopant depths from 0.15*t* to 0.6*t* give resolution within 20% of the minimum.

Concentration

Early studies of the piezoresistive effect showed that as the doping concentration increased, the piezoresistive coefficient, p_l, decreased[2]. This has a direct impact on the sensitivity from equations (3.17) and (3.18), and so although a higher concentration has more carriers for reduced noise, again it is not without cost.

A majority of recent calculations for the relation between p_l and the doping concentration have used a theoretical model proposed by Kanda[3] for the relation between p_l and the doping concentration. This model is reasonably accurate at low concentrations, but it substantially underestimates p_l at higher doping concentrations. At low concentrations (~5×10^{14} cm^{-3}) Smith found the p-type longitudinal piezoresistive coefficient in the [110] direction for silicon to be relatively constant at 72×10^{-11} m^2/N.[4] Since the piezoresistive coefficient decreases at higher concentrations (above 10^{17} cm^{-3}),

a piezoresistive factor *P(p)*, dependant on the doping concentration, was defined by Kanda to express the coefficient as a fraction of the maximum, low concentration, value. Room temperature data from Mason *et al.*[2], from Tufte and Stelzer[5], and one point from Kerr and Milnes[6], is shown in Figure 6-3 along with the theoretical curve from Kanda.

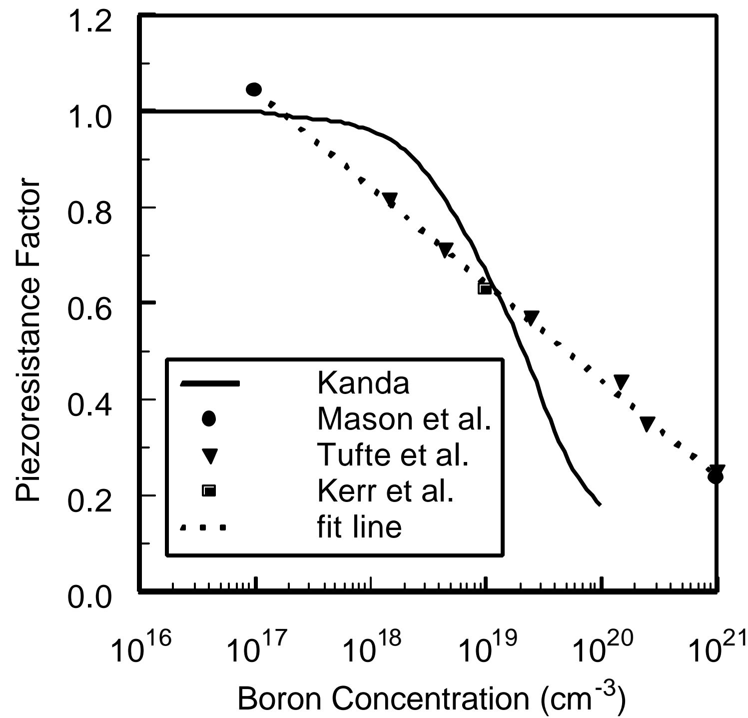

Figure 6-3. The longitudinal piezoresistive coefficient as a function of boron concentration. A widely used theoretical model by Kanda is shown as the solid line. This model substantially underestimates the piezoresistive coefficient at high concentrations.

For concentrations in the range of interest (above 10^{17} cm^{-3}), this data is well approximated by a straight line on the semi-log plot, according to

$$P(p) = \log\left(\frac{b}{p}\right)^{a}, \tag{6.3}$$

with a = 0.2014 and b=1.53 · 10^{-23} cm^{-3}.

The trade-off is by now a familiar one. At high dopant concentrations there are many carriers, and therefore improved Hooge noise. At low concentrations the sensitivity is highest, which gives the best resolution for a device limited by Johnson noise. There is a further limitation, however, because high dopant concentrations result in lower resistance. The sensitivity varies proportionally to the bias voltage (equation (6.1)), while the power varies as V_B^2/R so for a fixed power consumption, a heavily doped cantilever will a lower bias voltage and therefore reduced sensitivity. This is a second sensitivity loss associated with higher doping.

For the 1000 Å thick cantilevers in vacuum, we have found that power consumption in excess of 2-3 mW can result in destruction of the beams. Thicker cantilevers should be able to dissipate more power, but conservatively assuming a maximum power of 2.5 mW, the optimum doping level can be computed. Figure 8 shows the Hooge and Johnson limited force resolution as a function of dopant concentration for the standard cantilever in a bandwidth from 10 Hz to 1 kHz with a power consumption limited to 2.5 mW. The best force resolution in this case occurs for a doping of 10^{20} cm^{-3}, substantially higher than the 10^{17}-10^{18} cm^{-3} typically used.

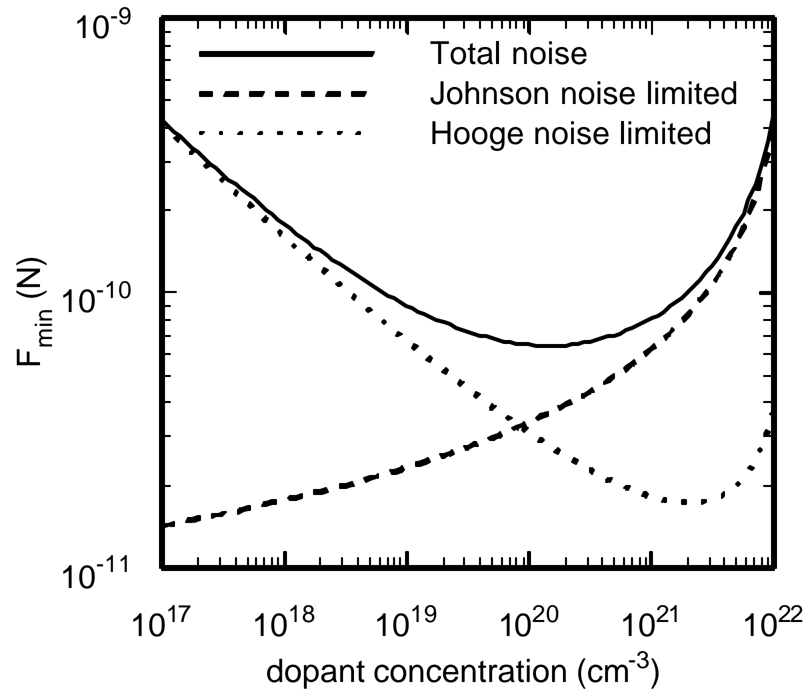

Figure 6-4. Minimum detectable force vs. doping concentration for standard cantilever[1] assuming a maximum power dissipation of 2.5 mW.

Again, the bandwidth of interest is important. A low-frequency cantilever that is dominated by *1/f* noise will favor heavy doping, while a cantilever used for measurements in a Johnson noise-limited frequency regime will favor low doping. The plot in Figure 9 shows the optimum doping level as a function of the piezoresistor volume and intended bandwidth for α=10^{-6} and P=2.5 mW. To find the optimum doping compute the abscissa, $(f_{max}$-$f_{min}/log(f_{max}/f_{min}))$, for the intended bandwidth and read the doping level from the curve corresponding to the cantilever volume ($l_{leg}t_d w$). This chart should also be valid for piezoresistors of other geometries. The dependence on volume arises because a large cantilever will naturally have more carriers, and can therefore use a lower doping level to increase sensitivity.

High doping levels also have the added advantage of reduced sensitivity to temperature fluctuations. Tufte and Stelzer show convincing graphical evidence that as

the doping concentration rises, particularly above 10^{20} cm^{-3}, the piezoresistive coefficient becomes almost independent of temperature variations between -80°C and 100°C.

A final consideration for the doping and depth combination is the total resistance, and whether other noise sources may eventually dominate. A good differential amplifier has noise approximately equivalent to the Johnson noise of a 1 kΩ resistor, so1 kΩ is a reasonable value for the minimum acceptable resistance.

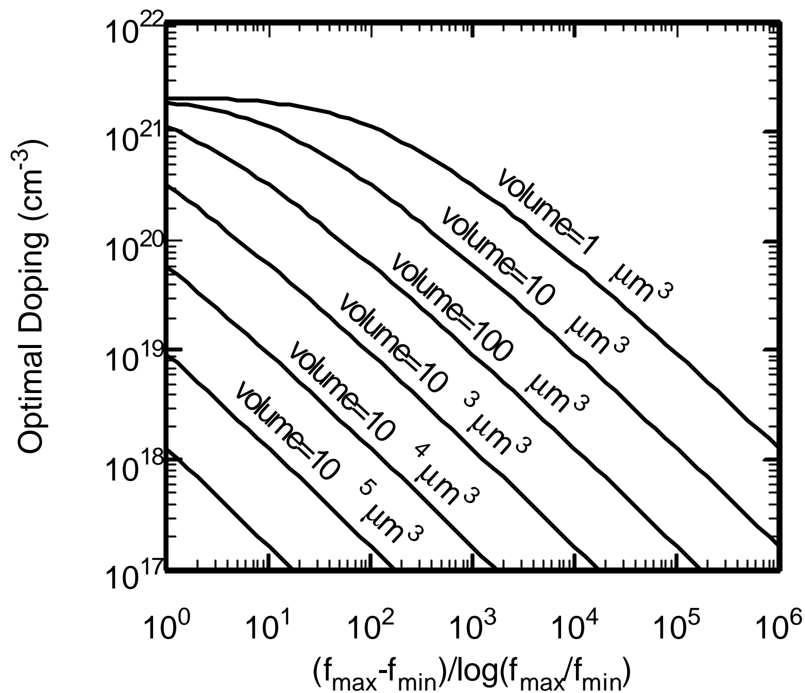

Figure 6-5. Optimal doping depending on cantilever size and operation bandwidth. A value of 10^{-6} is assumed for α and the power dissipated is 2.5 mW. Compute the value of $(f_{max}-f_{min})/\log(f_{max}/f_{min})$ and read the optimal doping off the y-axis for the given volume of the doped conducting region of the cantilever ($l_{leg}wt$). For other power dissipation values, the doping concentration for a 10-fold increase in power consumption is read from the curve of a 10-fold larger cantilever.

6.3. Surface treatment and anneal

The last important processing decision is the annealing of the dopant, and the potential addition of passivating surface layers. All of the piezoresistive cantilevers discussed in the work have a passivating oxide layer on the surface of the device, presumably to limit the *1/f* noise due to charge trapping or surface charges (viz. the McWhorter model of *1/f* noise[7]).

We have found in our batch of 1000 Å thick piezoresistive cantilevers that the removal of a 200 Å surface oxide had a negligible effect on the *1/f* noise. Gerlach *et al.* found that that "internal disturbances" were reduced with thicker oxides, particularly those grown at higher temperatures, but that secondary coatings such as nitride layers did not improve the noise[8]. While surface noise sources may still be present, and perhaps even dominant in large cantilevers with low Hooge noise, our data supports the claim that there is a bulk *1/f* noise source that eventually limits the cantilevers.

In their study of the *1/f* noise in implanted resistors, Vandamme *et al.* found that annealing could reduce the α parameter of equation (5.3) by up to three orders of magnitude[9]. They postulate that the anneal improves the quality of the crystal lattice, thereby reducing fluctuations in carrier mobility. It is not unreasonable to assume that it is the total anneal, measured in terms of the diffusion length $\sqrt{D\tau}$, rather than just the temperature, which determines the lattice quality (the τ in $D\tau$ is time, to distinguish it from the thickness, t). The diffusion coefficient is defined as $D=D_{io}exp(-E_{ia}/k_B T)$, where for boron D_{io}=0.037 cm^2/sec and E_{ia}=3.46 eV[10]. A plot of data available in the literature is shown in Figure 6-6.

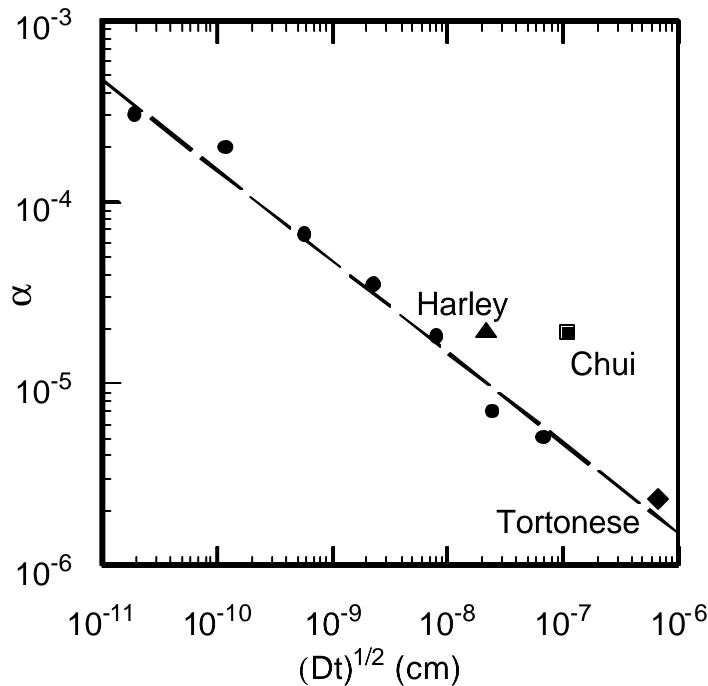

Figure 6-6. Hooge noise parameter ***a*** as a function of anneal diffusion length $\sqrt{Dt}$. The round points are data from Vandamme *et al.*, taken on implanted samples annealed for 4 hours at temperatures ranging from 450°C to 900°C [23]; the cantilever from Tortonese *et al.* was annealed 10 minutes each at 900°C and 1000°C[7]; the cantilever from Chui *et al.* was annealed 10 seconds at 1000° C and 40 minutes at 800°C[14]; the cantilever from this work was epitaxially grown silicon annealed 3 hours at 700°C[11]. The oxide grown to passivate the epitaxial cantilevers was later removed with pad etch. The other cantilevers remain passivated.

This data is not conclusive, but it does suggest that measured *1/f* levels can be related to the anneal. Since a thermal oxide growth is also an anneal, the importance of surface oxides may actually lie in the improvement of crystal lattice for Hooge noise rather than surface passivation. The data point from Tortonese *et al.* in Figure 5-4 which was an order of magnitude below the fit line of the rest of the data can now be accounted for by Figure 10, where the ***a*** parameter for that work is an order of magnitude better than that of Chui *et al.* and Harley *et al.*

The fit line of Figure 10 is given by $a = 1.5\times10^{-9}\sqrt{\text{cm}}/(Dt)^{1/4}$. An α value of 10^{-6} is the lowest we are aware of, and the indicated trend line is not likely to continue

indefinitely. Anneals with $\sqrt{Dt}$ above 10^{-6} cm are therefore perhaps unnecessary. The point from this work is for epitaxially grown silicon, and isn't expected to have the same lattice damage as an implanted sample. These caveats aside, if the indicated line is correct, the result has some interesting implications for optimization.

Much like the argument for the depth of the doped layer, the trade-off here is again between lower *1/f* noise and worsening of $\boldsymbol{b}$. Longer anneals cause the dopant to diffuse through the beam, resulting in a distribution further from the maximum stress at the surface.

Following an implant, the dopant concentration is well approximated by a Gaussian distribution. This distribution spreads as a Gaussian during an anneal, according to

$$p(z,t) = \frac{Q_T}{\sqrt{\boldsymbol{p}Dt}} e^{\frac{-z^2}{4Dt}} \quad (6.4)$$

where the total dopant density is Q_T [cm^{-2}], Dt is the diffusion length and z is the depth into the surface. It is assumed that the initial implant was done through a surface layer such that $z=0$ occurs at the top of the silicon.

This formula for the concentration can be substituted into equation (3.24) for $\boldsymbol{b}$. It is assumed that the implant energy has been selected such that the doping concentration at $z=t/3$ is a factor of 10 less than the concentration at the surface. This gives $\boldsymbol{b}=0.7$, which has previously been determined to be optimal. The equation for $\boldsymbol{b}$ can then be plotted as a function of Dt. These results are shown in Figure 6-7 for an initial peak concentration of $1.5 \cdot 10^{20}$ cm^{-3} for cantilevers of various thicknesses.

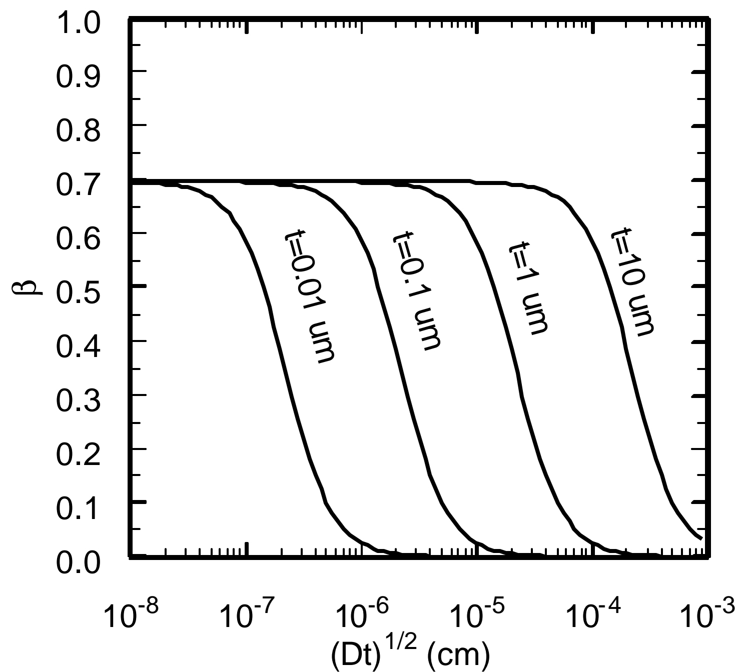

Figure 6-7. Plot of sensitivity factor β vs. anneal for cantilevers of various thickness. Above the corner anneal for each line, the net resolution worsens, providing an optimum anneal level for a given cantilever thickness.

The most important feature of Figure 6-7 is that up to some reasonably well defined point the anneal causes negligible dopant diffusion, after which it rolls off. Since the Hooge noise is decreasing with additional annealing, the force resolution improves as long as ***b*** is unaffected. Beyond the corner where ***b*** drops off, there is a net loss of force resolution, even for a fully Hooge noise-limited cantilever. The optimal anneal strategy is therefore to anneal just to the corner of the appropriate curve in Figure 6-7. For a 0.1 µm cantilever, $\sqrt{Dt}$ ~10^{-6} cm, so any piezoresistive cantilever thicker than 0.1 µm should receive at least that anneal, which is 22 minutes at 1000°C. In general, for anneals which are within the range plotted in Figure 6-6, the optimal anneal as a function of thickness is calculated to be $Dt=0.025t^2$, if t is the thickness in meters, and Dt is the anneal meters squared. Note that this analysis does not include transient enhanced diffusion which can substantially increase the dopant diffusion for implanted samples[11].

6.4. Operation

Now that an optimized device has been designed, only the question of optimal bias voltage remains. The sensitivity improves linearly with the bias voltage, according to equation (6.4), so at first glance a high bias voltage appears desirable. For *1/f* noise limited sensing, the noise power varies as V_B^2, so the noise voltage varies as V_B and there should be no preference for a particular bias voltage. The Johnson noise is independent of bias voltage, however, so in this case the higher bias is preferable. With one case preferring high bias, and the other ambivalent, the cantilever should be biased as high as its power dissipation abilities can tolerate. This is typically on the order of a few milliwatts, corresponding to a bias voltage of 5-10 V for most cantilevers. In addition to the potential physical destruction of the cantilever[12], a high operating temperature can hurt the resolution performance[13].

6.5. Predicted resolution

Incorporating all the optimization decisions made so far, we can now estimate the achievable force resolution for piezoresistive cantilevers. Assume the leg lengths extend half the total length, that the width is 10 µm, and that a doped region of 10^{19} cm^{-3} extends one third of the cantilever thickness, giving a β of 0.7. The optimal anneal is then selected as a function of thickness as described previously. For a given thickness spring constant and assuming a width of 10 µm, the length can be determined from equation (3.1).

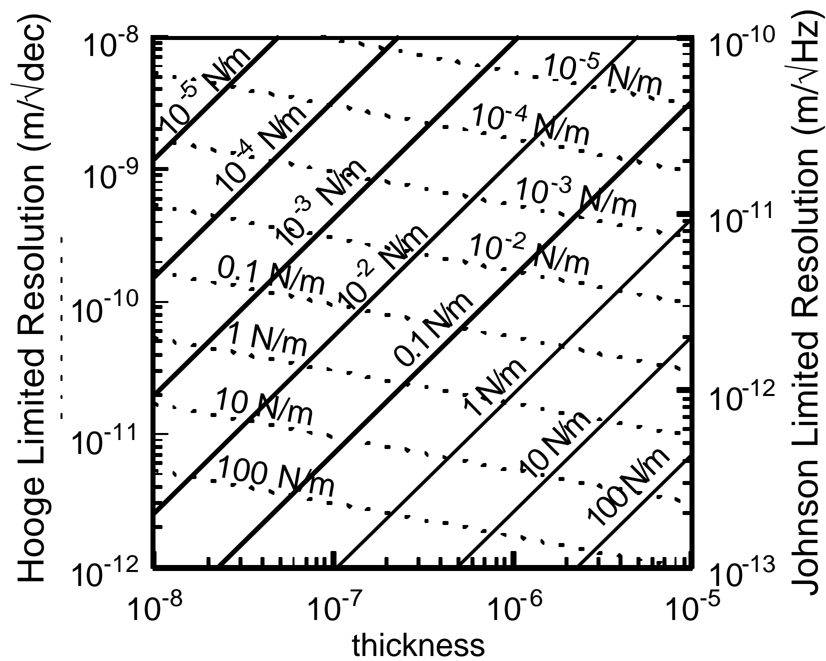

Figure 6-8. Displacement resolution, as limited by *1/f* noise and by Johnson noise for 10 μm wide cantilevers. The contours are for constant stiffness, with the spring constant written above the contour. The dotted lines give the *1/f* limited resolution, and the solid lines give the Johnson limited resolution.

The graph in Figure 6-8 illustrates the displacement resolution vs. thickness for cantilevers of given spring constants. The dashed lines of constant spring constant correspond to the left axis, and indicate the Hooge limited resolution. The solid lines correspond to the Johnson limited resolution, and are to be read off the right axis. The Hooge limited resolution is given per root-decade of bandwidth since the integrated noise per decade is constant. The Johnson noise is flat vs. frequency, and is therefore given as m/$\sqrt{Hz}$. Note that once a cantilever is fully limited by *1/f* noise, reduced thickness worsens the resolution, although it may still be advantageous due to bandwidth gains.

6.6. Example of cantilever design

As an example, consider the design of a 0.01 N/m 100 kHz cantilever intended to operate in a bandwidth from 10 Hz up to half its resonance, 50 kHz. From Figure 3-3, a maximum thickness of 0.2 µm is required. A width of 10 µm is convenient, and from equation (3.1) the length is set to 70 µm. The legs should extend half the total length and the doping 1/3rd the cantilever thickness. For the bandwidth calculations f_{min}=10 Hz and f_{max}=50 kHz, so the bandwidth figure for Figure 6-5 is 49990/3.7=13500. The cantilever volume is 134 µm^3, so from Figure 6-5 the optimal doping will be $4 \cdot 10^{18}$ cm^{-3}. From Figure 6-7 the anneal should be ~$2 \cdot 10^{-6}$ cm.

To calculate the expected displacement resolution this cantilever in a bandwidth from 10 Hz to 50 kHz, use Figure 6-8 to compute sqrt((($3 \cdot 10^{-10}$ m/$\sqrt{\text{decade}}$)$^2 \times$ (3.7 decades)) + (($4 \cdot 10^{-12}$ m/√Hz)$^2 \times$ (49990 Hz))) to get 1 nm displacement resolution in this bandwidth. Since we have chosen a spring constant of 0.01 N/m, the force resolution is 10 pN.

The resonant frequency of this cantilever is determined to be 100 kHz from Figure 3-3.

6.7. Summary

Piezoresistive cantilevers have been analyzed and optimized including expressions for both the *1/f* and the Johnson noise, as well as the cantilever sensitivity. These equations provide a complete expression for cantilever resolution. Using this expression, an optimization analysis has been performed, with the following conclusions:

Design

- The maximum cantilever thickness and the cantilever length will be set by spring constant and bandwidth requirements. For a fixed spring constant the force resolution varies as $w^{1/6}$ and the resonance varies as $w^{-2/3}$, so narrower is preferable, although the effect on resolution is small.
- For piezoresistors limited by Johnson noise, improved resolution can be achieved by reducing the cantilever thickness until, due to processing limitations, $\boldsymbol{b}$~0.7 can no longer be achieved. For cantilevers limited by *1/f* noise, thicker beams have improved resolution but lower bandwidth.
- The cantilever legs should extend between 30% to 70% of the total length, with shorter legs for Johnson limited devices, and longer ones for *1/f* noise limited cantilevers.

Processing

- The reduction of the piezoresistive coefficient with increased doping is not as severe as is often assumed, and can be expressed according to equation (6.3).
- The optimal thickness of the doped layer is one third of the total thickness with a 20% loss in resolution for dopant depths of 0.2t and 0.6t.
- For maximum resolution cantilevers should be doped as a function of their bandwidth and volume according Figure 6-5.
- For cantilevers limited by *1/f* noise the optimal anneal is related to the thickness t according to $D\tau=0.025t^2$, where $\boldsymbol{Dt}$ is in meters squared and t is in meters. Most cantilevers should use an anneal of ~$2{\cdot}10^{-6}$ cm, the maximum for which there is experimental Hooge noise data.

Operation

- The cantilever should be operated at as high a bias voltage as its power dissipation can tolerate.

References

1. Standard cantilever, l=100 μm, w=10 μm, t=1 μm,a=0.5, t_d=t/3, p=10^{19} cm^{-3}, f_{min}=10 Hz, f_{max}=1 kHz, 1999
2. Mason, W. P., Forst, J. J., and Tornillo, L. M., "Recent developments in semiconductor strain transducers," *Semiconductor and Conventional Strain Gages*, pp. 110-120, New York, 1962.
3. Y. Kanda, "Piezoresistance effect of silicon," *Sensors and Actuators A (Physical)*, vol. 28, pp. 83-91, 1991.
4. C. S. Smith, "Piezoresistance effect in germanium and silicon," *Phys. Rev.*, vol. 94, no. 1, pp. 42-49, 1954.
5. O. N. Tufte and E. L. Stelzer, "Piezoresistive Properties of Silicon Diffused Layers," *J. Appl. Phys.*, vol. 34, no. 2, pp. 313-318, 1963.
6. D. R. Kerr and A. G. Milnes, "Piezoresistance of diffused layers in cubic semiconductors," *J. Appl. Phys.*, vol. 34, no. 4, pp. 727-731, 1963.
7. McWhorter, A. L., *Semiconductor Surface Physics,* University of Pennsylvania Press, Philadelphia, 1957.
8. Gerlach, G., Nakladal, A., Buchhold, R., and Baumann, K., "The piezoresistive effect - stable enough for high-accuracy sensor applications?," *SPIE Conference on Micromachined Devices and Components IV*, vol. 3514, pp. 377-385, Santa Clara, CA, 1998.
9. L. K. J. Vandamme and S. Oosterhoff, "Annealing of ion-implanted resistors reduces the 1/f noise," *J. Appl. Phys.*, vol. 59, no. 9, pp. 3169-3174, 1986.

10. Runyan, W. R. and Bean, K. E., *Semiconductor Integrated Circuit Processing Technology,* Addison-Wesley, Reading, MA, 1990.

11. M. Miyake and S. Aoyama, "Transient enhanced diffusion of ion-implanted boron in Si during rapid thermal annealing," *J. Appl. Phys.*, vol. 63, no. 5, pp. 1754-1757, 1988.

12. B. W. Chui, M. Asheghi, Y. S. Ju, K. E. Goodson, H. J. Mamin, and T. W. Kenny, "Intrinsic-carrier thermal runaway in silicon microcantilevers," *Microscale Thermophys. Eng.*, vol. 3, no. 3, 1999.

13. O. Hansen and A. Boisen, "Noise in piezoresistive atomic force microscopy," *Nanotechnology*, vol. 10, pp. 51-60, 1999.

Chapter 7. A novel axial resonant probe

Up to this point, AFM probes have been evaluated primarily with regards to their force or displacement resolution and bandwidth. Force resolution was improved by making softer cantilevers, and bandwidth was improved by making smaller devices. This approach works for both piezoresistive and optically detected cantilevers. As softer cantilevers are used to achieve high force resolution, however, the force instabilities discussed in section 2.2 become a major concern. Cantilevers are unable to measure forces if the slope of an attractive force gradient exceeds the spring constant of the cantilever. An analogous phenomenon occurs when pulling on macromolecules, where the force difference and spacing between consecutive bonds to be broken will determine whether the second bond can be resolved independently from the first with a cantilever of a given spring constant.

Because of force instabilities, force transducers with high stiffness and excellent force resolution are required. In addition to force curve measurements, if a probe is stiff enough to avoid snap-down, non-contact imaging using attractive forces can be performed without touching the surface[1]. This type of imaging minimizes friction forces that can affect the image and avoids high repulsive forces that can damage the tip or sample. Unlike contact mode imaging, where a great many atoms can be in contact, resulting in averaging of the signal, the forces in non-contact mode imaging are dominated by the nearest several atoms. For this reason, non-contact AFM is usually used for true atomic resolution images[2]. Non-contact imaging is also used for images of magnetic fringing fields[3,4] and imaging of localized charge[5,6].

In non-contact AFM, the cantilever is oriented parallel to the surface, and is oscillated normal to the sample at its resonance. The presence of a force gradient from the tip-sample interaction results in an effective spring constant given by $k_{eff}=k+dF/dz$, where z

is the height of the tip above the sample[1]. By tracking changes in the resonance, the force gradient can be measured. A relatively stiff cantilever ($k>10$ N/m) is required to avoid snap-down instabilities.

A variation of this technique used for distance control in near field scanning optical microscopy (NSOM) is a mode called shear force microscopy[7]. In this mode, a cantilever perpendicular to the surface is driven at resonance. Attractive forces increase the resonant frequency, much like a pendulum in high gravity has a higher natural frequency. Because the cantilever is perpendicular, there is little concern of snap-down instabilities. This permits the use of softer cantilevers for improved force resolution. Using this approach, atto-Newton-level forces have been measured in vacuum at low temperature[8].

Both non-contact AFM and shear force microscopy are valuable techniques, resistant to force gradient instabilities, but they share a substantial limitation—the position of the probe tip is no longer precisely specified. Oscillation amplitudes on the order of 10 nm and greater are frequently used. For non-contact AFM, the measured force gradient is therefore actually the average over this tip motion, although the lateral spatial resolution is still well defined. For shear force microscopy, the lateral resolution is directly blurred by the tip motion. Neither technique is applicable for pulling on macromolecules, since nanometer-scale tip motion is unacceptable where the bonds to be measured may be only angstroms apart. Non-contact AFM is further unsuitable for this purpose, since it measures force gradients and not forces.

A third technique used to resist force instabilities is to stiffen a conventional cantilever by use of a force-feedback re-balancing technique. In one partially successful attempt, the cantilever end was coated with a magnetic material, and an external magnetic field used to exert forces on the tip[9]. To balance the cantilever during a force instability

requires a closed-loop bandwidth considerably greater than the cantilever resonance, however, which their system did not have the required actuator authority to achieve.

Another advantage that non-contact and shear-force microscopy share over traditional AFM use is the benefit of resonant detection. The popularity of resonant sensing as a technique for MEMS sensors is evidence of its advantages, and resonant detection has been employed for a variety of high resolution pressure sensors and accelerometers[10,11].

There are several advantages to resonant-based sensing techniques for micromachined sensors. Signals varying at frequencies well below the device resonance cause shifts in the resonant frequency. As a result, the resolution is only influenced by noise near the resonance, and not the *1/f* noise that is present at low frequencies for almost all detection techniques. As a further benefit, the frequency sensitivity scales favorably with reduced dimensions, as will be shown in section 7.2, and can be quite high for appropriately designed micromachined sensors. Finally, the forces to be measured can be applied axially to the resonator, resulting in a highly stiff transducer.

7.1. An axial resonant AFM probe

A probe concept that exploits the advantages of resonant detection with a stationary tip is illustrated in Figure 7-1. A cantilever is oriented perpendicular to the surface, as in shear force microscopy, but a tether near the end of the beam constrains the tip from oscillating, while allowing axial forces to be transmitted to the resonator. The tether is the critical addition, and is illustrated conceptually as a block on rollers. In this way, the tether directly couples vertical forces to the sensing element, but prevents any motion of the resonating beam from being transmitted to the tip, which remains stationary. The oscillator then responds to forces (not force gradients) by a shift in resonance. A close analogy can be drawn to the tuning of a violin or guitar, where the bridge prevents the

string from motion near the tuner, but permits the tension applied by the tuner to be transmitted to the rest of the vibrating string. An earlier non-microfabricated AFM sensor using this concept was in fact called a nanoguitar[12].

Figure 7-1. Schematic illustration of resonant beam AFM probe with stationary tip.

This sensor design provides three major benefits: 1) a vertical cantilever is extremely stiff, and therefore much less susceptible to force instabilities, 2) the motion of the resonating beam is measured near resonance, well away from the *1/f* noise of the secondary detector 3) the tip can be nearly stationary, for precise location and manipulation.

7.2. Sensor design

There are several key components to the sensor design. First, the oscillating beam should be designed for maximum force resolution. Second, the tether needs to ensure that the tip remains as stationary as possible, while transmitting the applied force to the resonant beam. Third, a method must exist for excitation of the resonator, and finally, the tip must be sharp and able to access the surface for probing. All of these objectives must be satisfied in a manner compatible with relatively planar microfabrication techniques.

It will be shown in the following section that a thin beam is critical to high sensitivity frequency shifts. Although a design similar to the one illustrated in Figure 7-1 could likely be fabricated using DRIE techniques, a thinner oscillator can be fabricated if the design is modified, as illustrated in Figure 7-2. In this case, the oscillator vibrates out of the plane and can therefore be deposited as a thin layer, rather than defining the thickness lithographically. It is also a more convenient orientation for an integrated piezoresistive sensor to measure the beam motion.

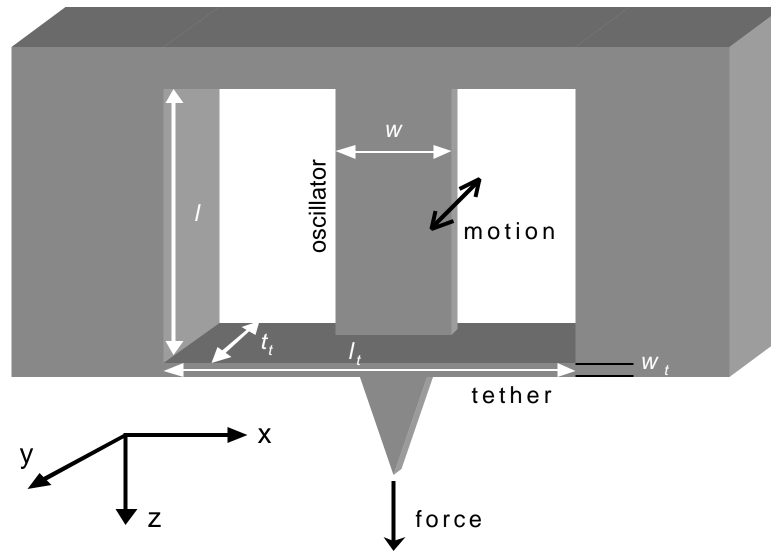

Figure 7-2. Illustration of an oscillator and tether for a planar fabrication process. The beam oscillates in the *y*-direction, measured forces are applied in the *z*-direction. The tether prevents the oscillator motion from being transmitted to the tip, so the tip does not move in response to the oscillations.

Beam design

The basic design trends for the resonator design can be derived from a simple sensitivity analysis. From fundamental beam equations[13], the resonant frequency of a beam with fixed ends, under an applied load F is given approximately as

$$\boldsymbol{w}_0 \cong \sqrt{\frac{12Et^2}{l^4\boldsymbol{r}} + \frac{12F}{l^2wt\boldsymbol{r}}} \tag{7.1}$$

where $\boldsymbol{w}_0$ is in radians per second, E is the modulus of elasticity and $\boldsymbol{r}$ is the density of the beam material. The width, length, and thickness of the beam are w, l and t respectively. Differentiating this expression with respect to the applied force F, and considering the response where F is small compared to the buckling force, gives the sensitivity of the resonant frequency to an applied load as

$$\frac{d\mathbf{w}_0}{dF} = \frac{1}{wt^2}\sqrt{\frac{3}{\mathbf{r}E}}\,. \qquad (7.2)$$

By itself, this expression could be misleading, since a simple external frequency multiplier can make this number arbitrarily large. Similar to the ΔR/R sensitivity quoted for piezoresistors, this expression can be normalized by the unloaded resonance to give

$$\frac{d\mathbf{w}_0}{\mathbf{w}} = \frac{l^2}{2wt^3E}dF\,. \qquad (7.3)$$

This equation gives the essential design objectives for high sensitivity: thin, long and narrow beams, in that order of importance. The beam width chosen was 4 µm, about twice the minimum line width of the stepper aligner used for the masks, and the beam thickness was chosen to be 0.2 µm. We were attempting 0.1 µm piezoresistors for the first time concurrent with the fabrication of these probes[14], and some margin was desired in case the thinner process failed. A length of 200 µm was chosen to set the fundamental resonance in the 10s of kilohertz, away from most probable *1/f* noise sources. Typical dimensions for surface micromachined resonant sensors are usually a 2 µm thickness, widths some 10s of microns and lengths in the hundreds of microns. The dimensions chosen for this sensor therefore improve the sensitivity roughly four orders of magnitude, primarily due to our capability of making thin piezoresistors.

The tether

In the coordinate system indicated in Figure 7-2, the x-z plane is the surface of the wafer. A surface to be probed would lie in the x-y plane. The oscillating beam motion is in the y-direction, so in order to keep the tip stationary, a tether is needed to resist motion in y. The surface forces to be measured occur in the z-direction, so the tether should be flexible along the z-axis to effectively transmit forces to the resonator. This can be

achieved with a cross-beam tether that is thick in the *y*-direction, and narrow in the *z*-direction.

The ideal tether does not exert any force in *z*, so a prudent observer might wonder if the *z*-direction stiffness of the tether will affect the forces measured by the oscillator. To applied forces, the bending of the tether and the axial compression of the resonator look like springs in parallel. If thickness is measured in the *y* direction, the tether width measured in the *z* direction, and the length is the distance between the two supports, the spring constant of the tether is

$$k_{tether} = \frac{16 E w_t t_t^3}{l_t^3}. \tag{7.4}$$

The spring constant of the oscillating beam axially is

$$k_{axial} = \frac{Ewt}{l} \tag{7.5}$$

Since the stiffness of a beam varies as the cube of its thickness, and because the oscillator is only 0.2 µm thick, a 2 µm-thick by 400 µm-long tether should attenuate the tip motion by several orders of magnitude compared to an un-tethered beam. The width of the oscillator was set at a minimum of 2 µm based on the lithography capabilities of the aligner. The bending spring constant of the tether in the *y*-direction is 0.68 N/m, compared to the axial spring constant of 680 N/m for the oscillator. This means that 99.9% of the applied force is absorbed in the oscillator, and the tether effect is insignificant. The 680 N/m axial spring constant is the number that determines susceptibility to force gradient instabilities, so the cantilever is immune to such problems.

Probe tip

An essential part of any AFM probe is a sharp tip, usually with a radius of less than 10 nm. Conventional AFM tip-making techniques are developed for placing the tip at right angles to the cantilever and are not applicable for a vertical probe. Fortunately, a technique has been developed at IBM Almaden to fabricate in-plane tips using a brief

TMAH etch to define <111> planes which intersect to form a tip of radius less than 5 nm[15]. For proof of concept of these probes, a sharp tip was not required, and a tip was simply defined as a sharp vertex on the mask.

The other issue for the probe tip is that it be able to access the sample with clearance for the chip corners. This can easily be accomplished by extending the tip on a support member. In order that the tip beam not flex and cause tip motion, this beam should be rigid.

Driving the oscillator

The signal to noise ratio of resonant sensors improves with larger oscillation amplitudes. It is preferable, therefore, to drive the beam with larger oscillation amplitudes than result from intrinsic thermomechanical motion alone. AFM resonant probes usually use a piezoelectric actuator to shake the entire chip, but such a method is unacceptable if the tip is to remain stationary. The other likely options for the drive are capacitive or thermal. Both capacitive and thermal drive result in forces at twice the voltage drive signal, because the forces are proportional to the square of the voltage. The resulting motions is therefore at twice the driving frequency, which is important for distinguishing motion signals from electrical noise due to the drive signal. Capacitive drive was chosen for this application, out of concern that a thermal drive might not provide sufficient amplitude for low-Q oscillation in air, particularly at high frequencies.

The electrostatic force between two parallel plates is approximately given by

$$F_{plate} = \frac{\boldsymbol{e}\boldsymbol{e}_0 A V_B^{\,2}}{2d^2}, \qquad (7.6)$$

where V_B is the voltage difference between the two surfaces, A is the surface area, $\boldsymbol{e}$ is the relative dielectric constant, $\boldsymbol{e}_0$ is the dielectric permittivity of a vacuum (8.85×10^{-12} C/Nm^2) and d is the distance between the two plates.

A narrow oscillating beam is favored from sensitivity concerns, yet provides little area with which to generate electrostatic drive forces. Accordingly, a paddle was added at the center to increase the area for the capacitive drive. This paddle also provides surface area to reflect a laser, which makes optical detection of the oscillator possible, either for characterization or operation. For the purposes of this proof-of concept, the drive electrode was a length of fine copper wire epoxied onto the chip and bent close to the oscillator with a micromanipulator, as illustrated in Figure 7-3. The end of the wire was first melted with a lighter to produce a ball at the end of approximately 500 µm radius. With a sphere on the end of the driving electrode, the electrode could be positioned close to the paddle without concern for the orientation of the wire.

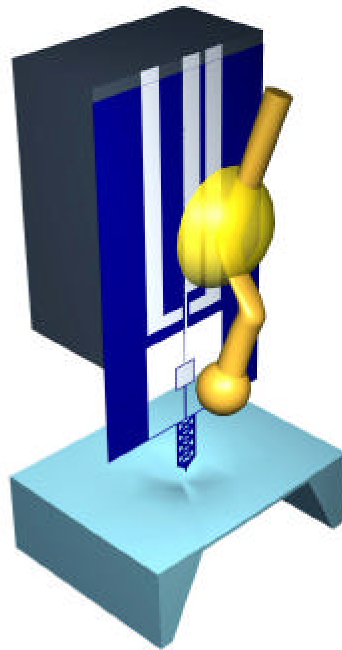

Figure 7-3. Calibrating an axial resonant probe. The sensor is calibrated by pressing on a micromachined membrane of known spring constant. A thin copper wire is epoxied to the chip to capacitively excite the resonator.

Secondary detection

The primary objective, detecting forces applied to the tip, is achieved by measuring the motion and resonance of the oscillator by way of a secondary detector. Optical detection with an interferometer or optical lever would provide the best possible resolution, limited only by thermomechanical noise of the paddle. The laser detection that comes standard on all AFMs, however, would not be able to reflect light off the paddle because of the probe orientation. For the probe to be compatible with existing AFMs an integrated piezoresistive sensor was chosen.

The *1/f* noise of the piezoresistor is not an issue for this sensor, so to maximize piezoresistor sensitivity the current path is confined to the base of the cantilever. To this end, the current path at the base of the oscillator is defined by a split of the beam into two 2-µm-wide legs for the last 10 µm, as shown in Figure 7-4.

7.3. Fabrication

The fabrication procedure is essentially the same as that described for the ultra-thin piezoresistors in Chapter 2, with the added complication that different thicknesses are required for the oscillator and for the tether. This was achieved by starting with a 2-µm-thick SOI wafer and first defining a mask layer for the tether and supporting structure. With the tether protected, the rest of the surface is thinned in an anisotropic plasma etch to 0.2 µm. A thin epitaxial layer was then used to create a doped layer, followed by another lithography and plasma etch to define the oscillator pattern.

The other fabrication steps are then exactly as for a traditional piezoresistive cantilever. The backside etch can be done with a wet etch, if the tether supports are built into the top epitaxial layers. A better solution is use of the Bosch process DRIE to define a backside etch mask that leaves bulk silicon at the base of the oscillator and at the ends of the tether.

A composite SEM of the completed device is shown in Figure 7-4.

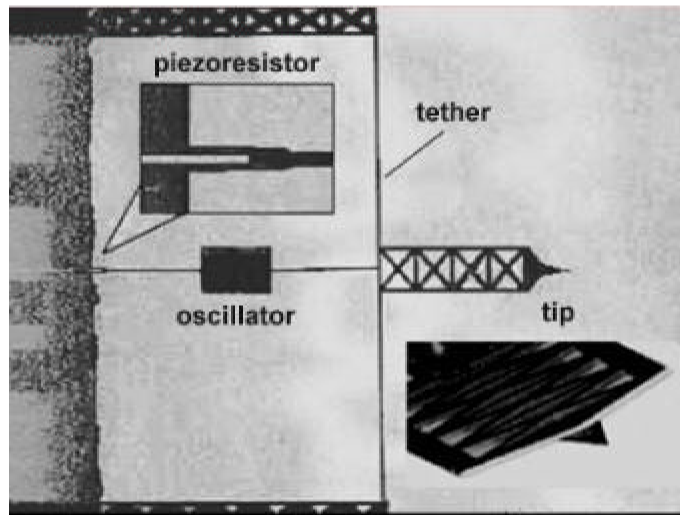

Figure 7-4. SEM image of force probe. Tether is 2µm thick by 2µm wide. Oscillator is 0.2µm thick, 4µm wide and 200µm long.

7.4. Applying calibrated forces

In order to test the force resolution of the devices it was necessary to apply a known force load to the tip. Calibrated loading was achieved by pressing the cantilever against a micromachined membrane 2 µm thick, and 2 mm on a side, as illustrated in Figure 7-3. If the membrane spring constant is known, then displacing the membrane a known amount results in the application of a calibrated load. The membrane spring constant was modeled using Ansys to be 0.92 N/m.

Pressing one cantilever against a known reference cantilever has been employed as a calibration technique, although not particularly reliable for normal AFM cantilevers. Two issues that plague this type of cantilever calibration are not present in this measurement. The first, and perhaps most damaging, is that the two cantilevers are rarely parallel. Most AFMs intentionally tilt the probe cantilever 5 to 15 degrees so the cantilever touches the surface before the support chip. With a tip extending several

microns off the end of the cantilever, pressing down introduces moments that cause the cantilever to bow upwards rather than bend downwards as expected. Because this model-T probe is oriented vertically and has an in-plane tip, this issue does not arise.

The second issue is that if the reference cantilever is not contacted at the tip, the spring constant may be significantly different than expected. The same problem occurs when pressing on a membrane if the probe is off center. For a 2 mm-wide square membrane, however, the spring constant 200 µm from the center is only 7% greater than at the center, and 33% greater 400 µm from the center. Placing the probe with this level of accuracy does not pose a problem. For 7% accuracy pressing on a typical 200 µm-long AFM cantilever, the load must be within 5 µm of the cantilever end.

To test the lower force resolution limits, forces on the order of 1 nN or less must be applied to the sensor. Given the ~1 N/m spring constant of the membrane, this will require sub-nanometer displacements of the probe, which can best be achieved with a piezoelectric actuator. An existing AFM could be used as the actuator for this experiment, but in order to explore the importance of resonance quality on the resolution a system was needed which could function either in air or vacuum. To this end a stage was manufactured with a manual screw to approach within a few microns of contact, and a piezoelectric stack to provide the fine motion. A photo of this stage is shown in Figure 7-5.

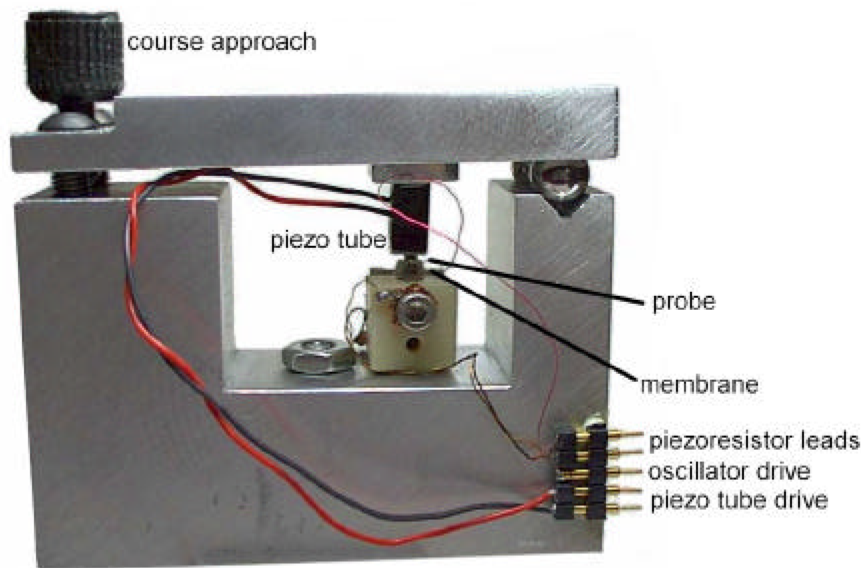

Figure 7-5. Photo of experimental set-up. This is essentially a crude AFM, intended for measuring the force resolution inside a vacuum chamber.

The piezoelectric stack was calibrated using a laser vibrometer and found to have a displacement response of 59 nm/V. A Burleigh high-voltage op-amp was used to apply a large DC offset for the approach, with a smaller sine wave added onto the approach signal to apply a small force modulation. The voltage output from the Burleigh had 20-25 mVrms of noise on the signal, which corresponds to almost 2 nN of force noise. In order that this noise not limit the detectable force resolution, the low frequency approach voltage was low-pass filtered at 1 Hz, reducing the voltage noise to 0.7 mVrms, or 60 pN of force noise. The applied force sine-wave signal was then AC coupled in after the high-voltage op-amp to modulate the piezoelectric stack.

7.5. Results

Piezoresistor calibration

To characterize the secondary detector, a Polytek laser vibrometer was targeted on the paddle, and the vibrometer and piezoresistor signals compared. This measurement was done with no loading on the probe. Two principal modes are visible on the vibrometer signal, as shown by the solid line in Figure 7-6. The fundamental resonance occurs near 25 kHz, with a second resonant mode at 45 kHz. The response from the piezoresistor is too noisy to show these thermomechanical noise peaks, but applying a capacitive drive signal to the paddle creates a motion that is detectable by both the vibrometer and piezoresistor. From such a measurement, the piezoresistor response was measured to be 5300 V/m, or $\Delta R/R$ of 4200 m^{-1}. From this data the amplitude of the oscillation voltages during operation can be translated into displacement.

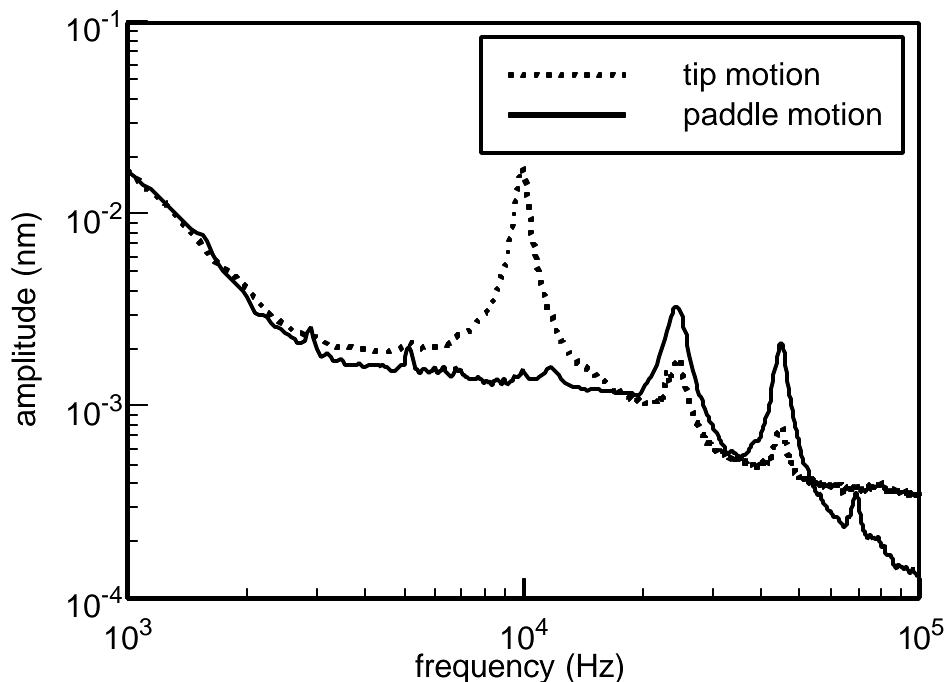

Figure 7-6. Vibrometer signal showing thermomechanical motion of the paddle and the probe tip. The solid line illustrates the paddle motion, which has resonant modes at ~25 kHz and ~45 kHz. The tip has a large unwanted mode at ~10 kHz due to torsion of the tether.

Unwanted tip modes

The dotted line trace on Figure 7-6 was measured with the vibrometer reflecting off the probe tip. There is a large peak near 10 kHz, which clearly indicates unwanted motion caused by torsion of the tether. This design flaw limits the use of these first-generation probes, since without a stationary tip one of the main advantages is lost. The addition of a second tether bar would allow the two tethers to exert a much higher moment than a single tether, still without significantly absorbing the forces intended for the resonator. This concept is illustrated in There is no limit on the spacing between the two tethers, so the moment they apply can be arbitrarily increased until this mode is no longer a problem.

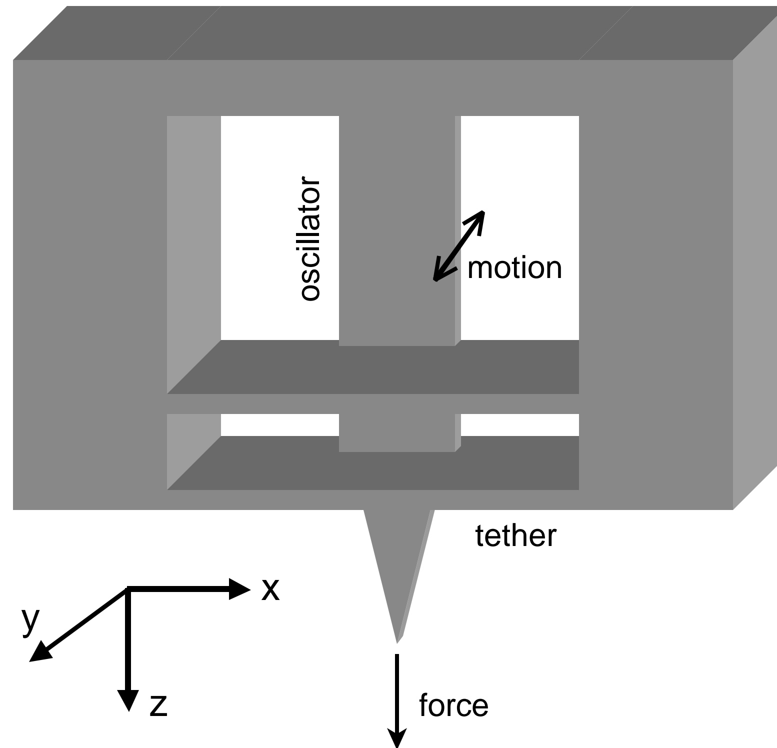

Figure 7-7. Axial resonant probe with a double tether. The two tethers can exert a restraining moment, preventing the tip from oscillating by the torsion of a single tether.

Demodulating the resonant signal

Applied loads modulate both the phase and amplitude of the resonator. For this measurement, the amplitude-modulated signal was measured using the oscillator response as a slope detector. This approach, often used in the AFM community for its simplicity, is to drive the resonator with a sine-wave input slightly above its resonant frequency[1]. The amplitude of the motion will be enhanced by the transfer function of the oscillator. For a fixed drive frequency, the resulting amplitude will vary as the resonator response curve shifts laterally. This is illustrated in Figure 7-8.

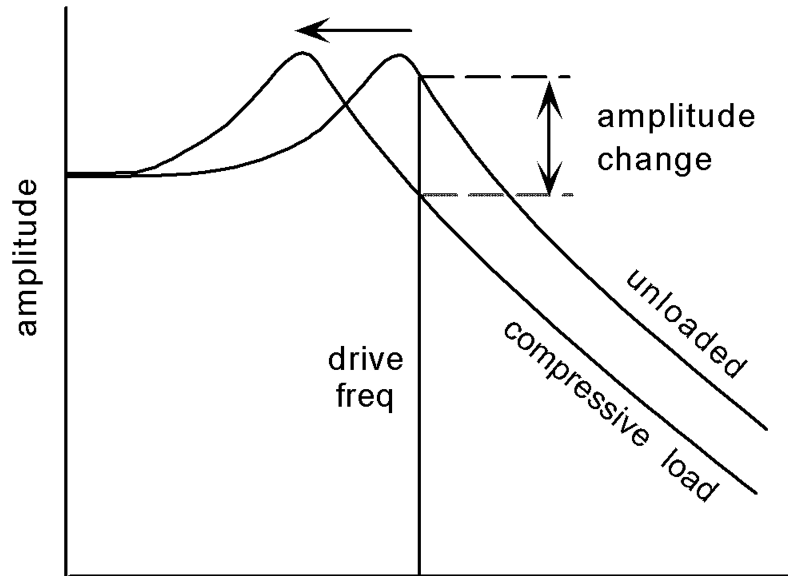

Figure 7-8. Amplitude detection of resonance shifts. The oscillator is driven at a fixed frequency, near the resonant peak. As the resonance shifts, the Q enhancement of the oscillator motion is either increased or decreased, resulting in an amplitude modulated signal.

There are two major disadvantages to this technique. The first is that the sensitivity varies with the applied load. The maximum slope of the transfer function occurs at a single point just off resonance and as the resonance shifts further away from the drive, the slope of the response curve changes. The second disadvantage is more fundamental. It was shown by Albrecht *et al.* that amplitude changes cannot occur instantaneously because transients must first settle[16]. For high Q oscillators these transients can limit the bandwidth capabilities of the measurement to less than 1 Hz.

For the characterization of this sensor, the slope detector was adequate. Simple frequency counting is another option, but the signal to noise of a frequency counter degrades rapidly with increased bandwidth and is therefore not favored for AFM use. A more complicated and versatile phase demodulator developed by Dürig *et al.* would be more appropriate as a long-term solution, however[17].

For a second order system with a given Q and $\boldsymbol{w_0}$ the maximum slope of the frequency response curve has been shown to occur at $\boldsymbol{w_0}=\boldsymbol{w}_0(1\pm1/Q\sqrt{8}\ )$[1]. At this point the slope of the response is

$$\frac{dA_0}{d\boldsymbol{w}_0}=\frac{4A_0Q}{3\sqrt{3}\boldsymbol{w}_0}. \tag{7.7}$$

This equation gives the change in the amplitude of the cantilever motion as the drive frequency is swept near resonance. It is also the change in amplitude of a fixed-frequency drive as the resonant frequency shifts by amount $d\boldsymbol{w}_0$ due to an applied load. Combining this equation with the frequency sensitivity from equation (7.2) gives the change in amplitude of the drive signal for a given force dF as

$$\frac{dA}{dF}=\frac{2\sqrt{3}A_0Ql^2}{9wt^3E}. \tag{7.8}$$

This equation has the same geometry dependence as equation (7.3), validating the original sensitivity derivation as a design tool.

Force resolution

Using the set-up described in section 7.4, calibrated loads were applied to the sensor. As the probe approached the membrane, the resonant frequency increases. Eventually, the membrane jumps up into contact with the probe, and the oscillation amplitude is slightly diminished due to the elimination of the tip motion. Once in contact, a 12 nm z-motion at 50 Hz was applied to the membrane, resulting in an applied 12 nN load. The resulting amplitude modulated signal was measured with a lock-in amplifier with a measurement bandwidth of 1 kHz and recorded on a digital oscilloscope. This data is shown as the lower trace in Figure 7-9. The Q of the cantilever at this time was only 20, due to air damping of the thin oscillator, and the oscillation amplitude was 36 nm. The resolution in a 1 kHz bandwidth is 9 nN, limited by the 300 pN/√Hz white displacement

noise of the piezoresistor. For detection using the laser vibrometer, thermomechanical noise is the limiting source.

The same measurement was then performed in a 1 mTorr vacuum. At this pressure the Q improves to 450. This Q value was much lower than expected for such a single-crystal-silicon cantilever, and is perhaps due to surface contamination. There was visible contamination on other devices from this wafer, remaining from an inadequate clean prior to the critical point drying release. Single crystal cantilevers thinner than these have been demonstrated with a resonance quality of greater than 15000, and up to 80000 after annealing to remove surface contamination[18]. Even for a Q of 450, with oscillation amplitude of 53 nm, the force resolution improves dramatically. A 1 nN applied load has much better signal to noise in vacuum than the 12 nN load in air as shown in Figure 7-9. The force resolution under vacuum is about 200 pN in 1 kHz or 7 pN/√Hz. This force resolution is approaching the limit of what this membrane calibration source can apply, due to the 60 pN of amplifier noise on the piezoelectric drive signal.

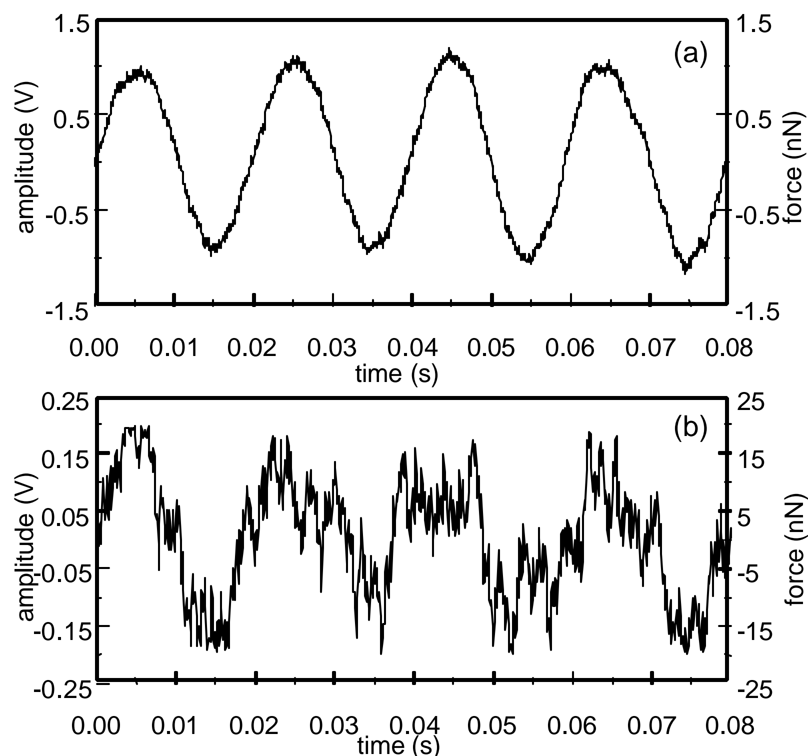

Figure 7-9. Force resolution of axial probe in vacuum and in air. (a) Time trace of a 1 nN force applied in vacuum with an oscillation amplitude of 53 nm, compared to (b) a 12 nN load applied in air with oscillation amplitude of 36 nm. Both measurements are in a 1 kHz bandwidth. The trace in vacuum has a Q of ~450, compared to a Q of ~20 in air, and the resulting signal to noise ratio is improved by a factor of ~40 in vacuum compared to air.

According to equation (7.8), the sensitivity should improve linearly with the Q and with the oscillation amplitude. Since the white noise from the piezoresistor is unchanged in air or vacuum, the resolution should improve as 1/sensitivity. From the measured increase in amplitude and Q, the resolution should have improved by a factor of 33. The measured resolution improved by a factor of 40, a discrepancy that is within the error of the measurement. For clean cantilevers with better Q, therefore, the force resolution should improve at least another order of magnitude.

The Q for such cantilevers is dramatically degraded in liquid, down to single digit values[19]. There are many interesting possible force measurements on biological molecules currently on the fringe of the capabilities of the AFM. If an encapsulation

method could be devised to permit the Q of vacuum while in water, such a probe could prove quite valuable.

An effective encapsulation method would need to seal the resonator in a vacuum cavity, yet allow forces to be transmitted to the oscillator within. A membrane perpendicular to the oscillating beam (in the x-y plane of Figure 7-2) is one possibility.

Because of the high stiffness of the vertical probe, these forces correspond to minute displacements. For a spring constant of 680 N/m, a 10 nN force corresponds to less than a 0.1 Å displacement, so even in air the displacement resolution is excellent. In vacuum, the 200 pN force resolution is equivalent to a 0.3 pm displacement.

7.6. Summary and future work

A novel probe has been presented which uses a resonating beam, tethered at both ends to create a high-stiffness resonant force probe with good resolution, a stationary tip, immunity to force gradient instabilities and a large dynamic range. Issues remain regarding unwanted tip motion, though they can be remedied in future designs with the addition of a second tether. For the best resolution, operation in a vacuum is required, which limits the potential use to a much smaller community with vacuum AFMs. If a method to encapsulate the resonator could be devised, however, the probe would extend the force measurement capabilities of the AFM for measurements in air or water.

References

1. Y. Martin, C. C. Williams, and H. K. Wickramasinghe, "Atomic force microscope-force mapping and profiling on a sub 100-Å scale," *J. Appl. Phys.*, vol. 61, no. 10, pp. 4723-4729, 1987.

2. Y. Sokolov, G. S. Henderson, and F. J. Wicks, "Theoretical and experimental evidence for "true" atomic resolution under non-vacuum conditions," *J. Appl. Phys.*, vol. 86, no. 10, pp. 5537-5540, 1999.

3. Y. Martin and H. K. Wickramasinghe, "Magnetic imaging by 'force microscopy' with 1000 Å resolution," *Appl. Phys. Lett.*, vol. 50, no. 20, pp. 1455-1457, 1987.

4. D. Rugar, H. J. Mamin, P. Guethner, S. E. Lambert, J. E. Stern, I. McFadyen, and T. Yogi, "Magnetic force microscopy: general principles and application to longitudinal recording media," *J. Appl. Phys.*, vol. 68, no. 3, pp. 1169-1183, 1990.

5. J. E. Stern, B. D. Terris, H. J. Mamin, and D. Rugar, "Deposition and imaging of localized charge on insulator surfaces using a force microscope," *Appl. Phys. Lett.*, vol. 53, no. 26, pp. 2717-2719, 1988.

6. T. D. Stowe, T. W. Kenny, D. J. Thomson, and D. Rugar, "Silicon dopant imaging by dissipation force microscopy," *Appl. Phys. Lett.*, vol. 75, no. 18, pp. 2785-2787, 1999.

7. E. Betzig, P. L. Finn, and J. S. Weiner, "Combined shear force and near-field scanning optical microscopy," *Appl. Phys. Lett.*, vol. 60, no. 20, pp. 2484-2486, 1992.

8. T. D. Stowe, K. Yasumura, T. W. Kenny, D. Botkin, K. Wago, and D. Rugar, "Attonewton force detection using ultrathin silicon cantilevers," *Appl. Phys. Lett.*, vol. 71, no. 21, pp. 288-290, 1997.

9. S. P. Jarvis, U. Duerig, M. A. Lantz, H. Yamada, and H. Tokumoto, "Feedback stabilized force-sensors: a gateway to the direct measurement of interaction potentials," *Applied Physics A (Materials)*, vol. 66, pp. S211-S213, 1998.

10. G. Stemme, "Resonant silicon sensors," *Journal of Micromechanics and Microengineering*, vol. 1, pp. 113-125, 1991.

11. D. W. Burns, R. D. Horning, W. R. Herb, J. D. Zook, and H. Guckel, "Resonant microbeam accelerometers," *Proceedings of the 1995 8th International Conference on Solid-State Sensors and Actuators*, pp. 659-662, 1995.

12. A. Stalder and U. Durig, "Nanoguitar: oscillating string as force sensor," *Rev. Sci. Inst.*, vol. 66, no. 6, pp. 3576-3579, 1995.

13. Timoshenko, S., Young, D. H., and Weaver, J., *Vibration Problems in Engineering,* 5th ed., Wiley, New York, 1974.

14. Harley, J. A., Stowe, T. D., and Kenny, T. W., "Piezoresistive Cantilevers with Femtonewton Force Resolution," *The 10th international conference on solid-state sensors and actuators*, vol. 2, pp. 1628-1631, Sendai, Japan, 1999.

15. Ried, R. P., Mamin, H. J., Terris, B. D., Fan, L. S., and Rugar, D., "5 MHz, 2 N/m piezoresistive cantilevers with INCISIVE tips," pp. 447-450, 1997.

16. T. R. Albrecht, P. Grutter, D. Horne, and D. Rugar, "Frequency modulation detection using high-Q cantilevers for enhanced force microscope sensitivity," *J. Appl. Phys.*, vol. 69, no. 2, pp. 668-673, 1991.

17. U. Dürig and H. R. Steinauer, "Dynamic force microscopy by means of the phase-controlled oscillator method," *J. Appl. Phys.*, vol. 82, no. 8, pp. 3641-3651, 1997.

18. K. Y. Yasumura, T. D. Stowe, E. M. Chow, T. Pfafman, T. W. Kenny, and D. Rugar, "A study of microcantilever quality factor," *Technical Digest. Solid-State Sensor and Actuator Workshop*, pp. 65-70, 1998.

19. D. A. Walters, J. P. Cleveland, N. H. Thomson, P. K. Hansma, M. A. Wendman, G. Gurley, and V. Elings, "Short cantilevers for atomic force microscopy," *Rev. Sci. Inst.*, vol. 67, no. 10, pp. 3583-3590, 1996.

Epilogue

For those that made it this far through the dissertation, a natural question is this: if I were starting the DNA unzipping experiment today, how would I approach it? My estimations of the requirements for the project have not changed, so the question is really whether or not a probe is now available with the following characteristics:

- 1 pN force resolution,
- 10 Hz to 100 kHz bandwidth
- a spring constant greater than 0.01 N/m.

With these specifications in mind, I can evaluate the ultra-thin piezoresistors and the axial resonant probe.

Thin Piezoresistive Cantilevers

Once the excellent sensitivity of the 1000 Å piezoresistive cantilevers had been demonstrated, I should have been able to meet the above specifications. The unexpected increase in *1/f* noise for the small cantilevers brings this into question, however.

Devices 500 Å thick are probably possible without further innovation. From Figure 6-8 then, the Hooge limited resolution would be (0.4 nm/√dec)·(2√dec)·(0.01 N/m) = 8 pN. From the same graph, the Johnson limited resolution would be (1pm/√Hz)·√(99990 Hz)·0.01 N/m) = 3 pN. The total force resolution would therefore be ~8.5 pN. From Figure 3-3, the resonant frequency of the cantilever would be about 400 kHz, safely above the specification.

While these numbers are close, they also presume nearly optimal cantilevers, and still turn up almost an order of magnitude short of the desired force resolution. The cantilever could be increased in length to give a spring constant of 0.001 N/m and still meet the

bandwidth specifications. Force instabilities may now become a concern, however, although the device is still a two order of magnitude improvement in stiffness over optical tweezers. In this case, the force resolution is ~3 pN.

I am also concerned as to how these cantilevers will operate in liquid. My original piezoresistor work for the NRL biosensor project began because they could not use commercial piezoresistive cantilevers in solution. Under bias in an aqueous solution, the aluminum leads undergo an electrochemical reaction and corrode in a matter of seconds. This corrosion problem was overcome with by coating the leads with a passivating polyimide layer. A similar coating could be used for these cantilevers, but the biosensor cantilevers additionally had a 1000 Å-thick passivating oxide layer on the beam itself. A 500 Å-thick cantilever obviously cannot such a layer, and there may be problems with the bare silicon in an aqueous solution.

Axial Probe

The axial resonant probe is another possibility for the DNA-pulling measurement. Because it uses resonant detection, *1/f* noise is not a problem. The current probes achieved 7 pN/√Hz force resolution in vacuum, which translates to 2 nN over a 100 kHz bandwidth. If that device were reduced in thickness to 500 Å (a factor of 4), the sensitivity should improve 64-fold. The length would have to also be reduced to boost the resonance up to the mega-Hertz region for the bandwidth, but the sensitivity could still improve at least an order of magnitude. The Q can reasonably be expected to increase 30-fold. A 16x improvement in sensitivity and a 30x improvement in Q, however, still only get the probe to 5 pN in a 100 kHz bandwidth.

There may be other knobs to play with here, and another order of magnitude improvement could be achieved by using optical detection instead of the built-in piezoresistor, but I am glossing over the critical limitation - these Q values are

obtainable only in vacuum, not in liquid. This means the encapsulation problem must also be solved. The first difficulty here is figuring out a fabrication process that makes a resonator perpendicular to a sealing membrane. Even if this is solved, there is the matter of the force due to the pressure difference across the membrane. Atmospheric pressure of 10^5 Pa exerts 1 mN of force on a 100 μm by 100 μm square membrane. Designing a mechanical system to account for this unwanted additional force, and the force noise that pressure fluctuations would cause, is a task I wouldn't even wish on a thesis advisor.

The value of this type of resonant probe probably lies in its ability to measure minute displacements. There are few ways to measure pico-meter displacements, which this system can accomplish in air, even without encapsulation. Such a device with a built in NSOM tip could alternatively provide the height control for a near-field scanning microscope with a non-oscillating tip. The problem of the unwanted tip oscillations should be straightforward to solve.

Despite these concerns, it would be a mistake to underestimate the innovation of future scientists, and I expect to see exciting force measurements in the not-too-distant future. If pressed, I would wager that optical detection techniques will play a role. Piezoresistors in other materials may also come to light, although Hooge-like noise was recently also observed in carbon nano-tubes (P.G. Collins, M.S. Fuhrer and A. Zettl, "1/*f* noise in carbon nanotubes", Applied Physics Letters, Vol 76., No. 7, pp. 894-896, 2000).

APPENDIX A: Table of Variables

Variable	Definition	Units
$\mathbf{a}$	Hooge constant	-
$\mathbf{b}$	sensitivity efficiency	-
$\mathbf{d}$	distance between bonds	m
$\mathbf{e}$	relative dielectric permittivity	-
$\mathbf{e}_0$	dielectric permittivity of a vacuum	C/Nm^2
$\mathbf{m}$	mobility	$cm^2V^{-1}s^{-1}$
$\mathbf{p}_l$	piezoresistive coefficient	m^2/N
$\mathbf{r}$	resistivity	$\mathbf{W}\times cm$
$\mathbf{s}$	stress	N/m^2
$\mathbf{w}_0$	resonant frequency	rad/sec
a	leg length ratio	-
A	area	m^2
A_0	oscillation amplitude	m
B	measurement bandwidth	Hz
c	distance to neutral axis	m
D	diffusion coefficient	cm^2s^{-1}
d	distance between capacitive plates	m
D_{io}	diffusion coefficient	cm^2s^{-1}
E	modulus of elasticity	N/m^2
E_{ia}	activation energy	eV
F	force	N
f_0	resonant frequency	Hz
F_{th}	Force noise power	N^2/Hz

H	2nd order oscillator transfer function	-
I	Area moment of inertia	m^4
I	total current	A
J	current density	A/m^2
k	spring constant	N/m
k_B	Boltzmann's constant	J/K
l	length	m
l_t	tether length	m
l_{leg}	leg length	m
m	effective mass	kg
M	moment	$N \cdot m$
N	number of carriers	-
p	doping density	cm^{-3}
P	piezoresistive coefficient factor	$0<P<1$
q	electron charge	C
Q_T	total charge density	C/cm^2
R	resistance	Ω
S_H	Hooge noise power density	V^2/Hz
S_J	Johnson noise power density	V^2/Hz
$S_{F,th}$	thermomechanical force noise power density	N^2/Hz
S_{th}	thermomechanical displacement noise power density	m^2/Hz
t	thickness	m
t_t	tether thickness	m
T	temperature	K
t_d	doped thickness	m
V_B	bias voltage	V

V_{out}	output voltage	V
V_H^2	Hooge voltage noise power	V^2
V_J^2	Johnson voltage noise power	V^2
w	width	m
w_t	tether thickness	m
x	cantilever displacement	m
x_{min}	displacement resolution	m
z	distance to surface	m